e-ISSN: 2618-575X

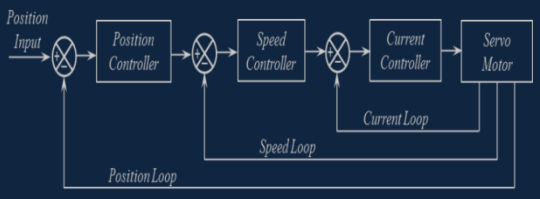

International Advanced Researches and Engineering Journal

Aerospace Engineering,
Aquaculture and Fisheries Engineering,
Architecture,
Bioengineering,
Chemical Engineering,
Civil Engineering,
Computer Engineering,
Electrical and Electronics,
Energy,
Environmental Engineering,
Food Engineering,
Geomatics Engineering,
Industrial Engineering,
Industrial Applications,
Machine Theory and Dynamics,
Manufacturing,
Mechanical Engineering,
Mechanics,
Mechatronics,
Medical,
Modeling and Simulation,
Physics Engineering,
Robotics,
Textile Engineering,
Health in Engineering

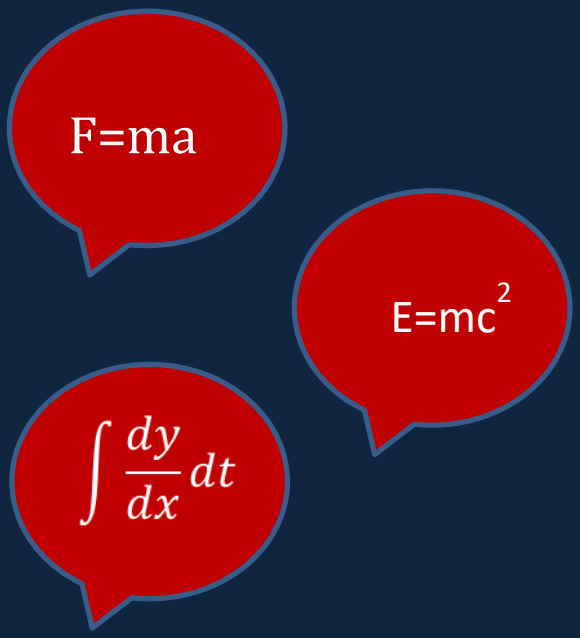

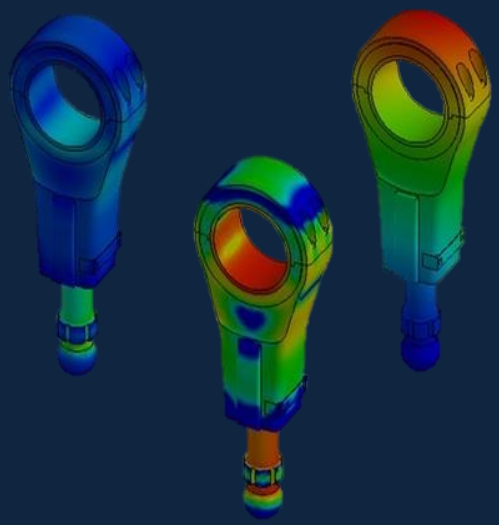

Volume: 03 / Issue: 03 / December 2019

Available online at www.dergipark.gov.tr

INTERNATIONAL ADVANCED RESEARCHES
and
ENGINEERING JOURNAL

Journal homepage: www.dergipark.gov.tr/iarej

e-ISSN: 2618-575X

International
Open Access

Volume 03
Issue 03

December, 2019

International Advanced Researches and Engineering Journal (IAREJ) is a double-blind peer-reviewed and publicly available online journal that has Editorial Board (http://dergipark.gov.tr/iarej/board). The editor in chief of IAREJ welcomes the submissions that cover theoretical and/or applied researches on **Engineering** and related science with Engineering. The publication language of the Journal is **English**. **Writing Rules** are given in Author Guidelines (http://dergipark.gov.tr/iarej/writing-rules). IAREJ publishes **original papers** that are research papers and technical review papers.

IAREJ publication, which is **open access**, is **free of charge**. There is no article submission and processing charges (APCs).

IAREJ is indexed & abstracted in:

Crossref (Doi beginning: 10.35860/iarej.xxxxxx)
Directory of Open Access Scholarly Researches (ROAD)
Directory of Research Journals Indexing (DRJI)
Google Scholar
Index Copernicus (ICI Journal Master List)
Journal Factor
J-Gate
Rootindexing
Scientific Indexing Services (SIS)
WorldCAT

Authors are responsible from the copyrights of the figures and the contents of the manuscripts, accuracy of the references, quotations and proposed ideas and the Publication Ethics (http://dergipark.gov.tr/iarej/page/4240).

The publication supporter of the journal is planning to change the URL of the IAREJ website to **https://dergipark.org.tr/en/pub/iarej** by 2020.

Available online at www.dergipark.gov.tr

INTERNATIONAL ADVANCED RESEARCHES
and
ENGINEERING JOURNAL

Journal homepage: www.dergipark.gov.tr/iarej

e-ISSN: 2618-575X

International
Open Access

Volume 03
Issue 03

December, 2019

Table of Contents

Available online at www.dergipark.gov.tr

INTERNATIONAL ADVANCED RESEARCHES
and
ENGINEERING JOURNAL

Journal homepage: www.dergipark.gov.tr/iarej

International
Open Access

Volume 03
Issue 03

December, 2019

e-ISSN: 2618-575X

Review Article

Using of recycling materials in the construction sector

Ahmet Ünal [a,*] ***and Ali Öz*** [b]

[a]*Erzurum Technical University, Engineering and Architectural Faculty, Erzurum and 25070, Turkey*
[b]*Atatürk University, Narman Vocational High School, Erzurum and 25240, Turkey*

ARTICLE INFO

Article history:
Received 10 October 2018
Revised 25 September 2019
Accepted 28 September 2019

Keywords:
Aggregate
Bituminous material
Glass waste
Recycling

ABSTRACT

The fact that the population is increasing day by day requires more careful use of limited resources. Making these limited resources reusable after use has a separate meaning in terms of both the environment and the economy. Therefore; the importance of recycling activities is increasing day by day. The managers of the countries; Due to the increasing importance of recycling activities, they make legal arrangements to encourage these activities. Particularly in the construction sector, because of the extensible resources are used extensively, recycling activities are applied intensively. Within the scope of the study, the recycling activities (asphalt, used vehicle tires, slags, glass waste and marble waste) in the construction sector were researched. In addition, applications after recycling of materials have been examined. The economic contribution of the acquisition of materials through recycling has been expressed.

1. Introduction

The fact that the world population is growing rapidly brings with it many problems. One of these problems is that waste materials are produced by using industrial materials whose consumption is continuously increasing. Removal of these waste materials from the production facilities is of great importance. The removal of industrial wastes and the availability of suitable waste for these wastes are virtually impossible, especially in large cities. In addition to these negativities, excessive and unplanned use of natural resources may cause these resources to diminish or even disappear in the years to come [1].

Many countries are focusing on the policy of recycling these resources in order to avoid excessive consumption of natural resources and to combat the emerging energy crises. Investigations has begun on recycling in Europe in the 1970s, and recycling efforts in Turkey, but has come to a position to be effective after the 2000s [2]. Turkey will be able to turn back backwardness in this sector by speeding up the application, but in this area. For this reason, policies that encourage recycling through legal regulations must be passed on first.

The recycling efforts started with the asphalt recycling activities that took place especially in the 1970s due to the oil crisis. Along with the oil crisis, countries have experienced great difficulties in meeting oil demand, which has led to the start of their recycling efforts. Asphalt recycling is defined as the process of stripping the finished asphalt within certain criteria and reusing it in certain ways [3].

The recycling of natural resources is mainly done in the construction sector, textile sector, industrial sector and many other areas. In this study; the work carried out in the field of recycling in the construction sector is explained. The effects of the applications made using recycled materials on the desired values in the specifications are explained.

2. Literature Review

In particular, the materials used in our time will be harmful to nature, even if they are both remote and removed. Recycling is increasing the importance of day to day. In this part of the work, the studies on recycling in the construction sector are mentioned.

* Corresponding author. Tel.: *+90-444-5-388 / 2363.*
E-mail addresses: ahmet.unal@erzurum.edu.tr *(A. Ünal)*, alioz@atauni.edu.tr *(A. Öz)*
ORCID: 0000-0001-8277-6002 *(A. Ünal)*, 0000-0002-6590-3775 *(A. Öz)*
DOI: 10.35860/iarej.469185

Sefidehkhan [4] compared the properties of concrete produced using recycled aggregate (RA) at different rates and the properties of concrete produced using crushed stone in study. It has been determined that the concrete produced using 100% recycled aggregate is in a lower class than the concrete produced with 100% crushed stone aggregate. Hosseinnezhad [5] investigated the recycling of concrete waste to the use of compressible concrete. For this purpose, prepared 15 different concrete mixes which can be compacted into cylinders by using 0%, 25%, 50%, 75% and 100% recycling aggregates. Examined the mechanical and durability properties of the produced blends. Found that the use of recycle aggregates up to 25% did not significantly affect the mechanical properties. However, the effect of the use of recycling aggregates has been reduced as the dosage of cement decreases. Süme [6] has studied the usage of the recycling aggregate for concrete road cover. It has been concluded that the concrete pressure resistance increases as the RA utilization rate increases and the bending strength shows a rolling-out curve, and that the concrete produced with 100% cleaned RA gives maximum yield and the pressure resistance gives maximum result and it should be used as concrete road cover. Çağrıcı [7] conducted a study on the use of recycled materials obtained from construction and debris wastes on road superstructures. We have examined the effect of waste materials by applying a test path approximately 100 meters long at the Arnavutköy Bolluca site where all of the filler, subbase, plent-mix base and bituminous base plates of the materials produced by industrial scale production using demolition wastes are located.

Kaya [8] investigated the use of damaged or old asphalt coatings in new roads by scraping. As a result of researches, he found that recovering asphalt as much as possible from all over the world and our country reduces the consumption of natural resources with less aggregate and bitumen use. In this way, it has determined that economical profit is realized with decreasing the production costs of asphalt. Güner et al. [9] have worked on the selection of materials for environmentally conscious structures for the sustainable development model. As a result of analysis of the samples they examined in their studies, they obtained a table by creating subgroups as a result of the analysis of the headings and the headings in the selection of materials in ecological and sustainable structures. By analyzing the selected twenty sample projets on the chart, the effect ratings of the parameters included in the chart were determined and the obtained data was interpreted together with the sub parameters. Güner et al. [10] the construction industry has examined the recycling of building materials as a source of raw materials and recycling. In the works, recyclable materials are explained in the construction industry, waste is considered as a source of raw materials and applications in the world are mentioned.

Chen et al. reviewing 1639 articles on the topic of recycling in total with a three-stage literature review; they stated the deficiencies in the current studies and suggestions that would encourage the current studies [11]. Kisku et al. the aggregate in the waste concrete formed due to the demolition of buildings; emphasized the importance of using in recycling. They compared the properties of conventional concrete with prepared concrete by using demolition wastes in recycling. They have reached the conclusion that the properties of the concrete prepared using recycling aggregates are lower than those of conventional concrete. However, they stated that the desired properties can be obtained by using some additives and modified mixing approaches [12]. Li et al. highlighted the environmental and economic advantages of the application of recycled solid waste in road pavement. In particular, they examined the applicability of recycled asphalt pavement and steel slags on the road [13].

The intensive consumption of raw materials in many sectors leads to depletion of resources and increases the importance of recycling activities. There is no doubt that recycling activities are widely performed in many different fields. In this study, especially recycling activities in the construction sector are mentioned and application areas of recycling materials in transportation sector are explained.

In this study, the practices related to the recycling activities in the construction sector are mentioned. Furthermore, the applications of the materials obtained from these recycling activities in the transportation sector are explained and their contributions are expressed.

3. Material

The development of technology, the speeding up of countries' recycling efforts and the necessity of recycling efforts have resulted in the use of very different structural materials in the field of recycling. In this part of the work, the methods of recycling in the construction sector are explained. In addition, the structural positive effects of the materials used in the recovery are explained. In the scope of the study, old asphalt coatings, used vehicle tires, slags, glass wastes and marble wastes were investigated and determined the effects of using these materials.

3.1 Scratched old asphalt pavements

Recycling is achieved by using the material obtained by scraping from the existing road superstructure in the production of bituminous hot mix to be constructed (Figure 1). Both economic and environmental advantages are achieved by using bitumen and agglomerate, which have high economic value in existing road pavement layers, after they have passed certain operations, again on the road superstructure [14].

Figure 1. Asphalt Recycling [15]

Depending on the type of asphalt production plant, different amounts of scrapped asphalt can be used to save both bitumen and mixtures that meet asphalt specifications. There are many applications where the use of recycled materials in the base, binder and bituminous base layers has been successful. In general, asphalt is added at a certain rate with 10%, 10%, 20% and 35% of the amount of recycled asphalt in the bituminous base layer, resulting in a mixture of asphalt specification criteria.

3.2 *Used vehicle tires*

Tires whose tread depth has fallen below 1.6 mm become unusable because of their physical properties and lack of reliability. Most of the finished tires are used in recycling plants. Particularly in America and Europe, used automobile tires, which cause major environmental problems, are broken up and separated from steel wires (Figure 2).

After this process it is reduced to dust or granular size and used in various industries. Used vehicle tires are widely used especially in the concrete and cement industries after being recycled. According to the results of the tests made, the increase in the amount of ground vehicle tire usage was reached as a result of decreasing the volume weight, bending strength and compressive strength values of concrete unit. Accordingly, it has been determined that rubber-reinforced concrete can be used in low-volume-weighted situations or in undesirable situations where the carrier properties are desired.

3.3 Slags

Slag is a side product of iron production in blast furnaces in iron and steel plants in shown Figure 3. The slags produced during the steel production are used for road cover. Slag is used in the bituminous base layer 45% and in the binder layer35%.

It is known that, in the works carried out, the binder and bituminous base layers are generally used as artificial aggregates in slag asphalt mixtures at certain ratios. In addition to these studies, cement with no binding properties alone has achieved binding properties when used with cement. It has been proven in many studies in the literature that it has a very positive contribution to the physical and mechanical properties of slag concrete [1].

3.4 Glass

Glass between recyclable materials; although it is not as harmful as abandoning plastics to the environment or wasted paper, it is one of the most energy-saving substances when conversion is made. Also, since it is a simpler structure than a few raw materials in its structure, recycling is also very easy compared to others. Although asphalt mixtures have no positive effect on performance, they are preferred because they increase the visibility coefficient of road surface in concrete way [1]. Glass wastes increase the stiffness in asphalt mixtures but decrease the resistance against cracking which may occur at low temperatures is the biggest reason why glass wastes are not used**.**

Figure 2. Old vehicle tires recycling [16]

Figure 3. Slags recycling [17]

3.5 *Marble waste*

Recycling is very important in marble which constitutes 60% waste material during production and processing. The marble, which forms two types of waste, namely dust and piece, is recycled in different forms. The marbles emerging as waste in marble production and cutting facilities are used as coarse / fine aggregates in the basement and plent-mix base layers which are connected water at the road surface and are also used as filling materials at certain ratios in asphalt mixtures. Marble dust can be used as road superstructure material. Fine dust can be used to reduce filler voids [1]. Delays the decomposition of asphalt at high temperature. The investigations have shown that the marble dust added to the pavement delays asphalt aging considerably. Asphalt added marble increases the viscosity of asphalt. This reduces the formation of treads. Marble dust is called a marble filler. This filler can be used on asphalt with little stone filler (Figure 4).

Apart from that, marble is used in lime production, cement production and ready-mixed concrete production. Investigations to increase the durability of concrete using 10% marble filler in concrete.

Figure 4. Marble waste recycling [18]

Figure 5. Concrete waste recycling [22]

3.6 *Concrete waste*

Most of the construction and demolition wastes are concrete wastes. Although recycling of concrete is not as much as paper, plastic and similar materials, it is a recycling material that is important to realize and to bring it back to the economy (Figure 5) [19]. There are many different applications related to the recycling activities of concrete in many countries in the world. It is estimated that 175-370 million tons of construction and demolition waste is produced annually in European countries. 72% of these wastes are stored and 28% are brought to the market through recycling activities [20]. By recycling the construction and demolition wastes, raw material (cement and aggregate) production and energy consumption are prevented. Image pollution is prevented by recycling the construction waste that covers a certain area and volume in the environment. Less energy is consumed by using waste rather than using natural resources. In addition, it contributes to the economic development of the country [21].

Since the content of the mixtures used in the pavement layer in the road flexible pavements consists of aggregates of 90-95%, it is used as aggregate in the road pavements together with the recycling of waste concrete.

3.6 *Plastic waste*

In recent years, plastic products have been used extensively in many sectors. One of the most important reasons why plastic materials are flexible, easy to process, light and cheap. However, pollution that occurs after the use of these plastic wastes is an important environmental problem [23]. Because plastic wastes decay and dissolve in the environment much more difficult than other wastes. This increases the importance of recycling activities of plastic wastes. Although very new, plastics used in the automotive industry are recycled by pyrolysis. Solid products obtained by pyrolysis are used as additives in hot asphalt pavements.

Milled pet bottle; it can be used in asphalt pavement only within the scope of waste assessment, provided that it does not exceed 0.5%, furthermore it has no positive effect on asphalt mixtures [24].

3.7 Lime waste

The raw material of lime is a natural raw material containing calcium carbonate ($CaCO_3$) and magnesium carbonate in the limestone chemical structure [24]. In soil improvement works due to calcium content; soil expansion and contraction of the soil as a result of the physical changes that occur as a result of applications to eliminate damages. With lime stabilization, optimum water content increases in the short term, proctor densities decrease, plastic limit increases, liquid limit decreases and CBR values increase [25]. In the long term, the CBR value increases, the free pressure and shear strength values increase, and the stability against swelling and shrinkage

increases. It was stated that the stabilization studies using lime contributed to the positive results.

As a result of the study conducted with the aim of improving the road infrastructure by using fly ash and limestone, the CBR value of the ground was increased [26].

3.8 Roof Shingle Waste

Syringe pieces are milled and their effects on hot bituminous mixtures are examined. Marshall Test is used to determine the stability of hot bituminous mixtures prepared for this purpose.

Although the roof waste is not in general a serious problem so far; the fact that its use is increasing day by day shows the importance of taking precautions in advance (Figure 6). When the roof waste is ground and used at a rate of 1.5% with 50/70 bitumen, it gives positive results on bituminous hot mixtures [27, 28].

3.9 Iron Waste

Iron wastes collected from construction wastes can be reused after melting and shaping (Figure 7). There are applications that iron, copper and magnesium wastes collected from construction wastes are mixed with bitumen in certain proportions in order to give hardness and frictional strength to the asphalt. Particularly in stone mastic asphalt pavements prepared using these mixtures, positive results were achieved [31].

Figure 6. Roof shingle waste recycling [29]

Figure 7. Iron waste recycling [30]

Figure 8. Bituminous waste recycling [32]

3.10 Bituminous Membrane Wastes

Bituminous membrane wastes can be re-produced after shredding and grinding and can be used in asphalt construction (Figure 8). It was determined that the content of membrane wastes was 45% bitumen and 2.5% elephant material [32].

As a result of the studies, as a result of the recovery of bituminous membrane wastes, 45% bitumen can be used as binder in asphalt [24].

4. Results and Discussion

The importance of recycling activities is increasing day by day due to the limited natural resources, the continuous increase in population, global warming and environmental pollution. In order to use exhausted resources more effectively and efficiently, recycling activities need to be done in a widespread manner. In addition to all the economic advantages of recycling material, it provides protection of natural resources and prevents the pollution of the surrounding area by preventing the formation of waste areas. It is obvious that the recycling trend that started in Europe and in the World has started to spread in our country. However, the majority of licensed recycling companies are located in major cities where the industry is concentrated. In this case, about 50% of the idle materials in our country are recycled. In the absence of recycling plants, the natural resources used cannot be recycled.

It is a fact that the recycling systems established based on existing laws and regulations are not very effective and cannot reach the desired result. In order to avoid these negative consequences, a number of legal arrangements have to be made. The legal shortcoming of negative consequences comes not from the regulations but rather from the legal inadequacies. In order to remedy this situation, the Turkish Grand National Assembly did some work in 2006 and the following years, but the inadequacy of these studies is easily noticed because the desired performance in recycling is not taken.

Building materials and construction costs as well as within the entire industry occupies an important place in Turkey. Ministry of Environment and Urbanization General Directorate of Environmental Management Waste Management Department; In Turkey, 45 million tons of annual structural 10 million tons of waste during the first three years together with the Urban Renewal Act, the amount of material to be recovered is estimated at 6 million tons yearly [15]. For this reason, second hand use and dissemination of recycling practices are important for energy and resource conservation. As a result; considering recycling activities in Turkey is seen as lagging behind the state in Europe. General information about the recycling materials used in the construction sector is given in the Table 1 below.

Table 1. Application areas of recycling materials

Material	Advantages	Usage Areas
Scratched old asphalt pavements	Preventing the formation of waste areas, reducing the need for new materials	Bituminous mixtures, road construction
Used vehicle tires	Contribute to the economy, prevent environmental pollution	Asphalt mixtures and highways
Marble waste	Economy and environmental effect	Cement admixture, improving the properties of ground
Glass	Increasing the visibility of the road surface but causing a lower level of stability compared to conventional mixtures	Bituminous hot mixtures
Concrete waste	Contribute to the economy, prevent environmental pollution	Highway pavement, as concrete material
Plastic waste	Environmental effect	As additives in hot asphalt pavement
Lime waste	Preventing the formation of waste areas, prevent environmental pollution	Ground improvement
Roof shingle waste	Contribute to the economy, prevent environmental pollution	Bituminous hot mixtures
Iron waste	Economy and environmental effect	Flexible pavement
Bituminous Membrane Wastes	Contribute to the economy	Used as binder in asphalt

5. Conclusions

In recent years, there has been a significant increase in the formation of structural waste materials due to technological developments and variations in applications. It is known to everyone that the prevention of structural wastes at the source of waste management policies. Appropriate forms of evaluation of waste should be preferred, such as reuse, recycling, reproduction and energy conservation, as there is no world without waste.

The recycling and recovery of construction waste is also closely related to the economy of the country. It seems that the construction industry is of great importance in recycling. In the construction sector, energy and raw material savings are achieved by creating a potential raw material source through recycling. In the construction sector there are many construction materials that can be recycled during construction and demolition. The waste issues in the construction industry should be assessed well and the economic and environmental losses should be minimized. During the recycling of the recycled materials into the production system, new job opportunities are created and the employment of the economy is seen to be increasing. In the world where natural resources are limited, recycling activities have social, economic and environmental impacts, highlighting the importance of these activities. Recycling, which is one of the most important branches of waste management, is seen as an efficient economic investment by including recyclable wastes into the production process through various methods. For this reason, recycling is important both at the macro level in terms of environment and economy and in micro level in terms of businesses and consumers. As a result, it should not be forgotten that recycling has a large share in the protection of the environment and in the promotion of economic development and prosperity in terms of value added to the economy.

References

1. İpekci, C. A., Coskun, N., Karadayı, T. T. *The Importance of Recovered Materials Usage in Terms of Sustainability in Construction Sector*. Turkish Science Research Foundation, 2017. **10**: p. 43-50.
2. Oktem, B. *Integrated Application in Waste Management.* Batman University Journal of Life Sciences, 2016. **6**: p. 135-147.
3. Yılmaz, S., Kalkan, D. K. *Energy Security Concept: A Discussion in Light of 1973 Oil Crisis.* Journal of International Crisis and Political Research 1, 2017. p. 169-199.
4. Sefidehkahn, H. P., Simsek, O. *Investigation of Some Engineering Properties of Concrete Made with Recycled Aggregate in Different Ratios.* Journal of Polytechnic, 2018 **21**. p. 83-91.
5. Hosseinnezhad, H. *Effect of recycled concrete agregate on properties of roller compacted concrete.* Msc Thesis, Ege University, 2016.

6. Sume, E. *Usability of Recycled Aggregate as Concrete Pavement.* Msc Thesis, Karadeniz Technical University, 2016.
7. Cagrıcı, A. *Usability of the Construction and Demolition Waste Derived From Recycling Material For Superstructure of Highway*. Msc Thesis Yıldız Technical University, 2016.
8. Kaya, B. *Recycling of Bituminous Mixtures, Environmental Effects of Recycling and Cost Analysis.* Msc Thesis Istanbul Technical University, 2011.
9. Güner, C., Gökşen, F., Koçhan, A. *Investigation of Material Selection on Environmentally Sensitive Buildings for Sustainable Development Model.* Academia Journal of Interdisciplinary Scientific Research, 2017. **3**: p. 1-14.
10. Gürer, C., Akbulut, H., Kurklu, G. *Recycling in the Construction Industry and a Different Structure as a Source of Raw Material Reassessment of Materials.* 5th Industrial Raw Materials Symposium, 2004, İzmir.
11. Chen, W., Jin, R., Xu, Y., Wanatowski, D., Li, B., Yan, L., Pan, Z., Yang, Y. *Adopting Recycled Aggregates as Sustainable Construction Materials: A review of the Scientific Literature.* Construction and Building Materials, 2019. **218**: p. 483-496.
12. Kisku, N., Josji, H., Ansari, M., Panda, S. K., Nayak, S., Dutta, S. C. *A Critical Review and Assessment for Usage of Recycled Aggregates Sustainable Construction Material.* Construction and Building Materials, 2017. **131**: p. 721-740.
13. Li, J., Xiao, F., Zhang, L., Amirkhanian, S,. *Life Cycle Assessment and Life Cycle Cost Analysis of Recycled Solid Waste Materials in Highway Pavement: A review.* Journal of Cleaner Production. 2019. **233**: p. 1182-1206.
14. Oruc, S., Yılmaz, B., Mazlum, M. S. *Investigation of Reuse by Recycling Asphalt Pavements in Hot Mix Asphalt.* Science and Engineering Journal of Fırat University, 2018. **30**: p. 87-93.
15. İzgazete. [cited 25 September]; Availablefrom: https://www.izgazete.net/belediye/atik-asfaltla-10- geri-donusum-saglaniyor-h17484.html
16. Maksangrup. [cited 25 September]; Availablefrom:https://www.maksangrup.com.tr/index.php /lastiklerin- geri-donusumu/
17. Belmetal. [cited 25 September]; Available from: http://belmetal.com.tr/aluminyumgeridonusum/aluminyum-curuf-alimi
18. Formendergi. [cited 25 September]; Available from:http://formendergisi.com/icerik/detay/150/mermer-artiklarinin-donusumu-icin-15-milyon-euroluk-yatirim
19. İzto. [cited 25 September]; Available from: http://www.izto.org.tr/portals/0/argebulten/6kentseldonusumatagi.pdf Accessed Date: 24.04.2018. (Recycling Attack in Urban Transformation, Nursel Kılıç, İzmir Chamber of Commerce, AR&GE BULLETİN 2012 December _Sectoral)
20. Ölmez, E., Yildiz, Ş. *Construction and Demolition Waste Management and Planned Istanbul Model.* Urban Management, Human and Environmental Problems Symposium, 2008, İstanbul.
21. Batman, M., *Investigation Of The Usability Of Concrete Experiment Sample Wastes As Recycled Aggregate.* Msc Thesis, Atatürk University, 2018.
22. Çağrıcı, A. *Usability of the Construction and Demolition Waste Derived from Recycling Material for Superstructure of Highway*. Msc Thesis, Yıldız Technical University, 2016.
23. Al-Oabadi, S. A. M. *Recycling Plastics Used in the Automotive Industry by Liquefying with Pyrolysis Method in Hot Asphalt Mixture.* Msc Thesis, Selçuk University, 2018.
24. KHL. [cited 25 September]; Available from: https://www.khlgroup.com/events/demolitionconference-turkey/assets/ibrahim-sonmez.pdf
25. MTA. [cited 25 September]; Available from: http://www.mta.gov.tr/v3.0/bilgimerkezi/kirec
26. [cited 25 September]; Available from:https://docplayer.biz.tr/6869531Yuksek-plastisiteli-bir-kili-kirecilestabilizasyonuyukseklisans-insaat-muh-melih-murat-kizilcelik.html
27. Ontürk, K., Firat, S., Vural, I., Khatip, J. M. *Improvement of Road Sub-base Fill by Using Waste Marble Dust and Fly Ash.* Journal of Polytechnic, 2014. **17**: p. 35-42.
28. CSB. [cited 25 September]; Available from: https://yalova.csb.gov.tr/insaatsektorunde-hangi-atiklar-geri-donusturulebilir-haber-21870
29. Cati Geri Donusum. [cited 25 September]; Available from: http://catigeridonusum.com/Urunler-Metal-Hurdasi
30. SBB. [cited 25 September]; Available from: http://www.sbb.gov.tr/wp-content/uploads/2018/11/Yasin Öcal.pdf
31. Otomasyon dergisi. [cited 25 September]; Available from: http://otomasyondergisi.com.tr/bolumler/mercek/demir-celikfirinlarindakiatigingeridonusumu
32. Ibrahim Sonmez. [cited 25 September]; Available from: https://docplayer.biz.tr/2790327-Insaat-atiklarinin-asfaltta-geri-donusum-malzemesi-olarak-kullanilmasi-dr-ibrahim-sonmez.html

Available online at www.dergipark.gov.tr

INTERNATIONAL ADVANCED RESEARCHES
and
ENGINEERING JOURNAL

Journal homepage: www.dergipark.gov.tr/iarej

e-ISSN: 2618-575X

International Open Access

Volume 03
Issue 03

December, 2019

Review Article

A review study on ladle slag detection technologies in continuous casting process

Hakan Kapusuz [a], ***Mehmet Ali Güvenç*** [a] ***and Selçuk Mıstıkoğlu*** [a,*]

[a]*Department of Mechanical Engineering, Iskenderun Technical University, İskenderun, Hatay, 31200, Turkey*

ARTICLE INFO

Article history:
Received 07 May 2018
Revised 10 September 2019
Accepted 23 October 2019

Keywords:
Continuous cast
Ladle slag detection
Vibration

ABSTRACT

In steel production, continuous casting method using BOF or EAF is increasing day by day. However, the complex nature of the continuous casting process poses many challenges for steelmakers. During the general steel production process of liquid steel, the state of ladle slag penetration into liquid steel is one of the most influential factors in steel quality. If the ingress of ladle slag into liquid steel cannot be controlled, undesirable results in terms of poor quality, safety and castability can occur. Generally, ladle slag consists of oxides such as CaO, SiO 2, Al 2 O 3, MgO. In conventional methods, the operator prevents the slag entry by manually controlling it. This method is performed directly by the operator, so the error rate is high. For this reason, it is not desired to be used by steel producers who want high quality products. In this context, steel mills carry out various activities to separate slag from liquid steel. The development of sensor technologies has accelerated the slag detection process. Acceleration and magnetic sensors are among the most widely used methods in this field. In this study, the systems used worldwide for the determination of slag in the continuous casting process were investigated and presented. The advantages and disadvantages of these systems are discussed. The detection methods by considering investment cost, detection time, accuracy were compared and presented. In the scope of this study, it is seen that every method has own advantages and disadvantages over other.

1. Introduction

Continuous casting of steel can be in many formats such as billet, bloom, round shape, beam blank, thin slab or slab. Whatever the semi-final product is some important points are the same. These points are also valid for both BOF and EAF route, Figure 1 [1]. Preventing ladle slag carryover transport to the tundish is one key element of them.

Ladle slag is necessary to adjust steel chemistry on ladle furnace side. A typical ladle slag consists of mainly oxide compounds. A typical slag sample is given in Table 1. The sample is taken after the final ladle treatment. For alloying and deoxidizing of steel yield it can be in certain range.

On the other hand, it can be a nightmare for continuous casting process from many perspectives regarding equipment and human safety, product and semi-product quality, and castability. To get rid of ladle slag is a major task for caster workers regarding the hazardous effects of slag carryover [2].

As seen in the literature investigation above, there are many efficiently methods to detect of carryover slag during the transportation of liquid steel from ladle to tundish. However, in the literature, it is seen that there are not sufficient academic studies examining the advantages and disadvantages of these methods as well as the negative effects of carryover slag. In this study, a research was carried out on the negative effects of slag on production process and product quality. In order to eliminate these negative effects, a comparative overview of some common methods used in the detection of carryover slag is given. End of this study, it can be commented that the required reaction time to close ladle slide gate which controls the flow plays a vital role for separating steel and carryover slag. This issue is a key indicator for the successful rate of the slag detection system.

* Corresponding author. Tel.: +90 (326) 613 56 00; Fax: +90 (326) 613 56 13.
E-mail addresses: hkapusuz@gmail.com *(H. Kapusuz)*, mali.guvenc@iste.edu.tr *(M.A. Güvenç)*, selcuk.mistikoglu@iste.edu.tr *(S. Mısıroğlu)*
ORCID: 0000-0001-5938-5759 *(H. Kapusuz)*, 0000-0002-4652-3048 *(M.A. Güvenç)*, 0000-0003-2985-8310 *(S. Mısıroğlu)*
DOI: 10.35860/iarej.421657

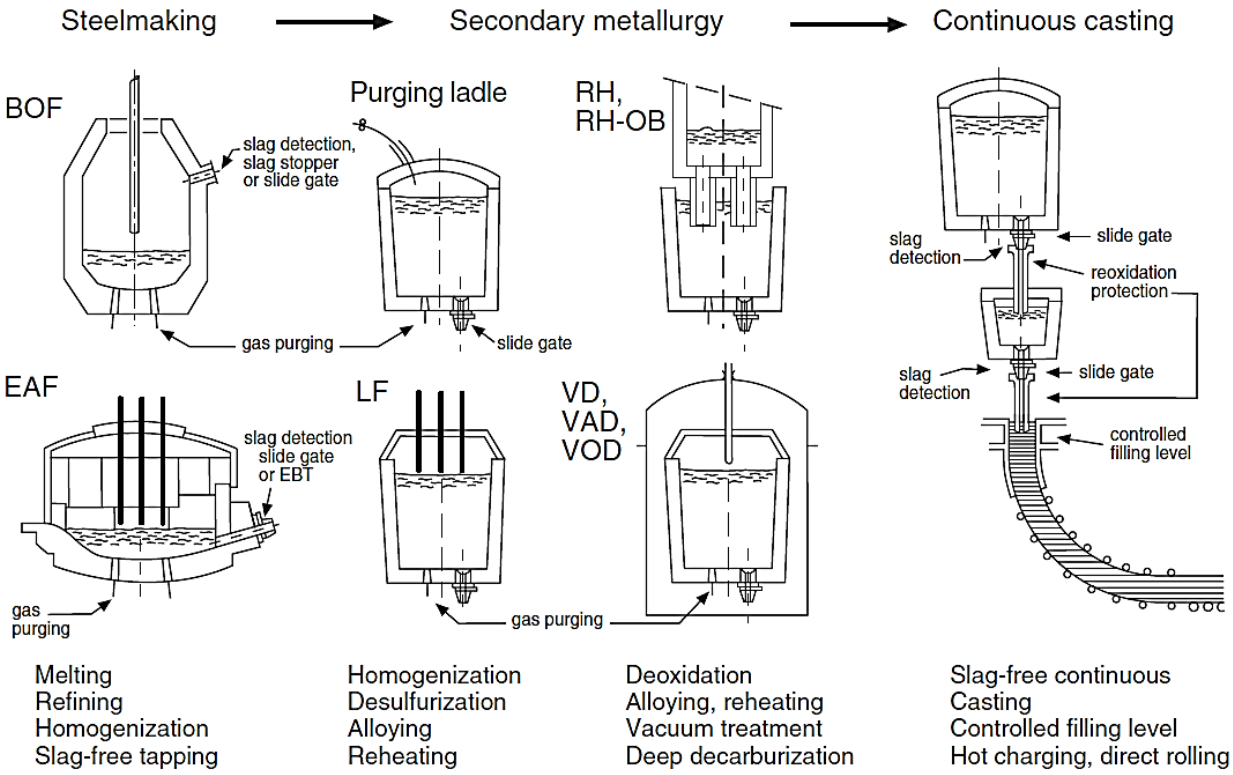

Figure 1. Liquid steel journey both in BOF and EAF route [1]

Table 1. % chemical analysis of ladle slag

SiO_2	CaO	Al_2O_3	MgO	FeO	S	MnO	K_2O	TiO_2	Fe	P_2O_5	Fe_2O_3	Na_2O
11.8	52.2	23.2	2.9	2.2	0.52	2	0.00	0.13	3	0.36	0.50	0.065

2. Effects of Ladle Slag on Continuous Casting Process

First of all, the ladle slag carryover is very detrimental to tundish refractory material so tundish life. Even if the tundish walls are well coated with high resistant materials, the ladle slag will dissolve it due to its content, temperature and volume. If the slag carryover is not prevented at the end of draining of every ladle and gathers in the tundish during whole tundish sequence, the slag can dissolve the refractory material of tundish wall[3, 4]. The amount of slag gathered in the tundish can be increase at each ladle. At the weakest point, generally at the slag level, the liquid steel can melt the tundish wall due to dissolved refractory lining, as seen in Figure 2. Related to this issue when the slag volume increases in tundish then tundish life will be shorter [5]. In other words, due to eroded tundish refractory, casting must be stopped wall to eliminate the risk of process safety [6].

Additionally, shorter life of tundish results in casting costs. The second effect of the slag carryover is the quality due to the slag entrainment. For high-quality steel, the slag carryover must be removed. It should not be mixed with carryover slag and synthetic slag (flux) on tundish. Inclusions are divided into 2 categories, endogenous and exogenous [7, 8]. Endogenous inclusions are a result of deoxidation, on the other hand, exogenous inclusions are the result of reoxidation. The ladle slag carryover is assumed the source of exogenous inclusions [8]. Excessive slag carryover will result in inclusions in final products such as coil or wire rod. In rolling process, inclusions resulted in by the slag carryover, which cannot be deformed, Figure 3 [8]. Crack, breaking, tears or slivers can become in view due to the presence of undeformed inclusions. Especially higher content of FeO and MnO in slag result in the greater potential of reoxidation. These weak oxide compounds react with the dissolved Al in liquid steel during steel slag interaction to form Al_2O_3. Especially slivers in the final product are attributed to Al_2O_3 content of solidified steel[9, 10].

Figure 2. Steel leakage through tundish wall due to carryover slag erosion

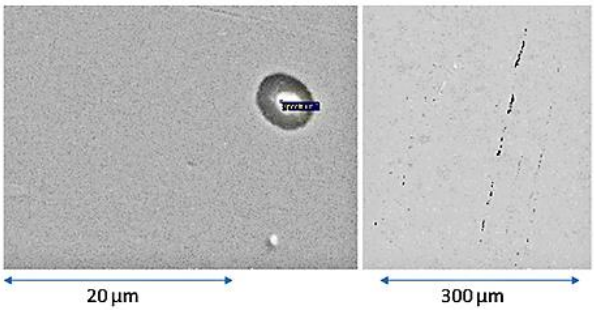

Figure 3. Example of an inclusion in spring steel in tundish sample (left) and in wire deformed in rolling direction (right) [8]

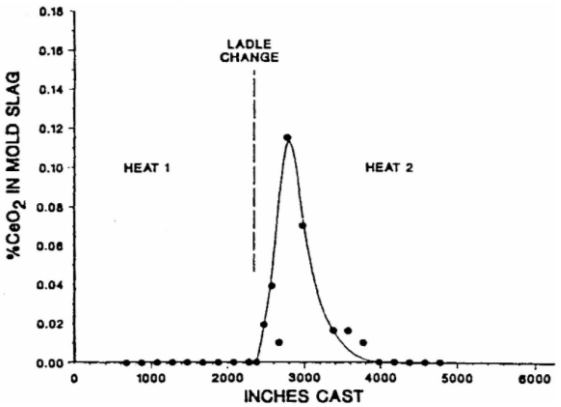

Figure 4. Tracer in mould slag in subsequent two heats [15]

Many studies investigate the strict relation between inclusions and product quality [7, 11]. For special steel products such as tire cord [12] or IF steels [13] it is very important to avoid slag carryover from the ladle to tundish. Additionally, the direct strip casting technology is growing day by day because of their many benefits. To produce thin steel strips inclusion control plays a vital role [14], in other words, slag detection becomes a very important element.

The third point is castability due to the slag entrainment into mould flux. Castability is a generic term referring how hard the casting process is. When the ladle carryover slag enters the mould zone through tundish bottom hole the mould flux behavior will be changed due to the interactions between ladle slag and mould flux. In a plant trial CeO2 was added to tundish slag as a tracer to detect tundish slag then it was seen in mould slag, Figure 4 [15].

Lubrication behavior of mould flux very depends on its chemical content [16]. Little changes in chemical content makes big differences in mould powder performance [17] and so lubrication. When lubrication is changed the mould friction between solid shell of steel and mould wall will be higher, which is not desired. The control of mould operations will be harder for operators, at worst scenario breakout happens due to the higher friction or slag entrainment into the liquid steel [18]. Additionally, when the end of the sequence has started the possibility of breakout is higher due to the lower height of steel in a tundish. Excessive slag that is gathered during the whole sequence of casting process in the tundish promotes to suck of it towards the steel shell. This will return us to safety, maintenance cost, and of course yield [15, 19, 20].

3. Common Ladle Slag Detection Methods in Continuous Casting Process

After above mentioned reasons it is very crucial to take under control of the ladle slag carryover in all continuous casting processes such as billet casting, slab casting or beam blank. There are many common methods used continuous casting facilities from manual detection to sensor-based detection systems.

Historically first slag control system starts with a human [21]. The manual detection is performed by caster operator. The ladle slag carryover comes after draining of steel at the end of the ladle. The operator sees the slag carryover on the tundish surface near ladle shroud. When the operator sees the slag, closes slag slide gate manually. Thus, the operator closes the slide gate after an amount of carryover slag passes to tundish. Apart from a late detection operator also need time to react. The operator distinguishes the ladle slag carryover from steel by their color differences and its behavior similar to boiling near ladle shroud submerging point. Procedure very depends on caster experience. In most cases, the same operator acts differently[22–24]. In some cases, the operator closes ladle slide gate very late and too much slag enters tundish and or mould zone or closes very early. In some plants when there is excessive slag carryover on the tundish surface, tundish is filled by steel and slag is overflowed to another empty vessel. It can be clearly seen that the slag carryover detection by a human has many open points [25].

Image processing and ultra-sonic reflection based detection [20] methods have also open points due to the late detection of slag carryover. These type of detection systems detect the carryover slag when the carryover slag enters the tundish zone that is very late for today's requirements. The only difference from the human controlled system is reaction time[26].

Unlike tundish zone detection systems, the electromagnetic slag detection system is located just bottom of the ladle near slide gate zone. Thus early detection is enabled, in other words, the slag does not reach tundish. This method is first used by AMEPA company and commonly used in steel plants, Figure 5 [27].

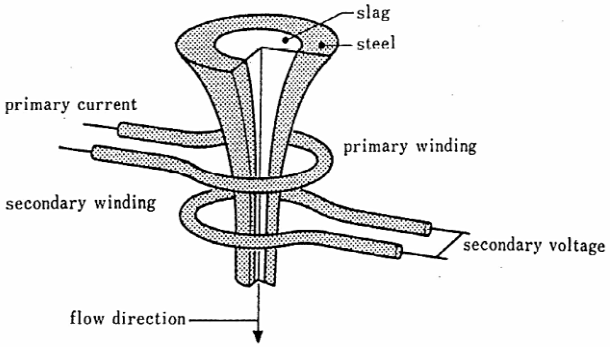

Figure 5. Electromagnetic ladle slag detection [27]

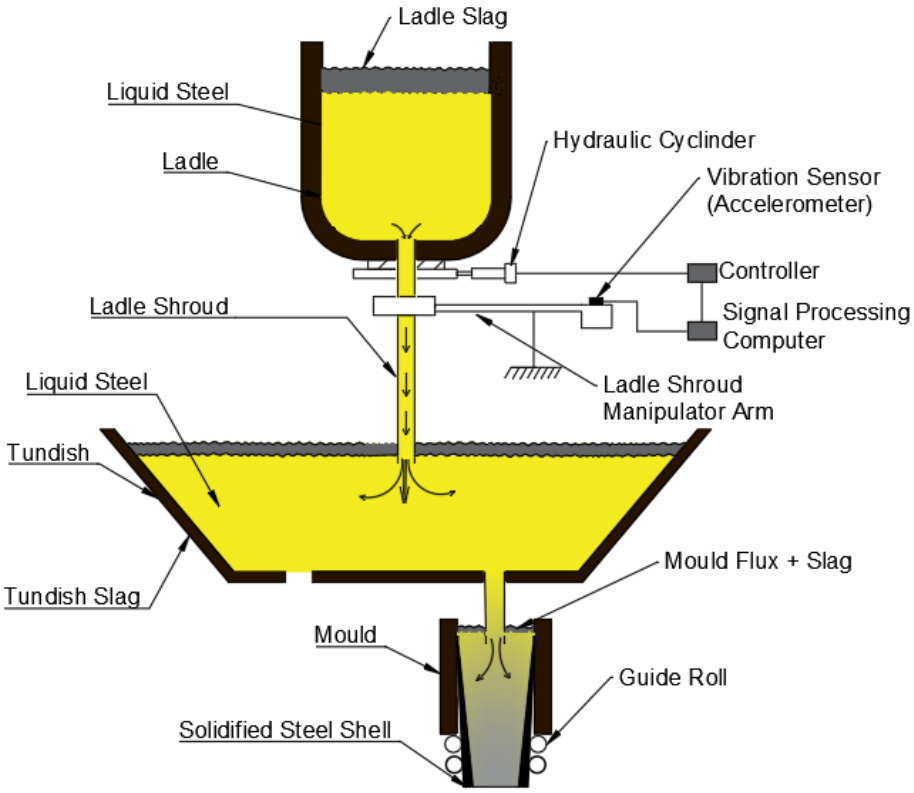

Figure 6. Schematic of continuous caster

Basically, there are two coils in the system: one of them is the current supplier and the second one is the secondary coil. When the current passes through the first coil an electromagnetic field is generated in the steel flowing through ladle nozzle. The electrical conductivity of slag is lower than that of liquid steel, the ratio is 1:10.000 at 1600ºC [28]. Before slag entering stage entire flowing composition is liquid steel having high electrical conductivity wherein larger magnetic field. When slag starts to come through coils, the magnetic field will decrease. The magnetic field is converted and collected via secondary coil [27, 28]. The deviation in electrical conductivity of the flowing stream means the amount of slag. By online monitoring of magnitude and phase of voltage that is induced in secondary coil, carryover slag can be detected very early [29]. Like other methods, this method has some disadvantageous. Because of the high-temperature environment, all components including coils must be thermal insulated. High temperature harms the coils [30] wherein system malfunctions can occur. Apart from this, all the ladles have to be equipped with necessary detection equipment, in other words, investment cost and maintenance cost are higher. Additionally, continuous casting is a sequence casting process. Whenever a new ladle arrives at the turret, an operator must plug the communication cable of the electromagnetic detection system. Lastly, according to a study [29], the slag must be close enough to the measuring coils to get a guaranteed detection otherwise wrong results can be gotten[4].

One of the promising methods is vibration based slag detection system. To overcome many above-mentioned disadvantageous of another type of detection systems that are high cost, hard installation, short service life, etc. vibration based detection system arose[31, 32].

When steel flows through the ladle nozzle it creates a certain vibration. The same condition is also valid for the slag. The vibration is transported through all solid part equipment. The continuous casting process, which is drawn not to scale, is also described in figure 6.

Vibration due to the steel and or slag flow are transmitted through the manipulator arm oscillates the accelerometer inside the vibration sensor which converts the motion to electrical signals [33], Figure 7 [34].

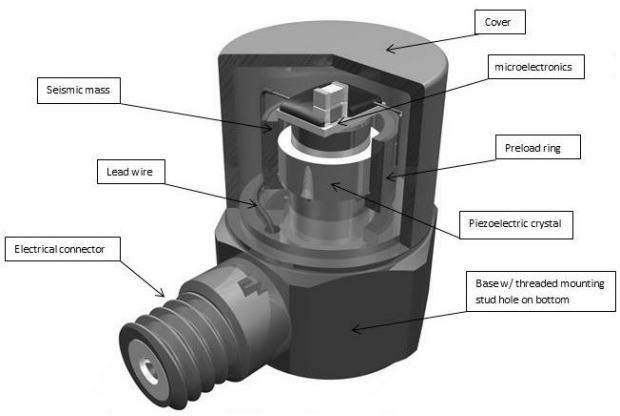

Figure 7. An accelerometer converts vibration to electrical signal [34]

Tablo 2. Comparison of detection methods

Main Properties	**Human Eye Based**	**Ultrasonic Reflection Based**	**Image Processing Based**	**Electromagnetic Based**	**Vibration Based**	**Acoustic Based**
Investment Cost(C)	0.5	1	0.75	1.5	0.75	1
Detection Time(T)	1.5xT	1xT	1.5xT	0.5xT	0.5xT	0.5xT
Accuracy(A)	0.5	0.75	0.75	0.9	0.9	0.75
Bad Aspects	Operator Experiences	Old Technology	Raw Signal Tuning	Hard Installation and Maintenance	Raw Signal Tuning	Raw Signal Tuning

The vibrations originated from steel and slag there are many vibration sources in the steel plant. These other sources can trigger false alarm leading to being closed slide gate very early. At the end remaining steel in the ladle will increase, which will result in decreasing overall yield. Thus, advanced signal processing including denoising is very crucial. In this study, nothing will be mentioned about signal processing, but the results of trials. There are many companies in the market dealing with this business and every one of them has a different algorithm [35].

Apart from the accelerometer based detection system, there is one another. It is almost the same like accelerometer type detection system. The only difference is sensor type which is acoustic. Sound waves created by steel and or slag makes pressure changes through the ladle shroud manipulator arm [36, 37]. The sound waves pass through the manipulator arm like vibration. These pressure changes are converted to the certain electrical signal via an acoustic sensor which is mounted directly onto manipulator arm surface. The latter is same just like in accelerometer-based detection system. Main disadvantages of this system are fine-tuning [18].

4. Results and Discussion

The ladle slag carryover must be under controlled due to the process safety, quality and castability. There are many methods used in steel plant todays and there is no perfect system nowadays. Every method has its own advantageous and disadvantageous. Ideal detection system should have lower investment cost and maintenance, longer service life, easy to installation. Some advantages and disadvantages were given in Table 2 created by considering investment cost, detection time, accuracy and bad aspects.

As shown Table 2, each method has its advantages and disadvantages over the other. However, generally sensor-based detection system seems feasible and affordable.

5. Conclusion

It can be clearly concluded from review:

- The slide gate controlled by man is not stable and feasible due to the increasing customer demands.
- Ultrasonic-reflection and image processing methods [20] are not suitable due to the late detection.
- Electromagnetic type detection system is common method among steel producers. On the other hand, it has very high costs, maintenance problems and hard installation procedures [27–30].
- Vibration based slag detection system is cheaper than electromagnetic slag detection system regarding investment and maintenance cost.
- Acoustic based detection system is like vibration based detection system. They have same advantageous and disadvantageous.
- Fine-tuning is still a challenging issue for vibration and acoustic based detection system. The performance of the systems very depends on their fine-tuning regarding signal processing.
- For 5 and 6, early alarm can be triggered due to the external vibrations such as human interventions, operator tasks, turret movement, etc. There are many vibrations a sound sources in steel plants causing false alarm. Due to the external sources in some heats, the ladles can be closed early without there is slag. This will lead to decrease yield.

Acknowledgments

This work was supported by the Iskenderun Iron & Steel Works Company scope of Master of Science Thesis of Hakan Kapusuz. We would like to thank Iskenderun Iron & Steel Works Company for their support.

References

1. Oberbach M. *High Grade Refractories for Clean Steel Technology.* In: Steel Technology International, 1991. **26:** pp 169–176.
2. Ozturk M., U. Korkut, *Investigation of mechanical and microstructural performance of alkali activated electrical arc furnace slag mortars.* International Advanced Research and Engineering journal, 2019. **03:** p. 55–59.
3. Madias J., *Electric Furnace Steelmaking*. 2014, Elsevier Ltd.
4. Li P.Y., D.P. Tan., X.H. Pan, B.Y. Lin, *Steel water continuous casting slag detection system based on wavelet.* Key Engineering Materials, 2007. **353:** p 3067–3071.

5. Yoshitani Y., *Contribution of Control System to Energy Savings in Steel Works.* IFAC Proceedings Volumes, 1983. **16:** p 25–38.
6. Takács G., K. Ondrejkovič, G. Hulkó, *A low-cost non-invasive slag detection system for continuous casting.* IFAC-PapersOnLine, 2017. **50:**438–445.
7. Zhang L., B.G. Thomas, *Inclusions in continuous casting of steel*. XXIV National Steelmaking Symposium2, 2013. **26:**138–183.
8. Louhenkilpi S., *Continuous Casting of Steel*. In: Treatise on Process Metallurgy. 2014, Elsevier Ltd., pp 373–434.
9. Pistorius P. C., *Slag carry-over and the production of clean steel.* Journal of the Southern African Institute of Mining and Metallurgy,2019. **119:** 557–561.
10. Varanasi S, Plant VS, Madhava V, et al *Slag Modeling for Effective Desulphurization in Ladle Furnace Refining*, APM 2019 conference, 2019.
11. Sanam V., P. K. Patra, *Reduction of Slivers Due To Nonmetallic Inclusions in Continuous Casting.* Materials Science and Technology, 2009. p. 1031–1041.
12. Zhang L., *State of the Art in the Control of Inclusions in Tire Cord Steels - a Review*. Steel Research International, 2006. **77: p.** 158-169.
13. Qin Y., X. Wang, L. Li, F. Huang, *Effect of Oxidizing Slag on Cleanliness of if Steel during Ladle Holding Process*. Steel Research International, 2015. **86:** p.1037–1045.
14. Holappa L, Wijk O., *Inclusion Engineering*, 2014, 1st ed. Elsevier Ltd.
15. Sahai Y, T. Emi, *Tundish Technology for Clean Steel Production*, 2008. World Scientific Publishing Co. Pte. Ltd.
16. Mills KC, A.B. Fox, Z. Li, R.P. Thackray, *Performance and properties of mould fluxes*. Ironmaking & Steelmaking, 2005. **32:** p. 26–34.
17. Ludlow V., B. Harris, S. Riaz, A. Normanton *Continuous casting mould powder and casting process interaction: why powders do not always work as expected.* Ironmaking & Steelmaking, 2005. **32:** p. 120–126.
18. Dede S., F. Altay, *Biosensors from the First Generation to Nano-biosensors.* International Advanced Research and Engineering Journal, 2018. **02:** p. 200–207.
19. Luk'yanov SI, Suspitsyn ES, Pishnograev RS, Krasilnikov SS, *Survey of melt stream infrared radiation parameters at various stages of steel tapping from basic oxygen furnace.* International Journal of Advanced Manufacturing Technology, 2017. **88:** p. 595–602.
20. Berner K., *Detecting method for slag carry-over in steel production*, 1996.
21. Zhang Z., L. Bin, Y. Jiang, *Optik Slag detection system based on infrared temperature measurement.* Optik - International Journal for Light and Electron Optics, 2014. **125:** p. 1412–1416.
22. Sandberg E., B. Lennox, P. Undvall, *Scrap management by statistical evaluation of EAF process data.* Control Engineering Practice, 2017. **15:** p. 1063–1075.
23. Raghavendra K., S. Sarkar, S.K. Ajmani, et al. *Mathematical modelling of single and multi-strand tundish for inclusion analysis.* Applied Mathematical Modelling, 2013. **37:** p. 6284–6300.
24. Bhattacharya D., A. Mishra, G.P. Poddar, S. Misra, *Case study of severe strip breakage in rolling mill of Thin Slab Casting and Rolling (TSCR) shop of TATA Steel, Jamshedpur.* Case Studies in Engineering Failure Analysis, 2016. **5–6:** p. 15–22.
25. Singh S., *Continuous Casting*. In: Reference Module in Materials Science and Materials Engineering, 2018. p. 1-11.
26. Chakraborty B, Sinha, BK *Development of caster slag detection system through imaging technique*. International Journal of Instrumentation Technology, 2011. **1(1):** p. 84-91.
27. Chen D., H. Xiao, Q. Ji, *Vibration Style Ladle Slag Detection Method based on Discrete Wavelet Decomposition.* IEEE, 2014. p. 3019–3022.
28. Tan D, S. Ji, P. Li, X. Pan, *Development of vibration style ladle slag detection methods and the key technologies.* Science China Technological Sciences, 2010. **53:** p. 2378–2387.
29. Wolfgang Theissen, E. Julius, R. Franz, *Method and Apparatus for the Detection of Slag Co-Flowing Within a Stream of Molten Meta*l, 1989.
30. Tan D.P., L. Zhang, A. Bin, *A WP-based nonlinear vibration sensing method for invisible liquid steel slag detection.* Sensors and Actuators, B: Chemical, 2014. **202:** p. 1257–1269.
31. Yang J., I. Tian, A. Fei, A New *Vibratıon Ladle Slag Detectıon System*, 2014. 285–291.
32. Kato H., M. Yamasita, *New Automation and Control Technology of Slab Caster.* IFAC Proceedings,1987. **20:** p. 253–258.
33. Piccinini A., V.P. Campagnoni, S. Ierace, F. Floreani, *A vibrational approach to Slag Sensing System: development and industrial application*. IFAC-PapersOnLine, 2016. **49:** 1412–1417.
34. ICP-accel1.jpg (655×464). [cited 2019 3 July]; Avaliable from: http://www.pcb.com/contentstore/mktgcontent/webimages/resources/techsupport/ICP-accel1.jpg.
35. Wenfang G., *Formation and Prevention of Sliver Defects on the Surface of Cold-rolled Strip, 2012*. **402:** p. 221–226.
36. Zhang Q, J. Wang, Y. Zhang, G. Xu, *Numerical simulation and manifold learning for the vibration of molten steel draining from a ladle.* Journal of Vibroengineering, 2013. **15:** p. 549–557.
37. Yang Z, Y. Wang, J. Rao, Z. Peng, *Control and optimizing of unstable state in continuous casting process with automatic system*. Advanced Materials Research, 2012. **472–475:** p. 3057–3062.

Available online at www.dergipark.gov.tr

INTERNATIONAL ADVANCED RESEARCHES
and
ENGINEERING JOURNAL

Journal homepage: www.dergipark.gov.tr/iarej

e-ISSN: 2618-575X

International Open Access

Volume 03
Issue 03

December, 2019

Research Article

PAPR reduction performance of bat algorithm in OFDM systems

Yüksel Tokur Bozkurt [a,*] ***and Necmi Taşpınar*** [b]

[a]*Department of Electronics and Automation, Voc. Sch. of Technical Sciences, Gaziantep University, Gaziantep, 27310, Turkey*
[b]*Department of Electrical and Electronics Engineering, Erciyes University, Kayseri, 38280, Turkey*

ARTICLE INFO

Article history:
Received 13 March 2018
Revised 10 February 2019
Accepted 02 October 2019

Keywords:
Bat algorithm
OFDM
PAPR
PTS

ABSTRACT

The progression in technology requires improved modulation techniques for wideband digital communication systems. Orthogonal frequency division multiplexing is efficacious systems to fulfill high-speed data transmissions needs. However, high peak-to-average power ratio (PAPR) is one of the significant limitations on the performance and power efficiency of OFDM systems. Due to industrial and scientific relevance, the assessment of the PAPR reduction has become popular subject in the current decade. This study presents the combination of bat algorithm with partial transmit sequence scheme as an efficient PAPR reduction method with an alleviated computational load. A set of simulations with different partial transmit sequence schemes are performed to comparatively evaluate the PAPR reduction performance of the partial transmit sequence based on bat algorithm scheme in OFDM system. The simulation results elucidate that BA-PTS scheme can provides better PAPR reduction performance with less computational load.

1. Introduction

In past few decades, orthogonal frequency division multiplexing system has attracted considerable interest by offering distinctive features like high spectrum efficiency, robustness to interference, resistance to fading, sub-carrier rate adaptation, simple receiver, low cost transmitter [1]. With these outstanding capabilities, OFDM system has been adopted by several communication technologies like digital audio broadcast, digital video broadcast [2], asymmetric digital subscriber line services, IEEE 802.16a, IEEE 802.11a/g and it also becomes a promising candidate for the next-generation technologies in digital communication systems such as wireless local area networks (WLAN) [3], WiMAX, LTE/LTE-A, etc. to support high-speed wide band digital transmission and reception. Nevertheless, OFDM systems stricken high peak-to-average ratio (PAPR) which can induce signal distortions, reduction in efficiency of RF amplifier, complexity in digital-to-analog and analog-to-digital converters, thus reduction of PAPR has become a research hotspot in the field of digital communications [4-16].

In order to reduce the PAPR in OFDM systems, various methods such as; clipping technique [5], coding technique [6], pre-distortion technique [7], transform schemes [8], and probabilistic scrambling techniques [9-16], are found in the literature. The probabilistic scrambling techniques are based on scrambling of the input data and transmission of data sequence with lowest PAPR. Tone reservation, selective mapping, tone injection, and partial transmit sequence (PTS) techniques are the examples of probabilistic scrambling techniques. Among all the PAPR reduction techniques, PTS is the most promising distortionless technique and has been successfully used in numerous digital communication applications [9-11].

In PTS technique; firstly, the input data is partitioned into several closely spaced sub-blocks and sub-blocks are separately multiplied by a set of phase weighting factors to form multiple sequence, then the one with lowest PAPR is selected for the transmission. However, the search of all possible phase factors to find optimum phase factor set which produces lowest PAPR is an exhaustive search task. The complexity of search task enlarges exponentially with the increase in number of sub-blocks

* Corresponding author. Tel.: +90-342-3171789; Fax: +90-342-3601171.
E-mail addresses: tokur@gantep.edu.tr *(Y. Tokur Bozkurt)*, taspinar@erciyes.edu.tr *(N. Taşpınar)*
ORCID: 0000-0003-3195-132X *(Y. Tokur Bozkurt)*, 0000-0003-4689-4487 *(N. Taşpınar)*
DOI: 10.35860/iarej.405068

and eliminates the feasibility in practical implementations of high-speed data transmissions [11-16].

In recent years, suboptimal search strategies are applied to alleviate complexity of optimal phase factor search tasks. Some studies proposed the combination of PTS technique with certain suboptimal search strategies such as random search (RS) [11], cuckoo search (CS) [12], differential evolution (DE) [13], parallel tabu search [14], artificial bee colony [15], harmony search (HS) [16], and particle swarm optimization (PSO) [17]. Swarm intelligence is noted as a strong method appropriate for optimization problems. For example, as a stochastic global optimization technique Particle swarm optimization is based on social behavior of bird flocking or fish schooling. Bat algorithm has been inspired by bats behavior during their hunting and flight [18]. In the PSO, each particle in the swarm arranges its position in the search space based on the best position it has realized so far as well as the position of the familiar best-fit particle of the whole swarm. Finally approaches to the global best point of the entire search space. The bat algorithm is inspired from the echolocation behavior of microbats, with varying pulse rates of loudness and emission [19-20].

In this paper, a PTS technique combined with suboptimal bat algorithm is proposed to reduce to PAPR with a low computational load. Modified PTS combining the interleaved partitioning for reducing the PAPR of OFDM signals with QAM sub-blocks is proposed. In Section 2 the theoretical description of OFDM system is introduced. In Section 3 and 4 traditional PTS and the bat search optimization algorithm (BA) for PAPR reduction are explained, respectively. Simulation results of the proposed technique are presented in Section 5 and finally, Section 6 concludes the work.

2. System Model of OFDM

Suppose in an OFDM system $X = [X_0, X_1, \cdots, X_{N-1}]$ indicates an input data sequence modulated by 16 quadrature amplitude modulation (QAM), where N shows the number of sub-carriers. Hense, in the discrete time domain an OFDM signal $x = [x_0, x_1, \cdots, x_{N-1}]$ can be described by

$$x_n = \frac{1}{\sqrt{N}} \sum_{k=0}^{N-1} X_k e^{\frac{j2\pi kn}{N}}, \quad 0 \le n \le N-1 \qquad (1)$$

where n is the discrete time index.

In the discrete time domain based on signal power the PAPR of OFDM signal can be represented by the ratio of the peak power to the average power, which can be showed by

$$PAPR(x_n) = 10log_{10} \frac{\max\limits_{0 \le n \le N-1} \{|x_n|^2\}}{E\{|x_n|^2\}} dB \qquad (2)$$

where E $\{\cdot\}$ and max $\{\cdot\}$ represent the expectation operation and the maximum operation, respectively.

Complementary cumulative distribution function (CCDF), which is also used to compare and evaluate PAPR reduction schemes' performances, is be described by

$$CCDF(N, PAPR_0) = Pr\{PAPR > PAPR_0\} = 1 - (1 - e^{-PAPR_0})^N \qquad (3)$$

where $PAPR_0$ shows a dedicated value of PAPR.

The PAPR characteristics of discrete-time OFDM signals and continuous-time OFDM signals are pretty much similar to each other. The proper PAPR performance can be accomplished through the implementation of LN-point IFFT of symbol sequence with (L-1)N zero-padding [9-16]. In the discrete time domain, the oversampling factor, L, is generally acknowledged as 4.

3. Traditional PTS

The functional block diagram of a distinctive partial transmit sequence combined bat algorithm optimization is shown in Figure 2. Proliferation of sub-blocks with optimized phase rotation vectors is the basic principle behind the PTS scheme as a distortionless PAPR reduction algorithm. In a representative PTS scheme, the input signal X is sectioned into M disjoint sub-blocks each with a set of sub-carriers equal size N, such that

$$X = \sum_{m=1}^{M} X_m \qquad (4)$$

where X_m shows the mth sub-block sequence. Each sub-block is weighted with an assigned phase weighting factor. The resulting sub-blocks are combined to diminish PAPR after being multiplied by phase rotation vectors. There wards, with the application of IFFT, the applicant sequence x′ can be maintained given by

$$x' = \sum_{m=1}^{M} b_m . IFFT\{X_m\} = \sum_{m=1}^{M} b_m \, x_m \qquad (5)$$

Where x_m represents the m[th] sub-block sequence in the time domain and b_m is the phase factor for m[th] sub-block sequence. Finally, the one with the lowest PAPR between all the applicant sequences is picked for transmitted.

The side information is necessary to successfully acquire original data sequence at the receiver. Theorize there are W allowed phase weighting factors in conventional PTS. Hence, M shows the number of sub-block, we can obtain W^{M-1} applicant sequences. Thus, $log_2 W^{M-1}$ bits are required to express the side information.

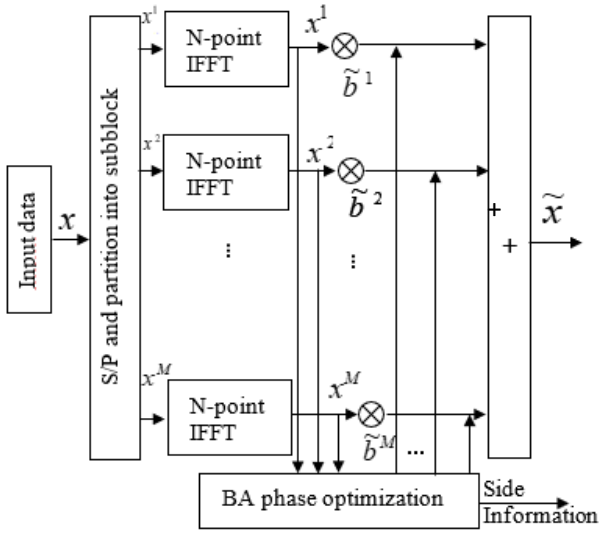

Figure 1. System model of the BA-PTS model

4. Bat Search Optimization Algorithm

Bat algorithm (BA), suggested by Xin-She Yang [19] in 2010, is a nature-inspired stochastic search algorithm for both non-linear and linear global optimization problems. It mimics the echo-location characteristics of microbats with varying pulse rates of loudness and emission. The flow chart of a bat algorithm is given in Figure 2.

The bat algorithm is built on the following basic assumptions: all bats utilize echolocation to locate orientation of target and detect distance, fly from their own position x_i to other randomly using velocity v_i, emit pulse using a constant frequency f_{min} with loudness A_0 and varying wavelength λ to detect forage, can also set the wavelength (or frequency) and the rate ($r \in [0,1]$) of emitted pulses with respect to proximity of target, and the loudness of emitted pulses alter from a large A_0 to a minimum constant value A_{min}.

In a d-dimensional search space there are some simple rules to update locations x_i and velocities v_i of bats during the search. At a time, instance t, a set of new positions x_i^t and velocities v_i^t can be given as

$$f_i = f_{min} + (f_{max} - f_{min})\beta \quad (6)$$

$$v_i^t = v_i^{t-1} + (x_i^t - x_*)f_i \quad (7)$$

$$x_i^t = x_i^{t-1} + v_i^t \quad (8)$$

where x* and β are the current global best location and random vector drawn from uniform distribution variable, respectively. The value of β must be between 0 and 1.

5. Simulations

The OFDM signals having $M = 16$ sub-blocks with 16-QAM modulation were randomly generated for computer simulations. Different number of the generation/the iteration G, different number of the population/the particle P, number of the phase factor $W = 2$, the number of sub-carries $N = 256$, pulse rate $R = 0.5$ and loudness $A = 0.5$ were selected. The fundamental parameters of the simulations were listed in Table 1.

Figure 3 and Figure 4 show the CCDF versus PAPR plot of the proposed scheme with the variation of number of population and number of iteration, respectively. The examined values are $10, 25,$ and 75 for the number of population, $25, 50,$ and 75 for the number of iteration while $P = 10$ and $P = 50$.

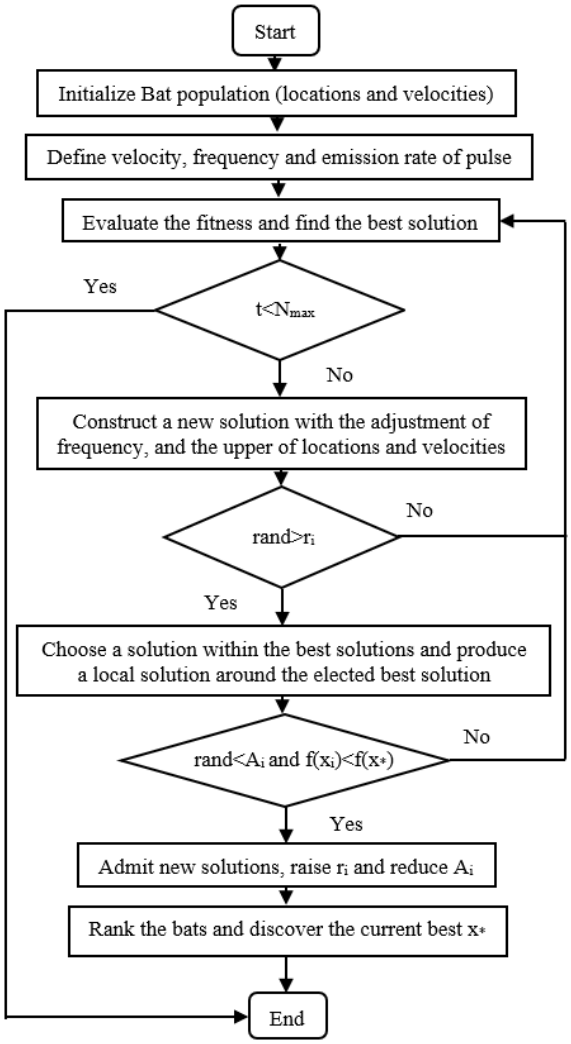

Figure 2. The flowchart of bat algorithm

Table 1. The fundamental parameters of the simulations

Quantity	Symbol	Value
number of sub-blocks	M	16
number of phase factor	W	2 (±1)
number of the iteration	G	25,50,75
number of sub-carriers	N	256
number of the population	P	10,25,50
loudness	A	0.5
pulse rate	R	0.5
modulation method	QAM	

The CCDF versus PAPR plot for the proposed scheme with 256 subcarriers is shown in Figure 3. It is clearly seen that PAPR is significantly reduced as the numbers of population increases. The PAPR values at $CCDF = 10^{-3}$, are 7.4 dB, 6.82 dB, 6.51 dB and 6.42 dB for 10, 25, 50 and 75 number of population, respectively. Compared to the traditional PTS, the PAPR reduction of about 3.55 dB for 10 population 4.13 dB for 25 population, 4.44 dB for 50 population and 4.53 dB for 75 population were achieved.

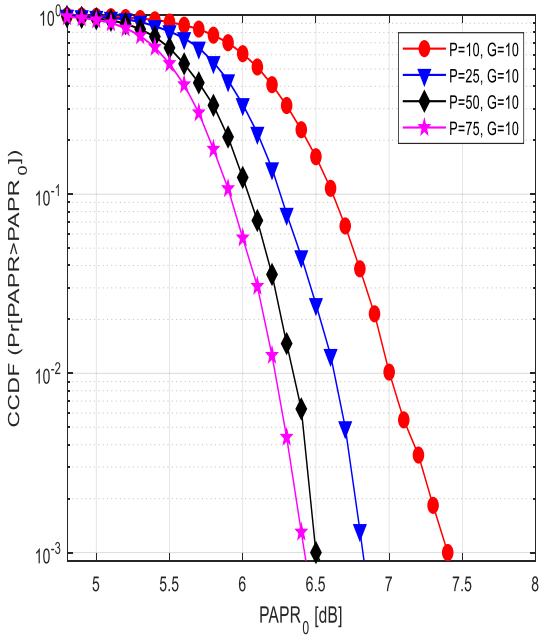

Figure 3. The CCDF versus $PAPR_0$ (dB) of BA-PTS with different values of P for G=10

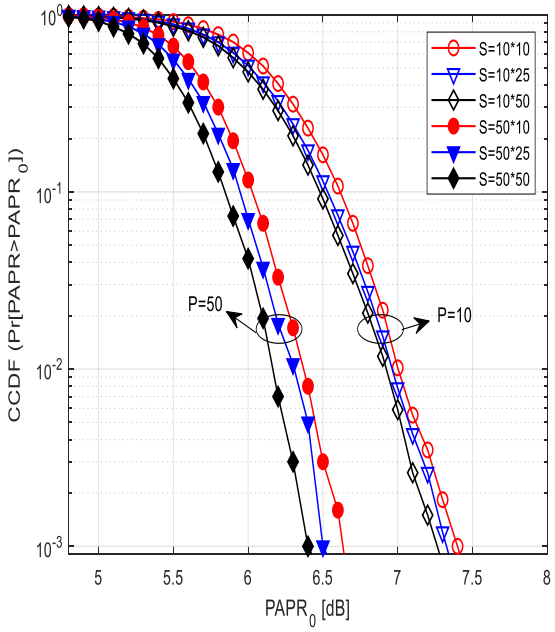

Figure 4. The CCDF versus PAPR0 (dB) of BA-PTS with different numbers of iteration for P=10 and P=50

In Figure 4, the simulation results are shown for the proposed scheme in which 10 and 50 numbers of population are employed with various iterations. The iterations are chosen as 10, 25 and 50. The number of sub-blocks and the number of sub-carriers are used as $M = 16$ and $N = 256$, respectively. It is observed that an increase in the number of iterations is resulted with a serious reduction in PAPR. When $P = 10$, the PAPR values are 7.42dB, 7.3 dB, and 7.28 dB at same time when $P = 50$, the PAPR values are 6.62 dB, 6.5 dB, and 6.42 dB for 10, 25 and 50 iterations, respectively. The PAPR reductions for $P = 50$, in accordance with for the PAPR reductions $P = 10$, are approximately 0.8 dB for 10 iteration, 0.8 dB for 25 iteration, 0.86 dB for 50 iteration.

Table 2 shows comparison of computational complexity amongst different methods for $M = 16$, $N = 256$ and $W = 2$.

In Figure 5, the performance comparison of the proposed scheme with other PTS based PAPR reduction schemes (optimum, random search, differential evolution and cuckoo search) are presented. When CCDF=10^{-3}, the PAPR of the original is 10.95 dB, the random search (RS) is 7.2 dB, the PAPR values for and the suboptimal methods are 7.1 dB for the cuckoo search (CS), 6.75 dB for the differential evolution (DE), 6.37 dB for the Optimum-PTS (O-PTS) and 6.54 dB for the proposed system. For same search complexity, the PAPR of the BA-PTS is smaller 0.21 dB, 0.56 dB, 0.66 dB than that of DE-PTS, CS-PTS and RS-PTS, respectively. The comparison shows that the BA-PTS gives better PAPR reduction compared with RS-PTS, CS-PTS and DE-PTS in OFDM system.

In Figure 6, the performance comparison of the proposed scheme with other PTS based PAPR reduction schemes such as harmony search, particle swarm optimization and optimum are presented. When $CCDF = 10^{-3}$, the PAPR of the original is 10.95 dB, the PAPR values for and the suboptimal methods are 7.45 dB for the PSO-PTS, 7.27dB for the HS-PTS, and 6.54 dB for the proposed system. For same search complexity, the PAPR of the BA-PTS is smaller 0.91 dB, 0.73 dB, than that of PSO-PTS and HS-PTS, respectively.

Table 2. Computational Complexity of the PTS Methods

Method	Search	PAPR
Original	0	10.95
PSO-PTS	1000	7.45
HS-PTS	1000	7.27
RS-PTS	1000	7.2
CS-PTS	1000	7.1
DE-PTS	1000	6.75
BA-PTS	1000	6.54
O-PTS	32768	6.37

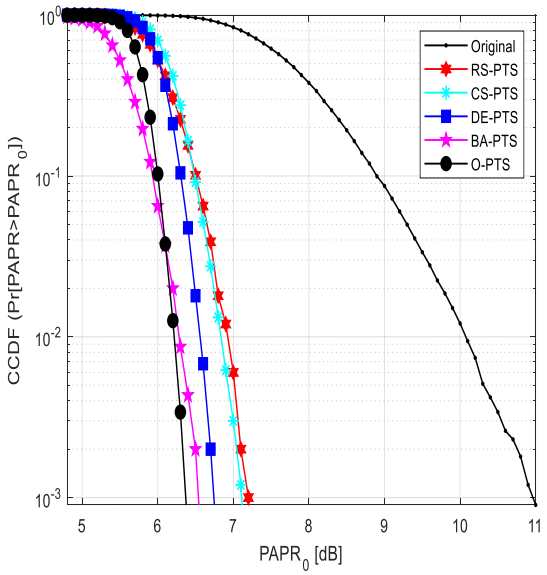

Figure 5. The CCDF versus $PAPR_0$ (dB) of optimum PTS, BA-PTS, DE-PTS, CS-PTS, RS-PTS and the original

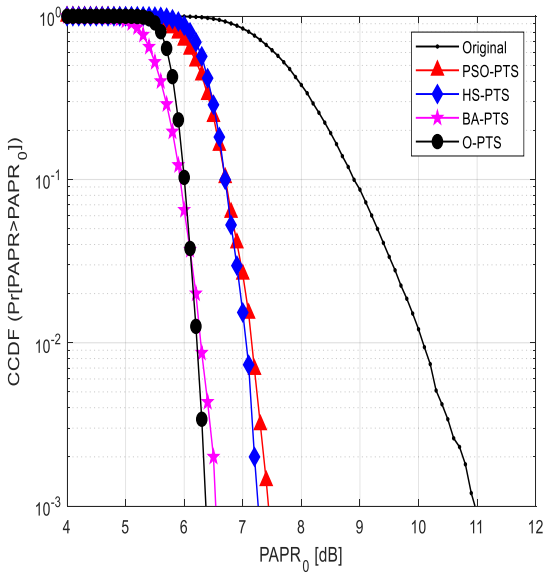

Figure 6. CCDF versus $PAPR_0$ (dB) comparison of optimum PTS, BA-PTS, HS-PTS, PSO-PTS and the original

The comparison shows that the BA-PTS gives better PAPR reduction compared with HS-PTS and PSO-PTS in OFDM system.

6. Conclusion

In this paper, we present PTS based on bat algorithm in OFDM system to deal with the PAPR problem to reduce the complexity. The CCDF simulations are performed to evaluate the PAPR reduction performance of the proposed BA-PTS scheme. The PAPR reduction performance and computational load are compared with those of original PTS, Optimum-PTS, RS-PTS, CS-PTS, DE-PTS, PSO-PTS and HS-PTS. It is shown that compared to RS-PTS, CS-PTS, DE-PTS, HS-PTS and PSO-PTS, BA-PTS scheme provides better PAPR reduction performance with less computational load.

References

1. Yang, S., Yang, W., Cai, Y., and Wei L., *An energy efficient PTS scheme for PAPR reduction in OFDM relay systems.* in *ChinaCom*2015: Shanghai, China. p.858-863.
2. Patidar, M.K., Mishra, A., and Saxena, R., *Partial approximate gradient constellation for PAPR reduction in OFDM signals.* International Journal of systems, Control and Communications, 2016. **7**(1): p.83-96.
3. Joshi, A., and Saini, D.S., *Peak-to-average power ratio reduction of OFDM signals using improved PTS scheme with low computational complexity.* WSEAS Transactions on Communications, 2013. **12**(12): p. 630-640.
4. Huang, X., *Diversity performance of precoded OFDM with MMSE equalization.* in ISCIT'07: Sydney, Australia. p.802-807.
5. Wang, J., Guo, Y., and Zhou, X., *PTS-clipping method to reduce the PAPR in ROF-OFDM system.* IEEE Transactions Consumer Electronics, 2009. **55**(2): p. 356-359.
6. Jones, A.E., Wilkinson, T.A., and Barton, S.K., *Block coding scheme for reduction of peak to mean envelope power ratio of multicarrier transmission scheme.* Electron Lett, 1994. **30**(25): p. 2098–2099.
7. Sharma, C., Tomar, S.K., and Gupta, A.K., *PAPR reduction in OFDM system using adaptive coding technique with pre distortion method.* WSEAS Transactions Communications, 2011. **10**(9): p. 255-262.
8. Huang, X., Lu, J., Zheng, J., and Letaief, K.B., *Companding transform for reduction in peak-to-average power ratio of OFDM signals.* IEEE Transactions on Wireless Communications, 2004, 3(6): p. 2030-2039.
9. Jie, Y., Lei, C., Quan, L., and De, C., *A modified selected mapping technique to reduce the peak-to-average power ratio of OFDM signal.* IEEE Transactions Consum Electr, 2007. **53**(3): p. 846-851.
10. Chen, J.C., and Li, C.P., *Tone reservation using near-optimal peak reduction tone set selection algorithm for PAPR reduction in OFDM systems.* IEEE Signal Processing Letters, 2010. **17**(11): p. 933-936.
11. Cimini, L.J., and Sollenberger, N.R., *Peak-to-average power ratio reduction of an OFDM signal using partial transmits sequences. IEEE Commun Lett, 2000.* **4**(3): p. 86-88.
12. Tokur Bozkurt, Y., and Taspinar, N., *PAPR reduction in OFDM systems using partial transmit sequence with Cuckoo search optimization algorithm.* International Journal of Intelligent Systems and Applications in Engineering, 2016. **4**(1): p. 260-263, 2016.
13. Hung, H.L., and Huang, Y.F., *Peak-to-average power ratio reduction in orthogonal frequency division multiplexing system using differential evolution-based partial transmit sequences scheme.* Commun IET, 2012. **6**(11): p. 1483-1488.
14. Taspinar, N., Kalinli, A., and Yildirim, M., *Partial transmit sequences for PAPR reduction using parallel tabu search algorithm in OFDM systems.* IEEE Commun Lett, 2011. **15**(9): p. 974-976.
15. Taspinar, N., Karaboga, D., Yildirim, M., and Akay, B.,

PAPR reduction using artificial bee colony algorithm in OFDM systems. Turk J Elec Eng & Comp Sci, 2011. **19**(1): p. 47-58.

16. Kermani, E.M., Salehinejad, H., and Talebi, S., *PAPR reduction of OFDM signals using harmony search algorithm*, in *ICT*2011: Ayia Napa, Cyprus. p. 90-94.
17. Gao, J., Wang, J., and Wang, B., *Improved particle swarm optimization for PAPR reduction of OFDM systems.* International Conference on Networking, Sensing and Control, in *ICNSC*2010: Chicago, IL, USA. p.621-624.
18. Chaieb, H., and Sakly, A., *Review and comparison BAT and PSO MPPT's based algorithms for photovoltaic system.* WSEAS Trans on Power Systems, 2018. **13**: p.108-117.
19. Yang, X.S., *A new metaheuristic bat-inspired algorithm-Inspired Algorithm, Nature Inspired Cooperative Strategies for Optimization*, Springer, 2010. **284**: p. 65-74.
20. Mishra, S., Shaw, K., and Mishra D., *A new meta-heuristic bat inspired classification approach for microarray data.* Procedia Technology, 2012. **4**: p. 802-806.

Available online at www.dergipark.gov.tr

INTERNATIONAL ADVANCED RESEARCHES
and
ENGINEERING JOURNAL

Journal homepage: www.dergipark.gov.tr/iarej

e-ISSN: 2618-575X

International
Open Access

Volume 03
Issue 03

December, 2019

Research Article

Misalignment fault detection by wavelet analysis of vibration signals

Özgür Yılmaz [a,*], ***Murat Aksoy*** [a] ***and Zehan Kesilmiş*** [b]

[a]*Department of Electrical and Electronics Engineering, Çukurova University, Balcali Adana, 01380, Turkey*
[b]*Department of Electrical and Electronics Engineering, Adana Bilim ve Technology University Saricam Adana, 01380, Turkey*

ARTICLE INFO

Article history:
Received 07 August 2018
Revised 13 September 2019
Accepted 10 October 2019

Keywords:
Asynchronous motors
Misalignment fault
Vibration frequency spectrum

ABSTRACT

Asynchronous motors are frequently used in many industrial applications, especially pumps and fans. Placement, bearing and coupling faults are common faults in these types of engines. Misalignment error is a common type of error that is seen very often among these errors. This error may cause efficiency decrease in a short run and vibration may cause short circuit and wear in moving parts in the stator windings in a long run. Early diagnosis of such faults is important in terms of machine health and productivity. In this study, loose connection and angular imbalance of the asynchronous machine were investigated. In the experimental works, a 1 Phase 0.75 KW power asynchronous motor, Y-0036-024A Electromagnetic Brake and SKF Microlog vibration meter were used during the measurements. The Frequency components of motor caused by the settlement errors were investigated under the different loads. A loose assembly error and angular imbalance were investigated from the misalignment errors. The engine was run idle and without any positioning errors and measurements were taken from different points with the accelerometer and the frequency spectrum examined. Measurements are repeated when the misalignment errors are occurred on purpose and the FFT frequency components were compared under the load of 12.50Nm using magnetic brake. The results show that the FFT frequency components are examined and the placement error can be determined with high success and accuracy. It has been found that harmonic components are formed in the frequency spectrum at 25Hz Coefficients. After the settlement error is generated it is seen that, undesired frequency components that are unloaded are lowered under load when the frequency spectra is examined. In this study, theoretical and experimental comparisons of settlement errors are made. Although many errors in this subject are examined in the same publication in general, only the results of the settlement errors are examined specifically as a contribution to the literature. The results and graphs are presented comparatively to the reader's knowledge.

1. Introduction

Asynchronous machines are frequently confronted in the industrial world. Today, the engine is the starting point of mechanical movement in many production processes. Today all industrial plants are exposed to asynchronous motors or a derivative or variant. In routine operations, each component generates a mechanical vibration signal at a given frequency even if the machines are operated under normal conditions. The amplitude and frequency of this signal are also related to the component's own material and design parameters, depending on the rotor rotation speed. Changes occur in component frequency characteristics when the motor is not under normal operating conditions or when an error occurs in the components [1,2]. Since vibration values from the outside of the motor are seen as the sum of the amplitudes at each frequency, it is very difficult to read under normal conditions [3]. Therefore, by dividing the components of the total signal into frequency components, reading the frequency information of the component operating outside normal conditions in the frequency spectrum will provide a faster and easier way to diagnose faults [4]. It is expected that the signal generated in normal conditions will have a vibration frequency and amplitude, the amplitude of the same vibration signal will increase in case of unbalance, sidebands will occur in the case of Settlement Errors, harmonics will be formed with general expression in case of loose connection and bearing errors [5].

The aim of this study is to investigate the frequency response of placement errors of motors. The total frequency is divided into its components by fourier

* Corresponding author. Tel.: +90-322-455 00 40 / 2401.
E-mail addresses: ozguryil@gmail.com *(Ö. Yılmaz)*, aksoy@cu.edu.tr *(M. Aksoy)*, zkesilmis@adanabtu.edu.tr *(Z. Kesilmiş)*
ORCID: 0000-0003-0972-0226 *(Ö. Yılmaz)*, 0000-0002-6980-5902 *(M. Aksoy)*, 0000-0002-5781-9450 *(Z. Kesilmiş)*
DOI: 10.35860/iarej.451528

transform and the changing frequency component is investigated by the placement error. When this error persists, a torque of 12.5Nm is added as a load on the motor and the same components are examined under load. In the experimental works, an asynchronous motor, Y-0036-024A Magnetic Powder Brake and SKF Microlog CMXA 80 vibration measurement and analysis device were used in 1 Phase 0.75KW power. All researchers worked in the laboratory during experimental studies.

Step 1: Vibration values have been obtained by operating the engine without a load.

Step 2: An angular error was given to the motor and measurements were made in the unloaded position.

Step 3: Measurements were made with a 3° angular placement error.

Many publications in literature, anomalies in vibration signal characteristics have been detected by wavelet analysis. Bearing failures, shaft imbalances and coupling failures have been studied. Bayrak et al. developed a power-based algorithm for the detection of broken rotor rod and concluded that by analyzing the changes in the energy densities of the components in the 90-110 Hz frequency range, the rotor fractures occurring on the motor consisted of components twice the network frequency [1]. Ayaz, E. studied an AI system to detect bearing faults with wavelet analysis.In this study the relationship between motor vibration and current signals was used as training set of an auto-associative recurrent neural network and with this way bearing failure frequencies was determined [6]. Carbajal-Hernández et al. studied the orbital analysis to detect rotor unbalance error to propose a new computational model. In this model it is suggested that vibration signals are processed with suggested computational model to obtain characteristic patterns created by orbits. These patterns are evaluated as inputs to a AI neural network [2]. Chen et al. studied Rotationg Machinery Fault Diagnosis(RMFD). Wavelet Analysis was used as the method. The study mainly covers the use of wavelet analysis on RMFD. They also mentioned the advantages/disadvantages of wavelet analysis in different applications and finally made a study for the detection of bearing faults [7].

Although most of the engine failure types and wavelet method have been studied no publication was found to detect misalignment faults by wavelet analysis. The focus of this study is the misalignment faults. The method used in this study is wavelet analysis of vibration signals. With this aspect, the study is thought to contribute to a gap in the literature.

2. Motor Frequency Components

2.1 Fourier Transform

The Fourier transform (FT) is a transformation that allows multiple signals to be expressed as a single total signal and each of these components can be expressed separately in frequency and amplitude separately from the total signal. Because time information is not carried by the Fourier Transformation, it does not give information about the time of the frequency, but it is used in signals that do not show time dependent changes [8,9].

Fourier Transform can be divided into Continuous Time Fourier Transform (CTFT) and Discrete-Time Fourier Transform (DTFT).

Continuous Time Fourier Transform can be expressed as;

$$F(k) = \frac{1}{\sqrt{2\pi}} \int_{-\infty}^{\infty} f(x) e^{-ikx}\, dx \tag{1}$$

$$f(x) = \frac{1}{\sqrt{2\pi}} \int_{-\infty}^{\infty} F(k) e^{ikx} dk \tag{2}$$

$$X(e^{jw}) = \int_{-\infty}^{\infty} X_c\,(t) e^{-jwt} dt \tag{3}$$

And Discrete-Time Fourier Transform is expressed as;

$$X(e^{j\Omega}) = \sum_{n=-\infty}^{\infty} x[n] e^{-j\Omega} \tag{4}$$

The discrete-time Fourier transform gives complex exponential signal components at different frequencies of a discrete-time signal. Discrete-time is periodic with 2π period due to the properties of complex exponential signs [8,10].

$$X(e^{j\Omega}) = \; \rangle \; x[n] e^{-j\Omega \mathrm{n}} \tag{5}$$

Inverse discrete-time Fourier transformation expression;

$$x[n] = \frac{1}{2\pi} \int_{-\pi}^{\pi} X(e^{j\Omega})\, e^{j\Omega}\, d\Omega \tag{6}$$

The Fourier spectrum of a signal is as follows, with amplitude and phase components;

$$X(e^{j\Omega}) = \left| X\,(e^{j\Omega}) \right| e^{j \angle X\,(e^{j\Omega})} \tag{7}$$

The amplitude of the Fourier transform $|X(e^{j\Omega})|$ points out amplitude spectrum and the amplitude spectrum is called the phase $\angle X(e^{j\Omega})$ phase spectrum.

Absolute summability is sufficient to enable fourier transformations of the signals, but Fourier Transform can also be performed when it is not aggregable. In the Fourier transforms, the convergence of the sign transformations in the infinite period is important, so Fourier Transform can also be performed for non-aggregate functions. The amplitude spectrum of the discrete-time $x\,[n]$ sign is a dual function, and the phase spectrum is a single function. The amplitude spectrum is symmetrical because the $x\,[n]$ sign is examined in the range (-π, π). The phase spectrum is reversed-symmetrically. For this reason, it is sufficient to examine the frequency spectrum (0, π). This is due to the symmetrical property of Discrete-Time Fourier Transform.

2.2 Frequency Components

Each piece on a running motor creates a vibration. Components such as windings, fans, bearings in the motor

create a component in the frequency spectrum [11]. It is expected that there will be a frequency spectrum like the one in Figure 1 for a motor that works in ideal conditions.

However, other components affecting the frequency components also have different effects on this component. The frequencies of these components are shown in Figure 2 [5,8].

When these components are picked up by the sensor, it looks like Figure 3 in the amplitude-frequency domain.

2.3 Frequency Spectrum Error Components

Each component reflects its frequency on the vibration signal. Therefore, each component generates error signals with different characteristics on the frequency component that it has formed [12-13].

Table 1 shows which faults are caused by faults in these components.

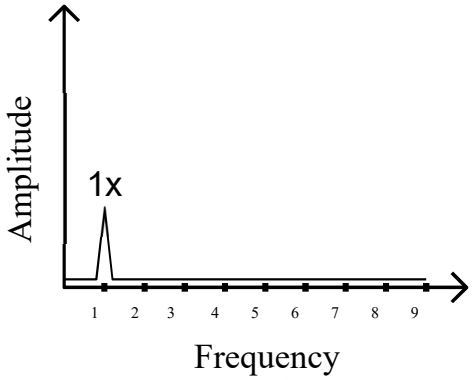

Figure 1. Motor ideal operation frequency spectrum

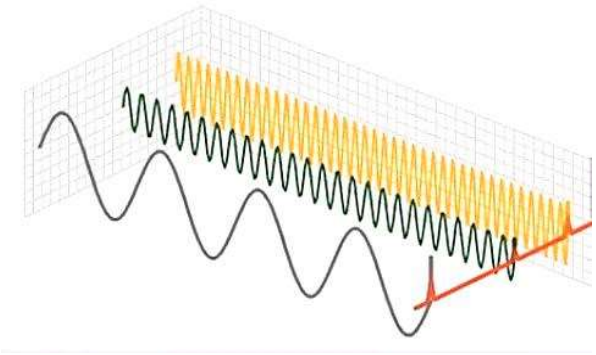

Figure 2. Frequency components

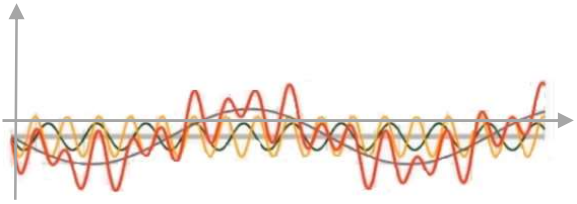

Figure 3. Amplitude-time graph of total vibration signal

Table 1. Error types [3]

Reason for Failure	Parameter Affected by Fault				
	Temperature	Pressure	Leakage	Oil	Vibration
Imbalance					√
Axis Obstruction	√				√
Bearing Load	√				√
Bearing Bed	√	√	√	√	√
Thead Damage				√	√
Looseness					√

Table 1 shows, vibration occurs in all types of error. Figure 1 gives the frequency spectrum expected to occur under ideal conditions. The frequency spectra that occur when errors occur are examined below.

2.3.1 **Imbalance**

The equilibrium (balance) of all the forces generated by the rotating elements in the machine is called the balance. Any change in this equilibrium causes unbalance. Imbalance is one of the most common types of error that are the most common cause of vibration in machines. Theoretically, no vibrations occur in a perfectly balanced machine. In practice there is no perfectly balanced machine. All machines are unbalanced, even at low levels. This imbalance forms a peak at the vibration frequency (1x) of the shaft rotation speed in the spectrum graph [14]. The components of the erroneous frequency spectrum expected to come into play in the case of imbalance are as shown in Figure 4.

In this graph, the growth of the component in the frequency spectrum in the normal operating mode is expected. The growth affects on the nominal rotation frequency, since the rotor will form once per revolution, due to the static imbalance on the rotor shaft.

2.3.2 Looseness

The working machine parts have loose connections over time. Generally, in the vibration spectrum graph, the vibration generated by the spindle revolution consists of multiple harmonics (1x, 2x, 3x, ...). In some cases, the shaft is also at half harmonics (0.5x, 1.5x, 2.5x, ...) of the revolution [12,14-15].

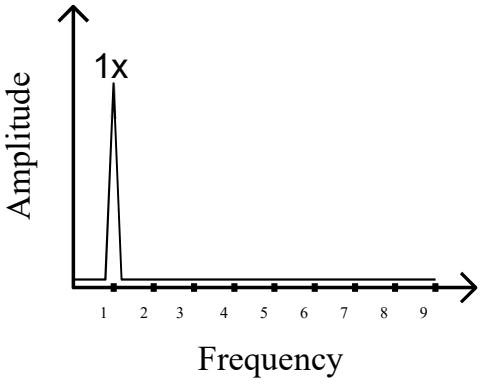

Figure 4. Imbalance frequency spectrum

In the case of a slack error, it is expected that the frequency spectrum of each component will be different in the frequency spectrum, so Figure 5.

Looseness of engine failure as the loose shaft and bearing looseness in the assembly error in the basic work done on the ground should be examined separately [15,16].

2.3.3 Bearing Fault

Roller bearings are widely used in rotating machinery. The problem-free operation of the machines is directly related to the healthy operation of the bearings. Vibration can be measured from the machine bearings and information can be obtained about the developments in the internal structure of the machine [16-17].

There are four types of failure frequencies that characterize the failure in the occurrence of a failure in the bearing. These are the outer ring, the inner ring, the rolling element and the lattice frequency [6,18].

The frequency components for the bearing failures are calculated by the following formula.

$$f_{du} = \frac{n}{2} f_r [\, 1 - \frac{BD}{PD} \cos\beta \,] \qquad (8)$$

Here;

n = Number of Balls

PD= $(D_1+D_2) / 2$

D_1= Ball Outside Radius

D_2= Ball Inner Radius

BD = Ball Radius

f_r = Cycle Frequency

β = Contact Angle.

It is expected that BPF harmonic components will occur in bearing problems. This is the harmonics that vary depending on the inner and outer diameters of the bearing. The graphical characteristic of the U is expected to occur as shown in Figure 6 [6,19].

2.3.4 Misalignment

Placement mistakes are very common in engine failures. 50% of the failures on systems containing asynchronous motors constitute placement errors.

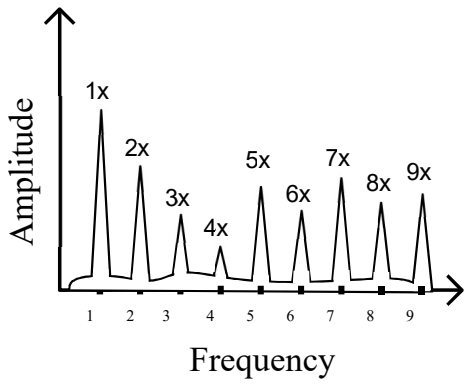

Figure 5. Frequency Spectrum of Looseness Error

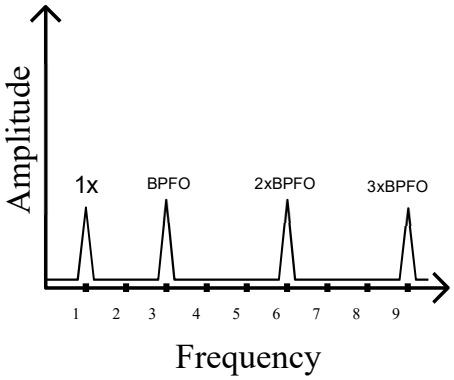

Figure 6. Bearing Failure Frequency Spectrum

Placement mistakes can be examined in two main sections.

- Axial Misalignment,
- Actual Misconception

Axial Distortion It occurs when the spindle, coupling or bearings are not adjusted from their exact centers [6,20]. The cases like Figure 7 are examples of axial misalignment.

All three types of misalignment cause a significant imbalance in the machine, which causes a vibration in the spectrum graph that causes a peak at 1x frequency. Internal (bearing) and parallel misalignment cause a high peak at 2x harmonic frequency at the same time.

Inner misalignment is a type of error related to the shaft. Parallel misalignment error experimental setup Figure 8 and the drawings of the experimental setup with angular misalignment error are shown in Figure 10.

The frequency response expected from Figure 8 is shown in Figure 9.

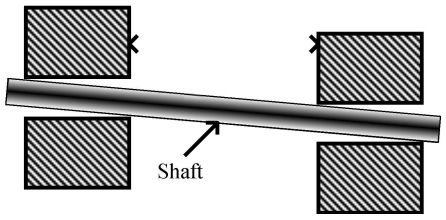

a) Inner Misalignment

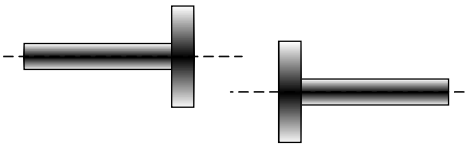

b) Parallel Misalignment

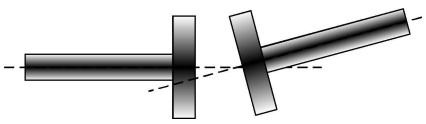

c) Angular Misalignment

Figure 7. Examples of Axis Misalignment

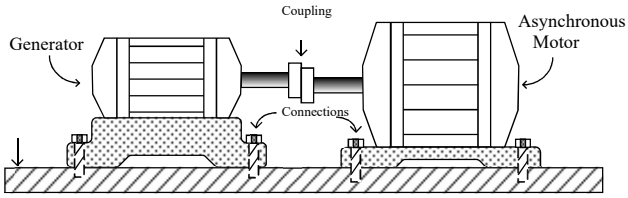

Figure 8. Parallel misalignment error

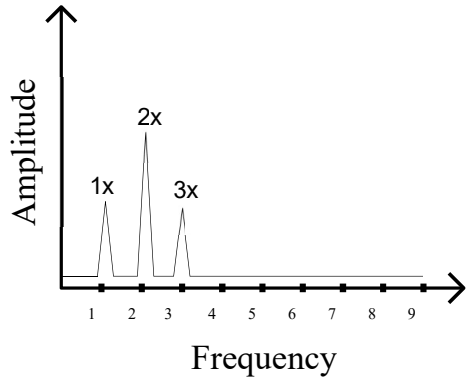

Figure 9. Parallel misalignment error frequency spectrum

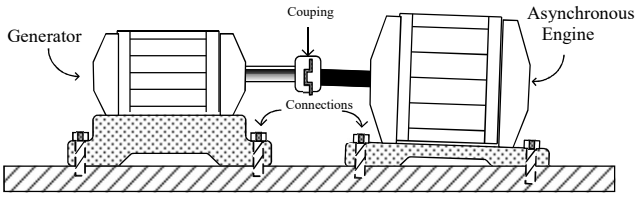

Figure 10. Angular alignment error

Measurements made for angular misalignment are detailed in the measurement results section.

It is expected that the frequency spectrum expected in parallel misalignment mistakes is as shown in Figure 9.

The placement error can also be angular. In this case, it causes an amplitude increase at 1x, 2x harmonic frequencies because it will also cause imbalance on the shaft.

Placement errors and axial misalignments cause a force above the load limit that the bearing can carry. This force on the inner and outer surfaces of the ball bearing and on the ball causes various abrasions and part breaks depending on the time. This causes heating on the ball bearings and therefore on the engine surface. As a result of these warm-ups and wears, motor noise problems and coupling problems due to heat can be seen [6,21].

Another variation of spectrum seen in settlement faults is side band formation.

2.3.4.1 Side Band Formation

The frequency components are two-sided around a central frequency. Despite being bilateral, they are not symmetrical. Carrier occurs depending on frequency. This carrier frequency can be the gear clutch frequency, the ball bearing frequency multiples, the resonance frequency of the machine or the structure, or the resonance frequency carrier frequency of the acceleration metric [16,21].

The sideband may also be referred to as the modulation frequency. It occurs when a frequency f_1 is modulated by f_2. For this reason, it is also known by this name.

3. Measurements and Results

3.1 Experimental Setup

Measurements were made in the laboratory environment. The drawings used for the measurements are given below.

Technical specifications for the engine are shown in the Table 2,

Technical specifications for the vibration analyzer are shown in the Table 3,

Technical specifications for load information are shown in Table 4.

Experimental setup including the motor, brake and coupling connection is shown in Figures 11-14.

3.2 Measurements Results

The measurements are based on the front and rear roller bearings of the motor. First, the values obtained without giving any settlement errors were taken and then the values were obtained by giving axial error and slackness errors.

Table 2. Experimental setup engine specifications

Engine Values	
Rated Voltage	230 V, 50 Hz
Velocity	1500 RPM
I_N	4,6 A
I_A/ I_N	4.5
T_N	5,10 Nm
Cos ϕ	0,98
Code	MSD 80 4b

Table 3. Experimental setup analyzer specifications

Vibration Analyzer	
Brand /Model	SKF CMXA 80 Portable Data collector/ FFT Analyzer
Number of Channel	4
I_N :	4,6 A

Table 4. Experimental setup load specifications

Load Informations	
Brand /Model	Y-0036-024A Magnetic Brake
Cycle	4000 RPM
Voltage	24V DC
Current	1,2A
Torque	20Nm

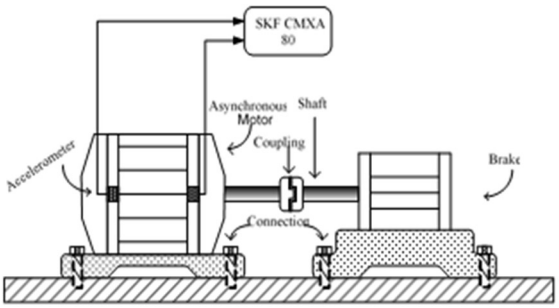

Figure 11. Experimental setup (schematic)

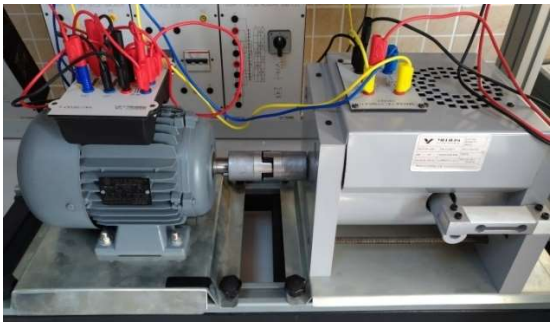

Figure 12. Experimental setup (1st)

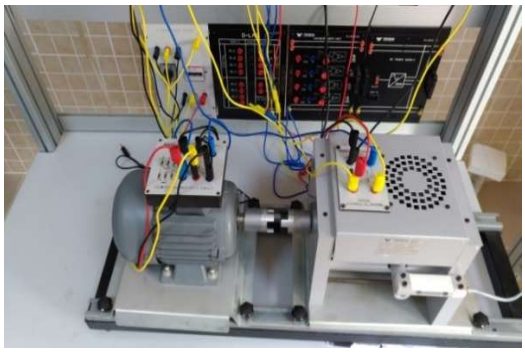

Figure 13. Experimental setup (2nd)

Figure 14. Vibration analyzer (SKF CMXA 80)

The values obtained in the unloaded position of the motor are given in Table 5. Error values in the case of angular imbalance are given in the following tables. The values obtained in the unloaded position by the angular imbalance are given in Table 6. In case of motor 3° angular misalignment fault, measurements were taken under load with torque of 12.5Nm. The values are given in Table 7.

3.3 Frequency Spectrums

The frequency spectra of the values obtained in erroneous and error-free measurements are given below. Natural operation in no-load position When there is 100Hz component in frequency, in case of placement fault, this component increases in amplitude and harmonics are generated at 25Hz frequencies.

The values obtained in the unloaded position of the motor are given in Figure 15. Frequency spectrum when the 3° angular misalignment exists and under load with torque of 12.5Nm is shown in Figure 16.

Table 5. No-load operation Vibration values

Place of Measurement	Date/Time	Last Value	Unit
MFH RUL	17.08.2017 16:03	0,286	gE
MFH HIZ	17.08.2017 16:03	3,62	mm/s
MRH RUL	17.08.2017 16:02	1,329	gE
MRH HIZ	17.08.2017 16:02	2,186	mm/s

Table 6. Unloaded vibration values under angular unbalance

Place of Measurement	Date/Time	Last Value	Unit
MFH RUL	17.08.2017 16:24	0,893	gE
MFH HIZ	17.08.2017 16:24	7,371	mm/s
MRH RUL	17.08.2017 16:23	0,198	gE
MRH HIZ	17.08.2017 16:23	9,986	mm/s

Table 7. Angular imbalance and vibration values under load of 2.5Nm

Place of Measurement	Date/Time	Last Value	Unit
MFH RUL	17.08.2017 16:27	0,708	gE
MFH HIZ	17.08.2017 16:27	4,275	mm/s
MRH RUL	17.08.2017 16:27	0,421	gE
MRH HIZ	17.08.2017 16:26	3,68	mm/s

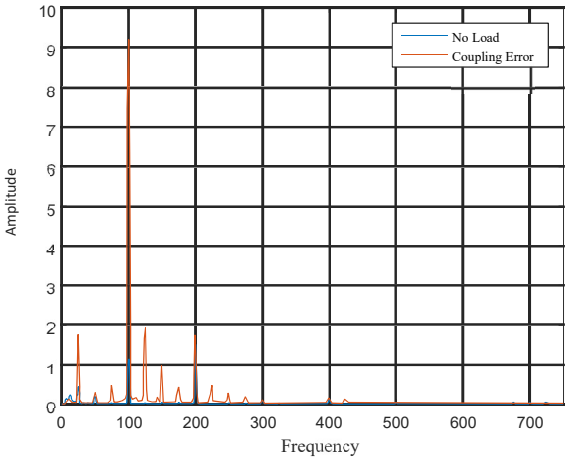

Figure 15. No-Load Operation and 3° Coupling Irregularities Frequency Spectrum

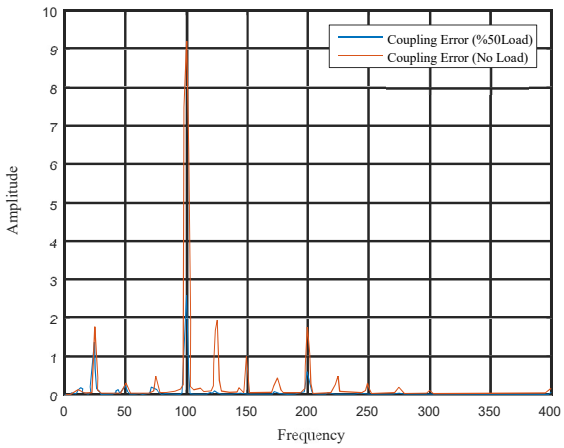

Figure 16: Frequency spectrum at 3° angular imbalance spectrum and under 12.5 Nm load

4. Conclusions

Engine components react to all kinds of abnormal working conditions over time. These reactions may be errors that affect other components in a distributed manner, or a single component connected fault. There is a natural vibration diagram that is generated as a result of the mechanical harmonic motion of each component. As a result of these graphs, the total vibration graph characteristic can be monitored by means of sensors. When this periodic motion is FFT transformed, the frequency component of each motor element can be obtained on the spectrum. These frequency components may vary depending on the rotor frequency and material structure of the mechanical part concerned, depending on external conditions. In case of error, the frequency component reacts like amplitude change, phase shift, harmonic formation, side band formation.

In this study, it was observed that the components of the rotor resonance were found in multiple harmonics such as 1x, 2x in the settlement faults examined (Figure 13) However, side bands are formed. The reason for the formation of these sidebands is that one of the two frequency forming around a center frequency modulates the other frequency.

In this study, the effect of the settlement error on the frequency spectrum has been proved experimentally. Thus, the desired harmonic components are shown graphically to readers.

In the case of angular imbalance in measurement, the value of the amplitude in the unloaded position falls below 12.5Nm under load. This is due to the modulating of the amplitude of the rotor vibration sign of the motor under load. The frequency component is undergoing amplitude modulation unchanged and the amplitude of the vibration signal is reduced.

As a result, it can be said that the settlement error on the motor forms harmonics as an integer number of times and can be observed on the frequency spectrum by sideband formations. The deviation rates in the spectrum have important clues as to the magnitude of the imbalance in settlement error.

Nomenclature

FT	: Fourier Transform
FFT	: Fast Fourier Transform
CTFT	: Continuous Time Fourier Transform
DTFT	: Discrete-Time Fourier Transform
MFH	: Motor Front Half
MRH	: Motor Rear Half
Nm	: Newton.Meter
RPM	: Rate Per Minute

References

1. Bayrak, M., & Küçüker, A.,Üç fazli asenkron motorlardaki kirik rotor çubuğu arizalarinin tespiti için güç tabanli bir algoritmanin geliştirilmesi. *Journal of the Faculty of Engineering and Architecture of Gazi University*, 2014.*29*(3),303–311. https://doi.org/10.17341/gummfd.82945
2. Juan Carbajal-Hernández, J., Sánchez-Fernández, L. P., Hernández-Bautista, I., Medel-Juárez, J. de J., & Sánchez-Pérez, L. A. (2016). *Classification of unbalance and misalignment in induction motors using orbital analysis and associative memories*. *Neurocomputing*, 2016.*175*: p.838–850. https://doi.org/10.1016/j.neucom.2015.06.094
3. Karahan, M. F., *Titreşim analiziyle makinalarda arıza teşhisi.* Yüksek Lisans Tezi, Celal Bayar Üniversitesi Fen Bilimleri Enstitüsü, Manisa,2005:p.37-55.
4. Cerit, M., *Makine Mühendisliği El Kitabı Cilt 1:Üretim veTasarım*,TMMOB,1994(169):p.2-32.
5. Kalyoncu, M., *Titreşim analizi ile makina elemanları arızalarının belirlenmesi*. Mühendis ve Makina Dergisi, Ankara,2006.47(552):p.28-35.
6. Ayaz, E. *Elektrik motorlarında dalgacık analizi yaklaşımı ile rulman arıza tanısı ve yapay zeka tabanlı bir durum izleme sistemi* (Doctoral dissertation, Fen Bilimleri Enstitüsü),2001:p.55-62.
7. Chen, J., Li, Z., Pan, J., Chen, G., Zi, Y., Yuan, J., He, Z., *Wavelet transform based on inner product in fault diagnosis of rotating machinery: A review.* Mechanical Systems and Signal Processing, 2016.70:p.1-35. https://doi.org/10.1016/j.ymssp.2015.08.023
8. Abbak, A., *Jeodezide Zaman Dizilerinin Dalgacık (Wavelet) Analizi*. Doktora Tezi,Selçuk Üniversitesi,Fen Bilimleri Enstitüsü,Konya,2007:p.8-17.
9. Chandra, N. H., & Sekhar, A. S., *Fault detection in rotor bearing systems using time frequency techniques.* Mechanical Systems and Signal Processing, 2016.72(73):p.105–133. https://doi.org/10.1016/j.ymssp.2015.11.013
10. Patil, SS, Gaikwad, JA,*Vibration analysis of electrical rotating machines using FFT: a method of predictive maintenance.* In: 2013 fourth international conference on computing, communications and networking technologies (ICCCNT), Tiruchengode, India, 4–6 July 2013, pp.1–6.
11. Lu, J., Ming, T., & Zhang, C. (2019). *Simulation Research of Rotor Misalignment Fault Based on Adams*. IOP Conference Series: Earth and Environmental Science, 2019.*252(2)*:p.022148. https://doi.org/10.1088/1755-1315/252/2/022148
12. Raj, V. P., Natarajan, K., & Girikumar, T. G. (2013, October). *Induction motor fault detection and diagnosis by vibration analysis using MEMS accelerometer. In Emerging Trends in Communication, Control, Signal Processing & Computing Applications (C2SPCA),* IEEE International Conference,2013(2013):p. 1-6.

13. Thomson, W., *Theory of vibration with applications. CrC Press*,2018:p.17-24.
14. Köse, R. K., *Makine arızalarının belirlenmesinde titreşim analizi.* Mühendis ve Makine Dergisi, 2004(45).538:p:24-32.
15. Cveticanin, L., Vecseri, A., Bíró, I., & Cveticanin, D, *Detection Procedures For Shaft Misalignment detection:An Overview*. Annals of the Faculty of Engineering Hunedoara-International Journal of Engineering,2019.17(1):p.1-4.
16. Ding, H., & Sun, Y.,*Rolling bearing fault feature extraction based on Daubechies wavelet decomposition.* IEEE 37th Chinese Control Conference, 2018:pp.8645-8649.
17. Song, W., Xiang, J., & Zhong, Y. *A simulation model based fault diagnosis method for bearings.* Journal of Intelligent & Fuzzy Systems, 2018.34(6): p.3857-3867.
18. Tezcan, M.,Gökhan, A., Canakoglu, A., Turan, M., *Üç Fazli Asenkron Motor Tasarimi ve FFT Analizi Three Phase Induction Motor Design and FFT Analysis,* [cited 2019 09 July];Available from: http://www.emo.org.tr/ekler/3f79341d72939e6_ek.pdf
19. Wang, J., Zhao, B., & Zhou, H., *Rolling bear fault recognition based on improved sparse decomposition.* IEEE 37th Chinese Control Conference 2018:p. 5790-5794.
20. Hines, A. J. W., Jesse, S., Edmondson, A., & Nower, D., *Motor Shaft Misalignment versus Bearing Load Analysis: Study Shows Shaft Misalignment Reduces Bearing Life*.Maintenance Technology,1999(April):p.11–77.
21. Kumar, C., Krishnan, G., & Sarangi, S., *Experimental investigation on misalignment fault detection in induction motors using current and vibration signature analysis. In Futuristic Trends on Computational Analysis and Knowledge Management (ABLAZE)*, IEEE International Conference,2015:p. 61-66.

Available online at www.dergipark.gov.tr

INTERNATIONAL ADVANCED RESEARCHES
and
ENGINEERING JOURNAL

Journal homepage: www.dergipark.gov.tr/iarej

e-ISSN: 2618-575X

International Open Access

Volume 03
Issue 03

December, 2019

Research Article

On the equivalent ZIP parameter extraction of desktop computer cases and LCD monitors connected in parallel

Şuayb Çağrı Yener [a,*] ***and Reşat Mutlu*** [b]

[a]*Department of Electric and Electronic Engineering, Sakarya University, Sakarya, Turkey*
[b]*Department of Electronics and Telecom. Engineering, Namık Kemal University, Corlu, Tekirdag, Turkey*

ARTICLE INFO

Article history:
Received 03 September 2019
Revised 28 September 2019
Accepted 27 October 2019

Keywords:
Computers
LCD monitors
Least squares method
Load models
Residential appliances
ZIP model

ABSTRACT

Constant-impedance, constant-current and constant-power ZIP models of electrical loads are commonly used in smart grid and residential load applications. Some of residential loads are of nonlinear nature such as LCD monitors and computers. In this study, first, equivalent ZIP model formulas of parallel-connected electrical loads are derived. Then, the ZIP models of an LCD monitor, a computer case and the computer case and the monitor connected in parallel have been obtained using experimental data and least-squares curve fitting method. Finally, the equivalent ZIP model formulas are tested with the experimental data. It has been found that for the rectifier nonlinear loads with different ZIP parameters, the formulas do not give acceptable errors. Therefore, for rectifier nonlinear loads, the measurement-based approach for load modeling must be performed.

1. Introduction

In smart grids power system loads and their modelling is essential from many perspectives; such as, to provide grid reliability by controlling over loads and failures, and to control uncontrollable, untraceable energy consumption and losses, to prevent power cuts [1]–[4]. Power system loads may have different characteristics. The simplest load models could be obtained using mainly three approaches: constant impedance, constant current, or constant power. However, power system or residential loads cannot be always accurately modeled by applying each approach individually. Therefore, ZIP models that combine all these approaches are used to reach most accurate electrical load models. Modeling of active and reactive powers of a device as a function of load RMS voltage is done using ZIP parameters and this modeling is important not only for utility but also smart grid applications [1], [5]–[12].

Residential load modeling is becoming more important due to smart grid connection, harmonics and power requirements, dissipated power reduction etc. [1], [3], [16], [17], [8]–[15]. ZIP parameter models are commonly used to estimate static loads power consumption or loads operating in steady-state applications [1], [5]–[9]. There are parabolic and exponential load models [11], [12]. Parabolic models are commonly used. The ZIP parameters data can be extracted from data obtained by simulations or experiments [18] and least-squares method curve-fitting process is used for that purpose [1]–[10]. Experiments needed for determining ZIP parameters are quite simple: load voltage, active power, and reactive power is measured by varying the load voltage using a programmable AC voltage source or a variac [12]. Experimental data give better results than simulations. In a house, all loads are connected in parallel. To the best of our knowledge, there are no formulas given to calculate equivalent ZIP parameters of parallel connected loads using the loads individual ZIP parameters. In this paper, the ZIP parameter formulas for parallel connected loads are derived first.

CVR method is used to lower power consumption by lowering operating voltage in smart grid applications [1]. To estimate the power consumption, ZIP models of all loads are needed [1], [5], [7], [12]. Some loads have internal rectifiers and they withdraw non-sinusoidal currents. LCD monitors have lower power consumptions than CRT monitors and they are becoming more common nowadays. Due to production laws and/or regulations to

* Corresponding author. Tel: +90 264 2954305; Fax: +90 264 2955601.
E-mail addresses: syener@sakarya.edu.tr *(Ş.Ç. Yener)*, rmutlu@nku.edu.tr *(R. Mutlu)*
ORCID: 0000-0002-6211-3751 *(Ş.Ç. Yener)*, 0000-0003-0030-7136 *(R. Mutlu)*
DOI: 10.35860/iarej.614997

eliminate harmonic mitigation to utility, Computer cases, LCD monitors or LCD televisions commonly have internal power factor correction circuits. Unfortunately, not all of them in use or in sales have these power factor correction circuits [19]. In developed world, since computers and LCD monitors are very common, it is also imperative to obtain their ZIP load models, too. The studies in [5], [12] have not considered rectifier loads. The study in [20] has examined nonlinear loads such as LCD TV, LED TV and game consoles. However, it has not considered their parallel connection. In [10], the nonlinear loads are also considered in residential loads, the loads contribution to total power is also examined but the equivalent zip parameters for the parallel connected loads are not derived. Since a computer and its LCD monitor are connected in parallel, they might be interacting with each other electrically. In this paper, using experimental data and the least-squares method, their individual and parallel-connected ZIP models are obtained. Then, the formula we derived is tested for their parallel combination.

The paper is arranged as follows. In the second section, the necessary formulas ZIP parameter estimation is given and the equivalent ZIP formula is derived. In the third section, information about the measurement system, experimental results and obtained ZIP parameters are presented. The paper is concluded with the conclusion section.

2. Determination of ZIP Parameters

2.1 A Brief Explanation of ZIP Model

The active and reactive power of a load fed by a sinusoidal voltage are given as

$$P = VI\cos(\varphi_V - \varphi_I) \tag{1}$$

$$Q = VI\sin(\varphi_V - \varphi_I) \tag{2}$$

Where V and I are the rms values of the device voltage and current, respectively. φ_V is the phase of load voltage and φ_I is the phase of load current.

φ_V=0 is taken for simplicity. In steady-state, RMS current and phase of any load depend on the device rms voltage with either a known or an unknown function:

$$I = f(V) \tag{3}$$

$$\varphi_I = g(V) \tag{4}$$

That's why not only active but also reactive power can be expressed as voltage dependent function. Usually polynomial or exponential functions are used for that purpose. If we assume a second-order polynomial dependency as done in [14], [20]:

$$P = P_0\left(Z_p\left(\frac{V}{V_0}\right)^2 + I_p\left(\frac{V}{V_0}\right) + P_p\right) \tag{5}$$

$$Q = Q_0\left(Z_q\left(\frac{V}{V_0}\right)^2 + I_q\left(\frac{V}{V_0}\right) + P_q\right) \tag{6}$$

Here, P and Q are active and reactive power corresponding to rms value of the operating voltage (V); P_0 and and Q_0 are active and reactive power corresponding to rms value of the nominal voltage (V_0), respectively. Z_p, I_p and P_p are ZIP coefficients of active power component; Z_q, I_q and P_q are ZIP coefficients of reactive power component, respectively.

In this paper, Least Squares Method (LSM) is employed used to obtain ZIP coefficients based on simulated or measured voltage-power values due to its simplicity as done in [6]. Here, V_i, P_i and Q_i are measured values of voltage, active and reactive powers, respectively. The ZIP coefficients are solved using the solution matrices are given as [6], [11], [12]:

$$\begin{bmatrix} Z_p \\ I_p \\ P_p \end{bmatrix} = \begin{bmatrix} \sum_{i=1}^{N} V_i^4 & \sum_{i=1}^{N} V_i^3 & \sum_{i=1}^{N} V_i^2 \\ \sum_{i=1}^{N} V_i^3 & \sum_{i=1}^{N} V_i^2 & \sum_{i=1}^{N} V_i \\ \sum_{i=1}^{N} V_i^2 & \sum_{i=1}^{N} V_i & N \end{bmatrix}^{-1} \begin{bmatrix} \sum_{i=1}^{N} P_i V_i^2 \\ \sum_{i=1}^{N} P_i V_i \\ \sum_{i=1}^{N} P_i \end{bmatrix} \tag{7}$$

$$\begin{bmatrix} Z_q \\ I_q \\ P_q \end{bmatrix} = \begin{bmatrix} \sum_{i=1}^{N} V_i^4 & \sum_{i=1}^{N} V_i^3 & \sum_{i=1}^{N} V_i^2 \\ \sum_{i=1}^{N} V_i^3 & \sum_{i=1}^{N} V_i^2 & \sum_{i=1}^{N} V_i \\ \sum_{i=1}^{N} V_i^2 & \sum_{i=1}^{N} V_i & N \end{bmatrix}^{-1} \begin{bmatrix} \sum_{i=1}^{N} Q_i V_i^2 \\ \sum_{i=1}^{N} Q_i V_i \\ \sum_{i=1}^{N} Q_i \end{bmatrix} \tag{8}$$

The following constraints,

$$\begin{aligned} Z_p + I_p + P_p &= 1 \\ Z_q + I_q + P_q &= 1 \end{aligned} \tag{9}$$

must also be provided.

2.2 Equivalent ZIP Model of n Parallel-Connected Loads

If n electrical load is connected in parallel, for the active and reactive powers of the ***k*th** load:

$$P_k = P_{0k}\left(Z_{pk}\left(\frac{V}{V_0}\right)^2 + I_{pk}\left(\frac{V}{V_0}\right) + P_{pk}\right) \tag{10}$$

$$Q_k = Q_{0k}\left(Z_{qk}\left(\frac{V}{V_0}\right)^2 + I_{qk}\left(\frac{V}{V_0}\right) + P_{qk}\right) \tag{11}$$

The total active and reactive powers are

$$P = \sum_{k=1}^{n} P_k = \sum_{k=1}^{n} P_{0k}\left(Z_{pk}\left(\frac{V}{V_0}\right)^2 + I_{pk}\left(\frac{V}{V_0}\right) + P_{pk}\right) \tag{12}$$

$$Q = \sum_{k=1}^{n} Q_k = \sum_{k=1}^{n} Q_{0k}\left(Z_{qk}\left(\frac{V}{V_0}\right)^2 + I_{qk}\left(\frac{V}{V_0}\right) + P_{qk}\right) \tag{13}$$

By doing some math, the following equations are obtained:

$$P = \sum_{k=1}^{n} P_k = \sum_{k=1}^{n}\left(P_{0k} Z_{pk} \left(\frac{V}{V_0}\right)^2 + P_{0k} I_{pk} \left(\frac{V}{V_0}\right) + P_{0k} P_{pk} \right) = \frac{\sum_{k=1}^{n} P_{0k} Z_{pk}}{\sum_{k=1}^{n} P_{0k}} \left(\frac{V}{V_0}\right)^2 + \frac{\sum_{k=1}^{n} P_{0k} I_{pk}}{\sum_{k=1}^{n} P_{0k}} \left(\frac{V}{V_0}\right) + \frac{\sum_{k=1}^{n} P_{0k} P_{pk}}{\sum_{k=1}^{n} P_{0k}} \quad (14)$$

$$Q = \sum_{k=1}^{n} Q_k = \sum_{k=1}^{n}\left(Q_{0k} Z_{qk} \left(\frac{V}{V_0}\right)^2 + Q_{0k} I_{qk} \left(\frac{V}{V_0}\right) + Q_{0k} P_{qk} \right) = \frac{\sum_{k=1}^{n} Q_{0k} Z_{qk}}{\sum_{k=1}^{n} Q_{0k}} \left(\frac{V}{V_0}\right)^2 + \frac{\sum_{k=1}^{n} Q_{0k} I_{qk}}{\sum_{k=1}^{n} Q_{0k}} \left(\frac{V}{V_0}\right) + \frac{\sum_{k=1}^{n} Q_{0k} P_{qk}}{\sum_{k=1}^{n} Q_{0k}} \quad (15)$$

The equivalent ZIP parameters of n parallel-connected electrical loads are obtained as:

$$Z_{peq} = \frac{\sum_{k=1}^{n} P_{0k} Z_{pk}}{\sum_{k=1}^{n} P_{0k}}, I_{peq} = \frac{\sum_{k=1}^{n} P_{0k} I_{pk}}{\sum_{k=1}^{n} P_{0k}}, P_{peq} = \frac{\sum_{k=1}^{n} P_{0k} P_{pk}}{\sum_{k=1}^{n} P_{0k}} \quad (16)$$

$$Z_{qeq} = \frac{\sum_{k=1}^{n} Q_{0k} Z_{qk}}{\sum_{k=1}^{n} Q_{0k}}, I_{qeq} = \frac{\sum_{k=1}^{n} Q_{0k} I_{qk}}{\sum_{k=1}^{n} Q_{0k}}, P_{qeq} = \frac{\sum_{k=1}^{n} Q_{0k} P_{qk}}{\sum_{k=1}^{n} Q_{0k}} \quad (17)$$

Therefore,

$$P = \sum_{k=1}^{n} P_k = P_{0eq}\left(Z_{peq} \left(\frac{V}{V_0}\right)^2 + I_{peq} \left(\frac{V}{V_0}\right) + P_{peq} \right) \quad (18)$$

$$Q = Q_{0eq}\left(Z_{qeq} \left(\frac{V}{V_0}\right)^2 + I_{qeq} \left(\frac{V}{V_0}\right) + P_{qeq} \right) \quad (19)$$

Where P_{0eq} and Q_{0eq} are the active and reactive power at the nominal voltage V_0, respectively and given as:

$$P_{0eq} = \sum_{k=1}^{n} P_{0k}, \quad Q_{0eq} = \sum_{k=1}^{n} Q_{0k} \quad (20)$$

If two loads are connected in parallel (for n=2) the following parameters are obtained:

$$Z_{peq} = \frac{P_{01} Z_{p1} + P_{02} Z_{p2}}{P_{01} + P_{02}}, \quad I_{peq} = \frac{P_{01} I_{p1} + P_{02} I_{p2}}{P_{01} + P_{02}}, \quad P_{peq} = \frac{P_{01} P_{p1} + P_{02} P_{p2}}{P_{01} + P_{02}}, \quad P_{0eq} = P_{01} + P_{02} \quad (21)$$

$$Z_{qeq} = \frac{Q_{01} Z_{q1} + Q_{02} Z_{q2}}{Q_{01} + Q_{02}}, \quad I_{qeq} = \frac{Q_{01} I_{q1} + Q_{02} I_{q2}}{Q_{01} + Q_{02}}, \quad P_{qeq} = \frac{Q_{01} P_{q1} + Q_{02} P_{q2}}{Q_{01} + Q_{02}}, \quad Q_{0eq} = Q_{01} + Q_{02} \quad (22)$$

3. Experimental Results

A desktop computer with an ATX case and an LCD monitor is shown in Figure 1. An LCD monitor has a remarkable features compared to CRT monitors considering their resolution and low energy consumption. Since increasing number of LCD monitors would increase the harmonics injected to utility, regulations are made for them to have power factor correction circuits internally unfortunately not all of them have it. Uncontrolled rectifiers draw considerable harmonic content and they are the main reason for the utility harmonics.

The experiments are performed for a VESTEL desktop computer case with 300W power supply and Samsung brand 923NW model LCD display. The measurement system is shown in Figure 2. A power analyzer is used to measure and record voltage, current and powers of the load. The power analyzer has recorded the experimental data. The variable load voltage is provided using a variable transformer (a variac) connected to the utility. The variac is controlled manually to vary load voltage during the data acquisition with the power analyzer. In experiments, the active and reactive powers of the tested devices are inspected with several volt voltage increments. The starting value of the applied voltage at unloaded conditions was around 210 V and the ending value of the applied voltage is around 225 V.

Figure 1. Desktop Personal Computer and LCD screen

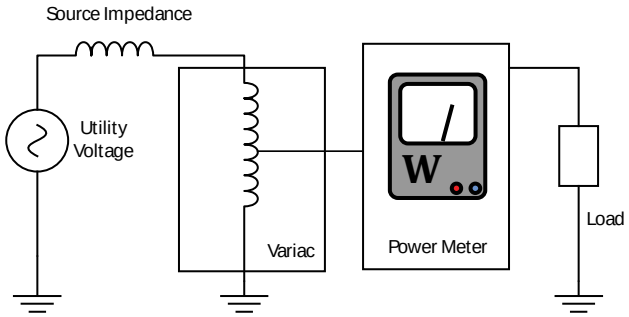

Figure 2. Measurement System

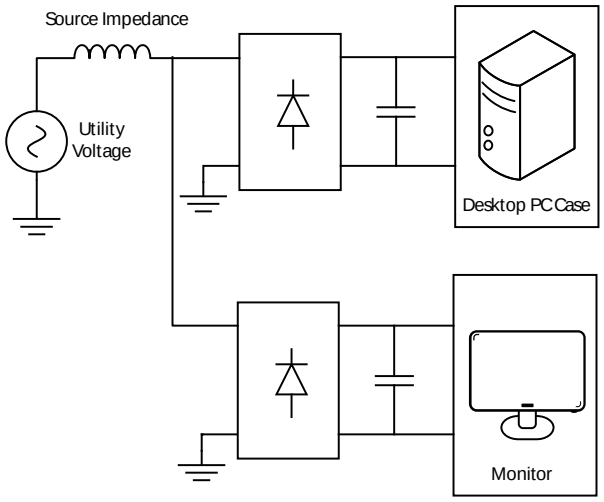

Figure 3. Equivalent circuit of the LCD monitor and Desktop computer system connected to the utility or the variac

Collected data for each specific load and the parallel combination of two loads as shown in Figure 3 is stored in an excel file and then is processed with MATLAB to calculate the ZIP coefficients.

For several voltage RMS values, the experiments are performed for loads connected separately and their parallel connection. For the space consideration, device voltage and current with respect to time for the parallel connection case is depicted in Figure 4. Active and reactive powers as a function of RMS utility voltage for LCD monitor, computer case and parallel combination of them are shown in Figure 5, Figure 6 and Figure 7 respectively. The current and voltage waveforms have harmonics at nominal voltage as shown in Figure 4. Also, it is obvious from the waveforms that the devices have no power correction circuits, just uncontrolled full-wave rectifiers with constant power loads. As shown in Figure 5, the LCD monitor has a narrow operation voltage range and it has almost constant active and reactive power. As can be seen from Figure 6, the computer case active and reactive power depends on the operation voltage and both varies about 10%.

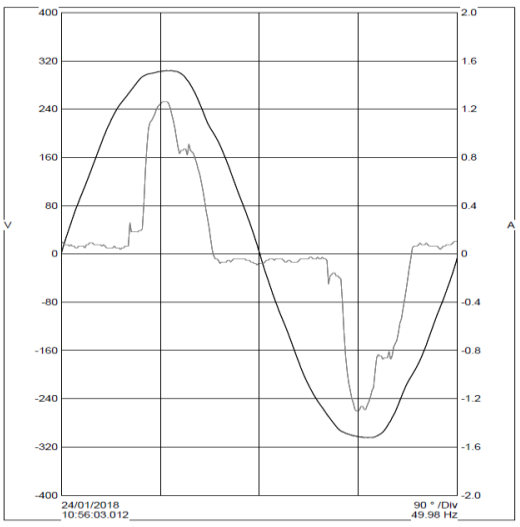

Figure 4. Paralel connection of computer case and monitor input voltage and current when the voltage effective value is 220 Volt

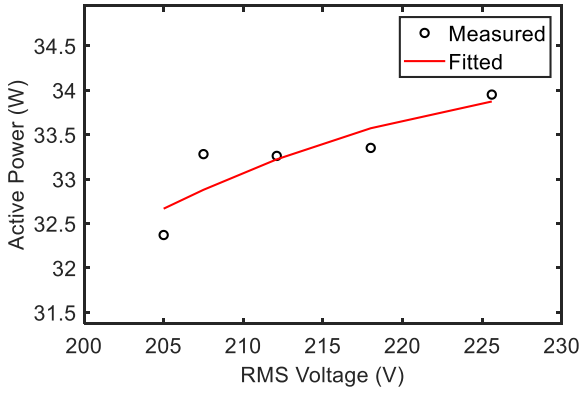

(a)

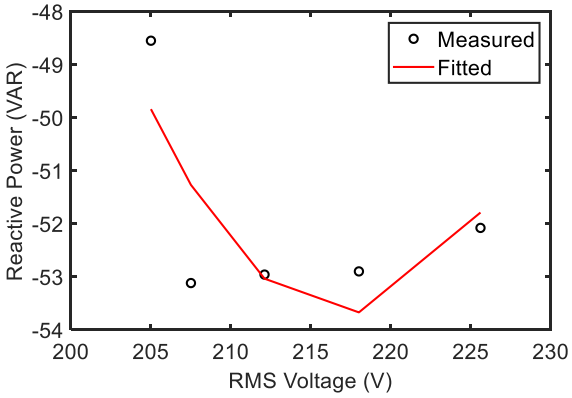

(b)

Figure 5. Active and reactive power of LCD monitor

MATLAB is used to calculate the ZIP parameters by post-processing the measured data using the LSM method. Calculated ZIP coefficients of each load and their combination are given Table 1. The equivalent ZIP parameters of the parallel loads are calculated using the formulas developed in Section 2 and listed in Table 1. The equivalent ZIP parameters calculated with the formulas is unable to predict the experimental ZIP parameters calculated from the experimental data.

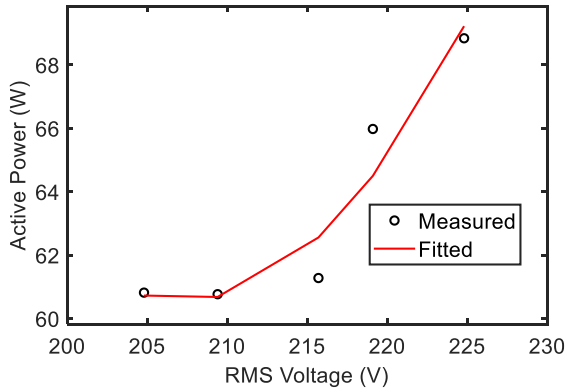

(a)

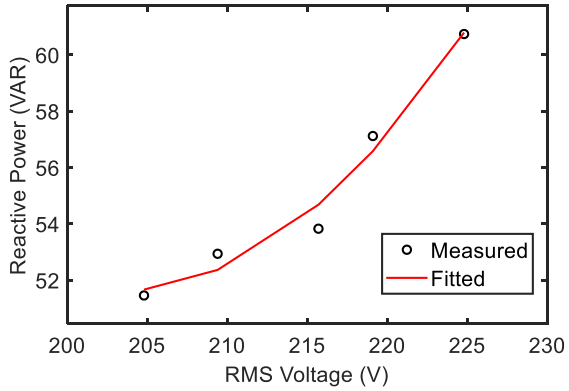

(b)

Figure 6. Active and reactive power of computer case

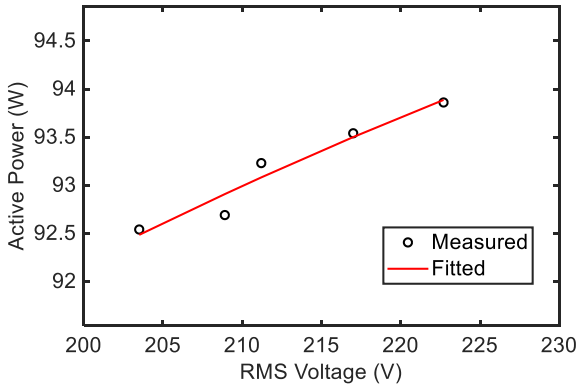

(a)

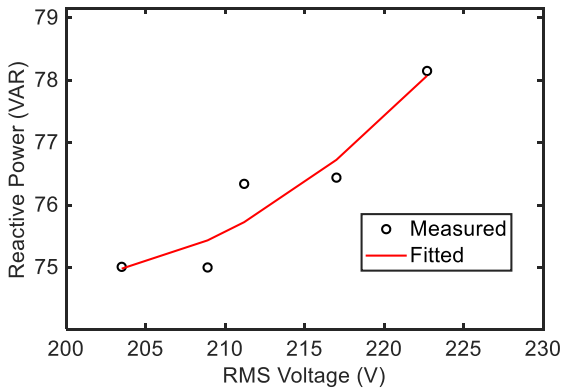

(b)

Figure 7. Active and reactive power of paralel connection of computer case and monitor

Table 1. Extracted ZIP parameters of the measured devices

Load	**P_0**	**Z_p**	**I_p**	**P_p**	**Q_0**	**Z_q**	**I_q**	**P_q**
LCD display only (experimental)	33.59	-2.10	4.49	-1.39	-52.68	-24.19	47.75	-22.54
PC case only (experimental)	66.43	20.55	-38.73	19.15	57.69	16.56	-30.61	15.03
Both device in parallel (experimental)	93.70	-0.20	0.56	0.63	77.34	3.49	-6.31	3.81
Both device in parallel (extracted)	99.93	12.95	-24.23	12.26	5.01	445.46	-855.1	410.41

4. Conclusion

In this study, for the first time in literature, a formula is derived to calculate the equivalent ZIP parameters of parallel connected loads by using their individual ZIP parameters. The formulas are tested for two loads having rectifiers. As shown in the table, the experimental and calculated equivalent ZIP parameters do not match well except for P_0. The reason can be explained as follows. As it can be seen from Figure 5 (a), the nonlinear loads both LCD monitor and PC case behave almost as constant (active) power loads. The controllers within the loads shape load currents to keep active power almost constant with just somewhat voltage dependency. Each load has a DC bus capacitor which also contributes the nonlinear dynamics.

The PC case draws inductive reactive power while as the LCD monitor draws capacitive reactive power. The nonlinear rectifier currents produce a non-sinusoidal voltage waveform at the rectifier output due to the source impedance (the variac impedance), the constant power controllers and DC bus capacitors. Since the rectifiers and their loads are not equal, each rectifier is affected differently from the non-sinusoidal input voltage exerted by the non-sinusoidal rectifier currents. Therefore, their ZIP parameters, i.e. their active and reactive power dependencies on the input rms voltage vary due to the harmonics in the rectifier voltage. Also, since the load impedance is not zero, the rectifier currents indirectly affect each other.

We have been able to estimate active power well since the constant power controllers force the loads to have constant powers and force the total active power to be sum of the load powers. There is somewhat nonlinear interaction and nonlinear reactive power compensation between the loads. That's why we are unable to predict their equivalent circuit parameters using the formula and the reactive power withdrawn from the utility by rectifiers could not be predicted with the equivalent ZIP model parameters. That's why it is important to determine ZIP parameter models of nonlinear loads or loads having a rectifier experimentally. Such a method can be applied to load extraction of the PC laboratories or big companies with computer clusters.

These formulas should also be tested for other loads. We believe it would give a better result for the nonlinear loads with low THD or for the linear loads.

Acknowledgments

The authors would like to express their thanks to Sakarya University Electromagnetic Research Center (SEMAM) for providing its technical infrastructure during experimental studies.

References

1. Azuatalam, D. T., Unigwe, O. C., and Collin, A. J., *Investigating the effects of conservation voltage reduction on UK-type residential networks*. , in *2016 Australasian Universities Power Engineering Conference (AUPEC)*, 2016, p. 1–6.
2. Bazrafshan, M. and Gatsis, N., *Convergence of the Z-Bus Method for Three-Phase Distribution Load-Flow with ZIP Loads*. IEEE Transactions on Power Systems, 2018. **33**(1): p. 153–165.
3. Tushar, Pandey, S., Srivastava, A. K., Markham, P., and Patel, M., *On-line Estimation of Steady-State Load Models Considering Data Anomalies*. IEEE Transactions on Industry Applications, 2017. p. 1–1.
4. Ge, Y., Flueck, A. J., Kim, D.-K., Ahn, J.-B., Lee, J.-D., and Kwon, D.-Y., *An Event-Oriented Method for Online Load Modeling Based on Synchrophasor Data*. IEEE Transactions on Smart Grid, 2015. **6**(4): p. 2060–2068.
5. Patel, A., Wedeward, K., and Smith, M., *Parameter Estimation for Inventory of Load Models in Electric Power Systems*. , in *Proceedings of the World Congress on Engineering and Computer Science 2014 Vol I WCECS 2014 22-24 October, 2014*, 2014, **I**.
6. Sadeghi, M. and Abdollahi sarvi, G., *Determination of ZIP parameters with least squares optimization method*. , in *2009 IEEE Electrical Power & Energy Conference (EPEC)*, 2009, p. 1–6.
7. del Pilar Rios, A., Agbossou, K., and Cardenas, A., *Taylor series approximation of ZIP model for on-line estimation of residential loads' parameters*. , in *2017 IEEE International Conference on Industrial Technology (ICIT)*, 2017, p. 632–637.
8. Wang, K., Huang, H., and Zang, C., *Research on Time-Sharing ZIP Load Modeling Based on Linear BP Network*. , in *2013 5th International Conference on Intelligent Human-Machine Systems and Cybernetics*, 2013, p. 37–41.
9. Haidar, A. M. A. and Muttaqi, K. M., *Behavioral Characterization of Electric Vehicle Charging Loads in a Distribution Power Grid Through Modeling of Battery Chargers*. IEEE Transactions on Industry Applications, 2016. **52**(1): p. 483–492.
10. Bokhari, A. *et al.*, *Experimental Determination of the ZIP Coefficients for Modern Residential, Commercial, and Industrial Loads*. IEEE Transactions on Power Delivery, 2014. **29**(3): p. 1372–1381.
11. Hossan, M. S. and Chowdhury, B. H., *Exponential factor dependent ZIP coefficients extraction and impacts of CVR in a utility feeder*. , in *2015 North American Power Symposium (NAPS)*, 2015, p. 1–6.
12. Durusu, A., Kekezoglu, B., Elma, O., Selamogullari, U. S., and Bircan, M., *Determination of zip coefficients for residential loads*. Pressacademia, 2017. **5**(1): p. 176–180.
13. Ai, Q., Yuan, R.-F., and He, X., *Research on dynamic load modelling based on power quality monitoring system*. IET Generation, Transmission & Distribution, 2013. **7**(1): p. 46–51.
14. Rudion, K., Guo, H., Abildgaard, H., and Styczynski, Z. A., *Non-linear load modeling — Requirements and preparation for measurement*. , in *2009 IEEE Power & Energy Society General Meeting*, 2009, p. 1–7.
15. Yener, S. C., Yener, T., and Mutlu, R., *A process control method for the electric current-activated/assisted sintering system based on the container-consumed power and temperature estimation*. Journal of Thermal Analysis and Calorimetry, 2018. **134**(2): p. 1243–1252.
16. Yener, T., Yener, S. C., and Mutlu, R., *Finite Difference Analysis of a Resistive Sintering System Container*. Journal of Nanoelectronics and Optoelectronics, 2019. **14**(8): p. 1143–1147.
17. Sevilmiş, F. and Karaca, H., *Performance analysis of SRF-PLL and DDSRF-PLL algorithms for grid interactive inverters*. International Advanced Researches and Engineering Journal, 2019. **3**(2): p. 116–122.
18. Bing Zhao, Yong Tang, Wen-chao Zhang, and Wang, Q., *Modeling of common load components in power system based on dynamic simulation experiments*. , in *2010 International Conference on Power System Technology*, 2010, p. 1–7.
19. Rawa, M. J. H., Thomas, D. W. P., and Sumner, M., *Experimental Measurements and Computer Simulations of Home Appliances Loads for Harmonic Studies*. , in *2014 UKSim-AMSS 16th International Conference on Computer Modelling and Simulation*, 2014, p. 340–344.
20. Quilumba, F. L., Wei-Jen Lee, Heng Huang, Wang, D. Y., and Robert Louis Szabados, *Load model development for next generation appliances*. , in *2011 IEEE Industry Applications Society Annual Meeting*, 2011, p. 1–7.

Available online at www.dergipark.gov.tr

INTERNATIONAL ADVANCED RESEARCHES
and
ENGINEERING JOURNAL

Journal homepage: www.dergipark.gov.tr/iarej

International
Open Access

Volume 03
Issue 03

December, 2019

e-ISSN: 2618-575X

Research Article

Influence of fabrication temperature on the structural features of chitosan gels for tissue engineering applications

Nimet Bölgen [a,*], ***Seda Ceylan*** [b] ***and Didem Demir*** [a]

[a]*Department of Chemical Engineering, Mersin University, Mersin 33110, Turkey*
[b]*Department of Bioengineering, Adana Alparslan Türkeş Science and Technology University, Adana 01250, Turkey*

ARTICLE INFO

Article history:
Received 26 October 2018
Revised 17 August 2019
Accepted 09 September 2019

Keywords:
Chitosan
Cryogel
Hydrogel
Scaffold
Tissue engineering

ABSTRACT

Chitosan is a natural polymer synthesized from the chitin of crab, lobster shells, fungal mycelia and shrimp. It has been used for biomedical applications in many different structures including thin film, nanofibrous membrane, sponge, microsphere, hydrogel and cryogel because of its non-toxicity, biodegradability, biocompatibility and antibacterial properties. Cryogelation technique is based on the crosslinking of polymers or crosslinking polymerization of monomers in the presence of crosslinking agents at temperatures below zero. On the other hand, hydrogels are mainly prepared at room temperature. In this study, chitosan gels were prepared at different reaction temperatures (-25, 0 and +25°C). Swelling profiles revealed that with decreasing reaction temperature swelling ratio increased. In addition, the degradation rate of chitosan gels prepared at -25 and +25°C was measured 50.60 and 30.88%, respectively. Results indicate that reaction temperature affects the architecture and characterization results of the gels.

1. Introduction

Tissue engineering is a scientific discipline that includes medical, engineering and biological sciences and works to preserve and improve tissue structure and quality of life. The aim of tissue engineering is to regenerate damaged tissues by combining scaffolds with cells and biomolecules.

Tissues made up of cells and extracellular matrix (ECM). A well-designed scaffold for tissue engineering applications should have similar mechanical and biophysical properties to ECM. Scaffolds are considered as an artificial ECM [1]. The ECM provides a three-dimensional microenvironment for the cells. In addition to providing physical support for cells, it organizes cell-cell interactions and provides various biochemical and biophysical cues for cell adhesion, cell-cell communication, migration, growth, proliferation, differentiation and ECM accumulation [2]. The use of polymeric materials to mimic the target tissue and produce scaffolds with different properties is a common practice in tissue engineering applications. The biomaterials used for this purpose can be formed in gel form. Hydrogels are obtained by gelation of the polymers at room temperature. The gels obtained by freezing the solution in the cooler is called cryogel.

Hydrogels: Polymeric hydrogels are biomaterials that have water absorption capacity and are water-insoluble due to the chemical or physical crosslinking of the polymer chains [3],[4]. Hydrogels may be prepared from natural and synthetic polymers. Examples of natural polymers are proteins (collagen) and polysaccharides (chitosan, dextran and alginate). Polymers from natural origin support cellular activities such as proliferation, differentiation and migration. They are biocompatible and biodegradable. On the other hand, they have low mechanical strength and batch variation. Hydrogels are commonly used in tissue engineering studies such as ECM, drug release systems and biosensors. Vinyl acetate, acrylamide, ethylene glycol monomers can be used to obtain synthetic polymers.

* Corresponding author. Tel.: +90 324 361 00 01; Fax: +90 324 361 00 32
E-mail addresses: nimet@mersin.edu.tr *(N. Bölgen)*, sceylan@adanabtu.edu.tr *(S. Ceylan)*, didemdemir@mersin.edu.tr *(D. Demir)*
ORCID: 0000-0003-3162-0803 *(N. Bölgen)*, 0000-0002-1088-7886 *(S. Ceylan)*, 0000-0002-2977-2077*(D. Demir)*
DOI: 10.35860/iarej.475136

Characterization properties of synthetic polymers can be precisely controlled and tailored. Hydrogels produced from synthetic polymers can have different degradability and functionality due to their modifiable properties. Hydrogels show a great resemblance to natural soft or hard tissues because of the biocompatibility, biodegradability and water absorption capacity. The gel cross-linking grade, the chemical structure of the hydrogel-forming monomers and environmental stimulants such as temperature, pH and ionic strength are important factors affecting the hydrogel bond structure [5]. Hydrogels are inert in normal biological reactions and resistant to degradation. In addition, hydrogels can be sterilized easily by heat, ethanol or UV radiation [6].

Cryogels: Cryogels are super macroporous three-dimensional polymeric gel matrices prepared from partially frozen solutions of monomeric or polymeric initiators. In the cryogel preparation process, the initiators are rapidly dissolved in an appropriate solvent. The steps of cryogelation process can be sorted as phase separation with ice-crystal formation, secondly crosslinking-polymerization and finally thawing of ice crystals to obtain cryogels with interconnected pores [7]. The interconnected macropores of the cryogels provide mass transfer of nanoparticles and nutrients. Unique pore structures, mechanical, osmotic and chemical stability makes the cryogels interesting biomaterials for the chromatographic applications of biological nanoparticles such as viruses and plasmids and cell organelles. Characteristic properties of cryogels can be changed by optimizing steps of the process for targeted tissue.

Effects of the different factors of cryogelation process can be listed as follows:

Freezing process: The macropores of cryogels can be hundreds of micrometers. The pore size varies depending on the cryogelation regime and temperature. As the freezing temperature drops, smaller ice crystals will be obtained. In order to optimize pore diameter, cryogelation temperature can be adjusted for targeted tissue [8],[9].

Crosslinker: Crosslinking amount is important in terms of the properties of cryogels. The higher amount of crosslinker is used, the lower water swelling rate and absorption capacity are obtained. Cryogels can also be produced by freezing/thawing techniques without crosslinkers. In this case, no additional treatment is required to remove crosslinking agents remaining in the tissue scaffold [8],[9].

Polymer concentration: Elasticity and fragility of cryogels depend on the initial polymer concentration. The higher polymer concentration of the initial reaction mixture is prepared, the denser and fragile matrices are obtained, and as the initial concentration is reduced, the matrices begin to exhibit a more elastic and spongy structure [7],[8].

In this study, scaffolds were produced in hydrogel and cryogel forms at different reaction temperatures using chitosan natural polymer. Chitosan is obtained from deacetylation of chitin by alkaline hydrolysis or enzymatic methods [10]. Chitosan is a biocompatible, biodegradable, non-toxic and antimicrobial polymer and these properties make it a suitable source for use in the biomedical field.

The chemical structure, surface morphology, swelling and degradation behaviors of the produced gels were investigated and the effect of the reaction temperature on the characterization of the material was compared for tissue engineering applications.

2. Materials and Methods

2.1 Materials

Chitosan (low molecular weight) was obtained from Sigma Aldrich (USA). Glutaraldehyde (25%, v/v, GA) and acetic acid (100%, glacial) were purchased from Merck (Germany).

2.2 Production of Chitosan Cryogels and Hydrogels

All gels were prepared at 1% (w/v) constant chitosan concentration. After the calculated amount was weighed, 6% (v/v) acetic acid solution was added and the solution was mixed until a homogeneous solvent was obtained. At room temperature, magnetic stirrer was used to mix solution. The structural differences of the gels were examined by changing gelation temperature as -25, 0 and +25°C.

GA was added as a crosslinking agent (5% weight of total polymer concentration) to chitosan solutions. The prepared solution was quickly put into a plastic syringe and placed into the cryostat for crosslinking reaction at specified temperatures (-25 and 0°C). Gelling at +25°C was carried out at room temperature. The structure formed at -25 and 0°C is called cryogel and the structure formed at +25°C is called hydrogel.

The cryogels formed at -25 and 0°C were kept at the specified temperatures for 4 hours while the hydrogel formed at +25°C was kept at room temperature for 4 hours. Then all the gels were left in the freezer for 20 hours. The frozen materials were thawed at room temperature. All gels were washed several times with distilled water to remove the unreacted chitosan and GA. The produced gels were freeze-dried by lyophilization.

2.3 Characterization of Gels

Functional groups of the produced chitosan gels were analyzed by Fourier Transform Infrared Spectrometer (FTIR) (Perkin Elmer, USA) between 500 and 4000 cm^{-1} wavelengths. Scanning electron microscopy (SEM) (Zeiss, Supra55, USA) was used to determine the morphology (pore structure, size, wall thicknesses and homogeneity) of the gels after coating with platinum at 5 kV for 1000x magnification ratios. The swelling capacity of the chitosan gels was calculated according to the method demonstrated in our

previous study [11]. Firstly, all samples were dried and weighed (Wi). At specified time intervals, filter paper was used to remove the excess water from the surface of cryogels and the cryogels were then weighed again (Wf). The swelling ratio (SR%) was determined using Equation (1):

$$SR\% = \frac{Wf-Wi}{Wi} \times 100 \quad (1)$$

Degradation behavior of the chitosan gels was determined by gravimetric analysis. The samples were incubated in distilled water at 37ºC in a shaking waterbath (DaihanScientific, WiseBath WB-22, Korea) at 60 rpm for 21 days. After 21 days the gels were dried and weighed (Wd). The degradation rate (DR%) was calculated according to Equation (2):

$$DR\% = \frac{Wi-Wd}{Wi} \times 100 \quad (2)$$

Statistical analysis of degradation ratio data was performed with one-way analysis of ANOVA. Statistical significance was defined as $p<0.05$.

3. Results and Discussion

In the present study, we aimed to investigate the effect of reaction (between chitosan and glutaraldehyde) temperature on the structure and physicochemical properties of the produced gels. In our preliminary studies, all gels were held at determined reaction temperatures (-25, 0 and +25°C) for 24 hours, respectively. Then, all gels were washed with large volume of distilled water to eliminate the uncrosslinked ingredients especially glutaraldehyde which is highly toxic for cells. However, while doing washing, the surface of the gel prepared at +25°C called hydrogel began to crack with rapid swelling behavior of hydrogel (Figure 1A). The high amount of water in the resulting structure could not be sublimated within 2 days in a lyophilizer. To overcome this, the crosslinking reaction time was limited to 4 hours (by considering that the reaction will be completed in a shorter time) and left in the freezer for 20 hours for mechanical stability. There are many studies in the literature where low reaction times are used to produce scaffolds from different polymers [12],[13]. It can be seen that the gels produced by this procedure are more stable and smoother as shown in Figure 1B.

3.1 FTIR

The chemical structure of the chitosan and crosslinked chitosan gels at different temperatures was analyzed using FTIR. The FTIR spectrums of the samples are demonstrated in Figure 2. The spectra show the typical bands of chitosan at 2925 and 3445 cm^{-1} ($–NH_2$) and carbonyl group band at 1477cm^{-1}.

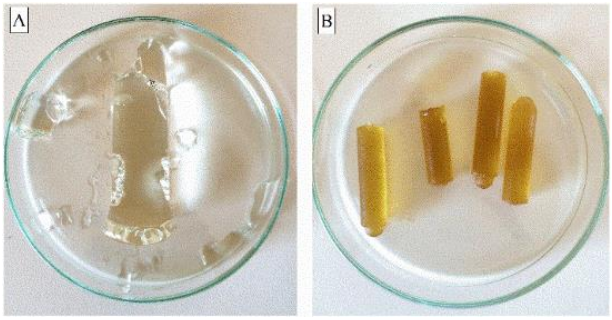

Figure 1. Gels with different crosslinking reaction times (A: 24 hours at room temperature, B: 20 hours at refrigerator after 4 hours at room temperature)

The crosslinking reaction between the aldehyde groups of glutaraldehyde and free amino groups of chitosan was proven by the existence of the peak at 1646 cm^{-1} from the imine bonds N=C [14]. This peak was observed for all the crosslinked chitosan gels.

The FTIR spectrum of pure chitosan and gels revealed that the C-OH stretching vibration at 1073 cm^{-1} for pure chitosan shift to 1037 cm^{-1} after crosslinking reaction with GA. The intensity of the peaks located at 1037 and 1646 cm^{-1} increase with increasing reaction temperature. The increasing band intensity for high temperatures may be related to the crosslinking degree of chitosan gels.

Furthermore, the CH_3 bending vibration at 1363 cm^{-1} and C–O–C bending vibration at 1155 cm^{-1} were observed in the spectrum of chitosan, but not in the spectrum of crosslinked chitosan [15]. In contrast, the band at 1559 cm^{-1} (amide II) was found in the spectra of GA crosslinked chitosan, but not in the spectra of pure chitosan.

Also, the formation of cross-links between chitosan and GA causes a color change of the chitosan gels from transparent to yellows [16].

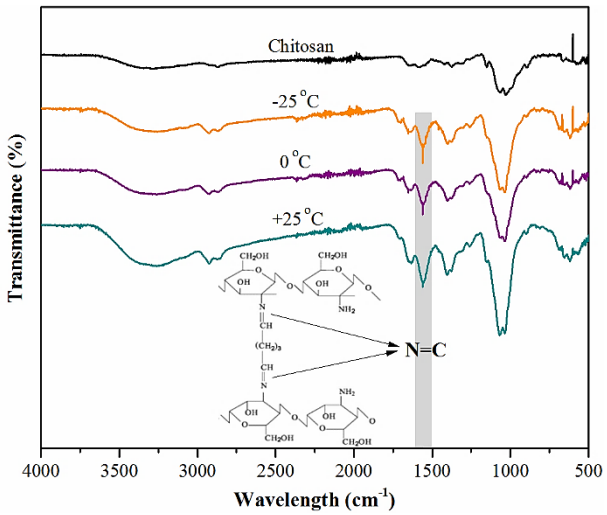

Figure 2. FTIR spectrums of chitosan and crosslinked chitosan gels

3.2 SEM

Pore size and porosity design of scaffolds are considered as important parameters for tissue engineering applications. Figure 3 shows a comparison of the pore morphology and pore size distribution of the produced chitosan cryogels and hydrogel. The images demonstrated that the cryogels exhibited an interconnected pore morphology as seen in Figure 3A and B. The steps of the cryogelation process can be sorted as phase separation with ice-crystal formation, crosslinking and polymerization followed by thawing of ice-crystals to form an interconnected porous cryogel network [7]. The microenvironment is important for cell behavior because cell attachment, infiltration, proliferation and differentiation were affected interconnected pore structure of the cryogels [17].

The pore size distribution of cryogels prepared at -25 and 0°C was shown in Figure 3A and B, where the mean pore size was calculated as 21.57 and 24.22 µm, respectively. Although the average pore size of the cryogels was not directly affected by the cooling temperature, the pore size distribution diagram showed that the cryogels produced at -25°C were relatively regular (Figure 3). This is due to the formation of ice crystals at -25°C. The ice crystals formed acted as pore-forming agents during the crosslinking process. Another reason is that it may contribute to the formation of more regular pores by stabilizing the polymer network [18].

The inner matrix of the hydrogel was also explored by SEM as seen in Figure 3C. The hydrogel surface displayed thin polymer walls with irregular pores. The mean pore size diameter of hydrogel was 38.95 µm with a wide distribution of pore size.

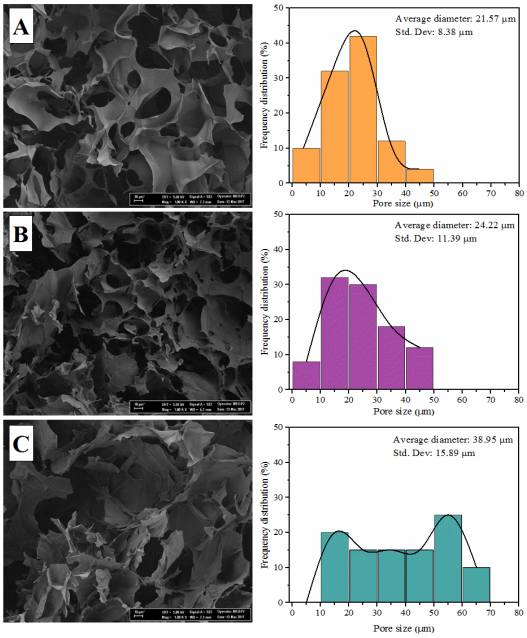

Figure 3. SEM images and pore size distribution diagram of chitosan gels (A: -25˚C, B: 0˚C and C: +25˚C at 1000× magnification)

3.3 Swelling and Degradation Behaviors of Gels

Swelling behavior is an important parameter which influences the physical and chemical properties of the scaffolds after and before implantation and supplies of nutrients and oxygen to the interior regions [19].

The swelling ratios of the produced gels are presented in Figure 4. The samples were monitored and the duration of the equilibrium was determined as approximately 20 min. All gels have the ability to retain more water than their dry weight due to the porous and hydrophilic structures [20].

The degradation of polymeric network is another significant parameter for determination of how far a scaffold can withstand to support tissue regeneration or formation [20]. The weight loss of the gels was demonstrated in Figure 5 by the *in vitro* degradation test for 21 days. The results were related to the water uptake capacity of gels as determined in swelling ratio analysis. As the swelling ratio increased more water was absorbed by the gels, which resulted in a faster degradation rate.

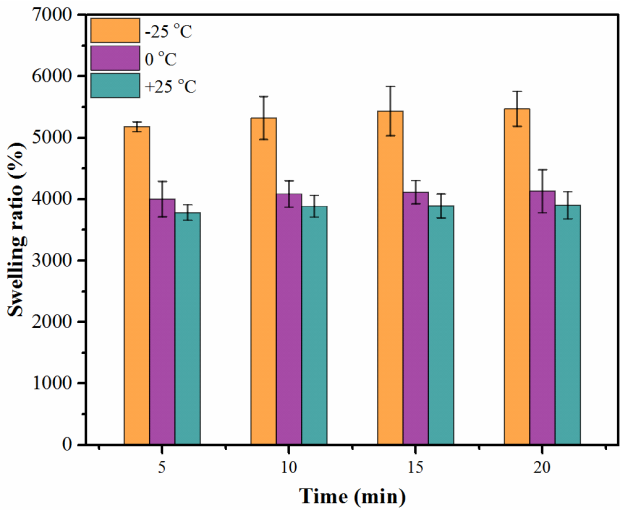

Figure 4. Swelling ratio of chitosan gels

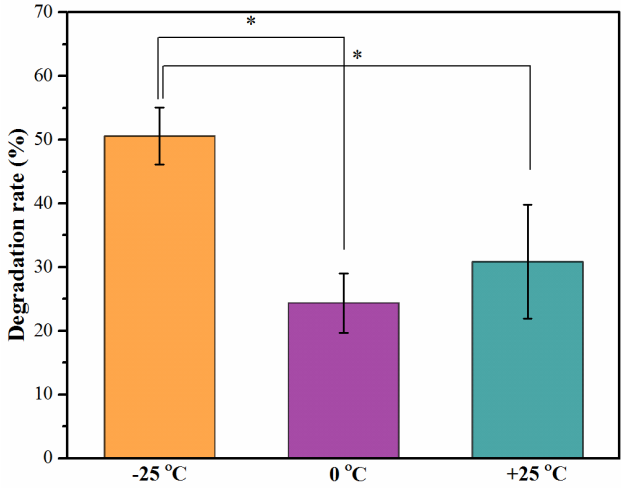

Figure 5. Degradation rate of chitosan gels [Asterisk (*) indicates significant statistical difference (p≤0.05, compared between gels)]

4. Conclusions

Chitosan gels were fabricated by crosslinking of chitosan in the presence of a crosslinker at different reaction temperatures. The synthesis and characterization of the gels were successfully shown. FTIR spectrum of scaffolds proves crosslinking reaction between the free amino groups of chitosan and aldehyde groups of glutaraldehyde. Characterization studies have revealed that the surface morphology (pore size and pore size distribution), swelling and degradation profiles of produced cryogels and hydrogel are different. The synthesized cryogels exhibit an interconnected and homogeneous pore structure, while the hydrogel is an irregular pore structure with thin polymer walls. Comparing the swelling and degradation behavior of cryogels, it was observed that gel prepared at -25°C showed a higher water uptake and weight loss rate than gels prepared at 0°C and +25°C. This distinction is due to the basic difference in their pore morphology and wall thickness. Furthermore, the desired properties of chitosan gels such as swelling, degradation and morphology can be adjustable by changing the reaction temperature. The high-water uptake capacity and porous structure of the produced gels would enable to design novel scaffolds for use in potential applications in tissue engineering and biomedical field.

Nomenclature

DR : Degradation rate
ECM : Extracellular matrix
FTIR : Fourier Transform Infrared Spectrometer
min : minute
SEM : Scanning electron microscopy
SR : Swelling ratio
Std. dev : Standard deviation
Wd : Degradation weight
Wf : Final weight
Wi : Initial weight

References

1. Aamodt, J.M., and D.W. Grainger, *Extracellular matrix-based biomaterial scaffolds and the host response*. Biomaterials, 2016. **86**: p. 68-82.
2. Gümüşderelioğlu, M., B. Maviş, A. Karakeçili, A.S. Kahraman, S. Çakmak, S. Tığlı, T.T. Demirtaş, and S. Aday, *Doku mühendisliğinde nanoteknoloji*. Bilim ve Teknik Dergisi Yeni Ufuklara, 2007.
3. Patel, N.R., and P.P. Gohil, *A review on biomaterials: scope, applications & human anatomy significance*. International Journal of Emerging Technology and Advanced Engineering, 2012. **2**(4): p. 91-101.
4. Place, E.S, N.D Evans, and M.M. Stevens, *Complexity in biomaterials for tissue engineering*. Nature materials, 2009. **8**(6): p. 457-470.
5. Koruyucu, A. *Evaluation of crosslinking type and antibacterial activities of copper oxide loaded cotton textile fabrics*. International Advanced Researches and Engineering Journal, 2018. **2**(3): p. 278-281.
6. Gümüşderelioğlu, M., *Biyomalzemeler*. Tübitak, 2002.
7. Kumar, A., R. Mishra, Y. Reinwald, and S. Bhat, *Cryogels: Freezing unveiled by thawing*. Materials Today, 2010. **13**(11): p. 42-44.
8. Değirmenci, E., *Polivinil Alkol Membranlara İtakonik Asit Aşılanması*. 2006.
9. Lozinsky, V.I, and F.M. Plieva, *Poly (vinyl alcohol) cryogels employed as matrices for cell immobilization. 3. Overview of recent research and developments*. Enzyme and Microbial Technology, 1998. **23**(3-4): p. 227-242.
10. Çırak, T., *Preparation and characterization of active agent loaded polymeric scaffolds for ophthalmologic applications*. 2008.
11. Demir, D., F. Öfkeli, S. Ceylan, and N. Bölgen, *Extraction and characterization of chitin and chitosan from blue crab and synthesis of chitosan cryogel scaffolds*. Journal of the Turkish Chemical Society, Section A: Chemistry, 2016. **3**(3): p. 131-144.
12. Ji, C., N. Annabi, A. Khademhosseini, and F. Dehghani, *Fabrication of porous chitosan scaffolds for soft tissue engineering using dense gas CO_2*. Acta Biomaterialia, 2011. **7**(4): p. 1653-1664.
13. Budianto, E., S.P. Muthoharoh, and N.M. Nizardo, *Effect of crosslinking agents, pH and temperature on swelling behavior of cross-linked chitosan hydrogel*. Asian Journal of Applied Sciences, 2015. **3**(05): p. 581-588.
14. Beppu, M.M., R.S. Vieira, C.G. Aimoli, and C.C. Santana, *Crosslinking of chitosan membranes using glutaraldehyde: Effect on ion permeability and water absorption*. Journal of Membrane Science, 2007. **301**(1-2): p. 126-130.
15. Li, B., C-L. Shan, Q. Zhou, Y. Fang, Y-L. Wang, F. Xu, L-R. Han, M. Ibrahim, L-B. Guo, and G-L. Xie, *Synthesis, characterization, and antibacterial activity of cross-linked chitosan-glutaraldehyde*. Marine Drugs, 2013. **11**(5): p. 1534-1552.
16. Ostrowska-Czubenko, J., M. Gierszewska, and M. Pieróg, *pH-responsive hydrogel membranes based on modified chitosan: water transport and kinetics of swelling*. Journal of Polymer Research, 2015. **22**(8): p. 1-12.
17. Yetiskin, B., C. Akinci, and O. Okay, *Cryogelation within cryogels: Silk fibroin scaffolds with single-, double- and triple-network structures*. Polymer, 2017. **128**: p. 47-56.
18. Ran, D., Y. Wang, X. Jia, and C. Nie, *Bovine serum albumin recognition via thermosensitive molecular imprinted macroporous hydrogels prepared at two different temperatures*. Analytica Chimica Acta, 2012. **723**: p. 45-53.
19. Nazemi, K., F. Moztarzadeh, N. Jalali, S. Asgari, and M. Mozafari, *Synthesis and characterization of poly (lactic-co-glycolic) acid nanoparticles-loaded chitosan/bioactive glass scaffolds as a localized delivery system in the bone defects*. BioMed research international, 2014. **2014**: p. 1-9.
20. Çetinkaya, Z., D. Demir, and N. Bölgen, *Fish skin ısolated collagen cryogels for tissue engineering applications: purification, synthesis and characterization*. Journal of the Turkish Chemical Society, Section A: Chemistry, 2016. **3**(3): p. 329-348.

Available online at www.dergipark.gov.tr

INTERNATIONAL ADVANCED RESEARCHES
and
ENGINEERING JOURNAL

Journal homepage: www.dergipark.gov.tr/iarej

e-ISSN: 2618-575X

International
Open Access

Volume 03
Issue 03

December, 2019

Research Article

Constrained model predictive control for the quadruple-tank process

***Zohra Zidane** **

Team of Applied Physics and New Technologies, Department of Physic, Polydisciplinary Faculty, University of Sultan Moulay Slimane, B.P: 592, 23000 Beni-Mellal, Morocco

ARTICLE INFO

Article history:
Received 04 March 2019
Revised 16 September 2019
Accepted 27 October 2019

Keywords:
Model predictive control
MIMO systems
ARIMAX systems
Non-minimum phase systems
Quadrupule-tank
Quadratic programming
Prediction

ABSTRACT

Model Predictive Control (MPC) is an advanced method of controllers, explicitly uses of model to obtain control signal. MPC is popular in industry and academia because it is capable to deals with non-minimum phase, unstable, dead time and multivariable processes, and solves the problem of constraints. MPC with integral action method is used in this study for the quadruple tank system by taking the lower two tanks into account. The objective of this work is to design and study the MPC method for controlling the level of tanks in a quadruple tank process depending on type of constrained problems. However, to solve the problem of constraints is not easy way. The methods based on the quadratic programming function and 'if-else' technique are presented to solve the problem of the process constraints in MPC. A comparative study is performed with the quadratic programming function and 'if-else' technique. The performance of the proposed method is tested for reference tracking and disturbance rejection behavior. Simulation results are presented and discussed to show the performance of the controller.

1. Introduction

Developing effective control methods for the control of industrial processes in many areas of engineering is difficult because of the long and tedious identification of models [1].

The Model Predictive Control, MPC, has been the most used technique in more than 30 years and has become an important tool in many industrial process applications [2].

The predictive control applications that have been used successfully are [3]:

- Clinical anesthesia.
- Robotic.
- Chemical engineers.
- Cement industry.
- Electric servo motor, etc.

Predictive control is an effective strategy for solving constraints and dynamics of nonlinear systems, when the analytical computation of the control signal is difficult [4, 5]. This methodology is very used in industries, where the dynamics of the system are slow enough to allow its implementation [6].

The powerful of MPC controllers are its ability to manage constraints, non-minimal phase processes, changes in system parameters and its great applicability to the Multi Input Multi Output (MIMO) processes [7], [8].

Model Predictive Control, MPC, also known as receding horizon control, uses the range of control methods, making the use of the process model to predict the output and the control signal obtained by minimizing the quadratic cost function [9]. The effectiveness of the controller depends on the quality of the system dynamics captured by the input-output model used for controller design [10].

Constraints of different types are ubiquitous in the control of industrial processes; how to deal with them in the design of the control system is an important issue. Ignore the constraints or impose them on the control signal in a heuristically can lead to a deterioration of the performances, or even instability, in particular for the predictive control of the unstable systems.

* Corresponding author. Tel.: +212-(0)-523-4246 85/16 ; Fax: +212-(0)-523-4245 97.
E-mail addresses: zohra.zidane@usms.ma; zidane.zohra@gmail.com *(Z. Zidane)*
ORCID: 0000-0002-5603-8011 *(Z. Zidane)*
DOI: 10.35860/iarej.535552

Taking constraints into consideration in the design phase inherently leads to solving the constrained optimization problem. The quadratic programming (QP) techniques can be applied to the resolution of various types of constrained predictive control problems [11, 12].

The MPC algorithms usually assume that all signals have an unlimited range, although real processes have constraints (input constraint, input rate constraint, constrained output, etc). For this reason, it is necessary to use MPC controllers to cope with constrained inputs. In this work, constrained MPC is applied to the state space model of the four tank system after linearization. The MPC under constraints is given in more detail and constraint optimization techniques discussed here are based on 'quadprog' function and 'if-else' loop. Quadratic programming (QP) methods are widely used in constraint predictive control applications; see for example the comments given in [13] and [14].

In the previous paper given in [15], a comparative study of unconstrained and constrained control system behavior is developed and the method based on the Quadratic Programming (QP) technique are used to solve the constrained optimization problem. The aim of this work is to design and study the predictive controller for controlling the level of tanks in a quadruple tank process depending on type of constrained problems. However, there is no easy way to solve the problem of constraints. This study presents a comparison between the both named quadratic programming function and 'if-else' technique. The purpose of the tests will be to check if one of the two proposed methods is able to solve the problems of constraints with less calculation and lead MPC to best performance in term of good tracking and perturbation rejection capacity.

The paper is organized as follows. The one classical formulation of constrained MPC controller algorithm is presented. A benchmark quadruple tank process is considered. The efficiency and the superiority of MPC under constraints are illustrated by an example of simulation. Some concluding remarks and future prospects complete the paper.

2. MPC Algorithm

The general strategy of the MPC is shown in Figure 1 [16, 17].

1) Definition of a numerical model of the system to calculate the predicted future outputs $\hat{y}$. These depend upon the known values up to instance k, taking the current y(k) into consideration and calculate the future control signals $u(k+i), i = 1 \dots p-1$.
2) The sequence of future control signals is computed to minimize the objective function.

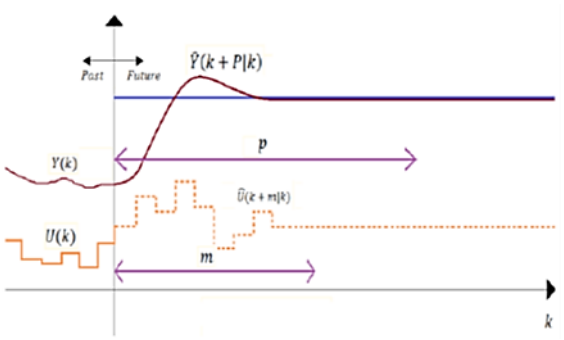

Figure 1. The receding horizon strategy of MPC [17]

3) Only the current control signal $u(k)$ is applied to the system. Next time, measure $y(k+1)$, repeat step 1 and all sequences are updated. And the control signal $u(k+1)$ is then calculated using the concept of moving horizon.

In MPC, the model used to analyze the behavior of the system [17] is linear or nonlinear. The future moves of the variables studied are obtained by minimizing the quadratic cost function.

2.1 Performance Criterion

The quadratic cost function to be minimized is:

$$J_k = \left(y_{k+1/L} - w_{k+1/L}\right)^T Q\left(y_{k+1/L} - w_{k+1/L}\right) + {u_{k/L}}^T P u_{k/L} + \Delta {u_{k/L}}^T R \Delta u_{k/L} \quad (1)$$

Where **w** is the reference signal, **y** is the output signal, **Δu** is the input changes, and **u** is the input signal. Q, R and P are the weight matrices. **L** prediction horizon.

The control law minimizing the cost is, [18]:

$$u_{k/L}{}^* = arg\ min\ J_k(u_{k/L}) \quad (2)$$

The purpose of the quadratic cost function is to reduce the difference $\left(y_{k+1/L} - w_{k+1/L}\right)$ and at the same time reduce the control $u_{k/L}$ [19].

3. Constraints Implementation

A constraint is a limitation; in practice all processes have constraints. In MPC one normally defines these constraints to minimize inequalities [20],

$$C\Delta u_{k/L} \le b \quad (3)$$

Where $C \in R^{m \times n}$ is a matrix and $b \in R^m$ is a vector.

The **input constraints** are given in linear inequality form as:

$$\begin{bmatrix} S \\ -S \end{bmatrix} \Delta u_{k/L} \le \begin{bmatrix} u_{k/L}^{max} - cu_{k-1} \\ -u_{k/L}^{min} + cu_{k-1} \end{bmatrix} \quad (4)$$

The **input rate constraint** written in linear inequality form as:

$$\begin{bmatrix} I \\ -I \end{bmatrix} \Delta u_{k/L} \leq \begin{bmatrix} \Delta u_{k/L}^{max} \\ -\Delta u_{k/L}^{min} \end{bmatrix} \quad (5)$$

The **output constraint** in linear inequality form, defined as,

$$\begin{bmatrix} G_L^{\Delta} \\ -G_L^{\Delta} \end{bmatrix} \Delta u_{k/L} \leq \begin{bmatrix} y_{max} - F_L^{\Delta} \\ -y_{min} + F_L^{\Delta} \end{bmatrix} \quad (6)$$

Input, rate and output constraints from Equations (4), (5) and (6) can be given as $C\Delta u_{k/L} \leq b$ respectively.

$$\begin{bmatrix} S \\ -S \\ I \\ -I \\ G_L^{\Delta} \\ -G_L^{\Delta} \end{bmatrix} \Delta u_{k/L} \leq \begin{bmatrix} u_{k/L}^{max} - cu_{k-1} \\ -u_{k/L}^{min} + cu_{k-1} \\ \Delta u_{k/L}^{max} \\ -\Delta u_{k/L}^{min} \\ y_{max} - F_L^{\Delta} \\ -y_{min} + F_L^{\Delta} \end{bmatrix} \quad (7)$$

Where

$$C = \begin{bmatrix} S \\ -S \\ I \\ -I \\ G_L^{\Delta} \\ -G_L^{\Delta} \end{bmatrix} \text{ and } b = \begin{bmatrix} u_{k/L}^{max} - cu_{k-1} \\ -u_{k/L}^{min} + cu_{k-1} \\ \Delta u_{k/L}^{max} \\ -\Delta u_{k/L}^{min} \\ y_{max} - F_L^{\Delta} \\ -y_{min} + F_L^{\Delta} \end{bmatrix}$$

4. MPC with Integral Action

Model predictive control has many different algorithms, depending on the numerical model of the process used for the objective function. These formulations have some problems with offset. To solve this, using the integral action it is an effective approach [21], [22].

Consider discrete-time state space model with disturbance.

$$\begin{aligned} x_{k+1} &= Ax_k + Bu_k + \zeta \\ y_k &= Cx_k + \epsilon \end{aligned} \quad (8)$$

Where A, B and C are system matrices, $x_k \in R^n$ is a state vector, $u_k \in R^r$ is input vector, $y_k \in R^m$ is output vector. ζ is process disturbance vector and ϵ is measurement noise vector.

In order to solve the problem of optimal control of the MPC, Firstly, a model without unknown perturbations is considered.

From the Equation (8), the state space model becomes,

$$\begin{aligned} \Delta x_{k+1} &= A\Delta x_k + B\Delta u_k \\ y_k &= y_{k-1} + C\Delta x_k \end{aligned} \quad (9)$$

Where,
$\Delta x_{k+1} = x_{k+1} - x_k$
$\Delta x_k = x_k - x_{k-1}$
$\Delta u_k = u_k - u_{k-1}$

The augmented form of the model shown below is obtained using the model of Equation (15),

$$\begin{aligned} \underbrace{\begin{bmatrix} \Delta x_{k+1} \\ y_k \end{bmatrix}}_{\tilde{x}_{k+1}} &= \underbrace{\begin{bmatrix} A & 0 \\ C & I \end{bmatrix}}_{\tilde{A}} \underbrace{\begin{bmatrix} \Delta x_k \\ y_{k-1} \end{bmatrix}}_{\tilde{x}_k} + \underbrace{\begin{bmatrix} B \\ 0 \end{bmatrix}}_{\tilde{B}} \Delta u_k \\ y_k &= \underbrace{\begin{bmatrix} C & I \end{bmatrix}}_{\tilde{C}} \underbrace{\begin{bmatrix} \Delta x_k \\ y_{k-1} \end{bmatrix}}_{\tilde{x}_k} \end{aligned} \quad (10)$$

A strictly proper state model written as,

$$\begin{aligned} \tilde{x}_{k+1} &= \tilde{A}\tilde{x}_k + \tilde{B}\Delta u_k \\ y_k &= \tilde{C}\tilde{x}_k \end{aligned} \quad (11)$$

$\tilde{A}, \tilde{B}, \tilde{C}$: Augmented model matrices

The predicted value of the output along the horizon will be;

$$y_{k+1/L} = F_L + G_L u_{k/L} \quad (12)$$

Where

$$F_L = O_L \tilde{A}_L \quad (13)$$

$$G_L = [O_L \tilde{B} \quad H_L^d] \quad (14)$$

Where O_L is extended observability matrix for the $(\tilde{C}, \tilde{A})$, and H_L^d is a Toeplitz matrix for $(\tilde{C}, \tilde{A}, \tilde{B})$ matrices [19].

The cost index Equation (1) with the model prediction Equation (12) can be given as quadratic objective function on standard for as,

$$J_k = \Delta u_{k/L}^T H \Delta u_{k/L} + 2 f_k{}^T \Delta u_{k/L} + J_0 \quad (15)$$

Where

$$H = G_L^T Q G_L + R \quad (16)$$

$$f_k = G_L^T Q (F_L - w_{k+1/L}) \quad (17)$$

$$J_0 = (F_L - w_{k+1/L})^T Q (F_L - w_{k+1/L}) \quad (18)$$

The optimal control deviation vector written as,

$$\Delta u_{k/L}^* = -H^{-1} f_k \quad (19)$$

Note that, the first element of $\Delta u_{k/L}^*$ is $\Delta u_{k/L}$ and the current control $u_{k/L}$ is calculated as $u_k = \Delta u_k + u_{k-1}$ [19].

5. Process Description

Quadruple tank process contains four interconnected water tanks and two pumps as given in Figure 2 [23], [24]. The process inputs are u_1 and u_2 and the outputs are $y_1 = k_c l_1$ and $y_2 = k_c l_2$.

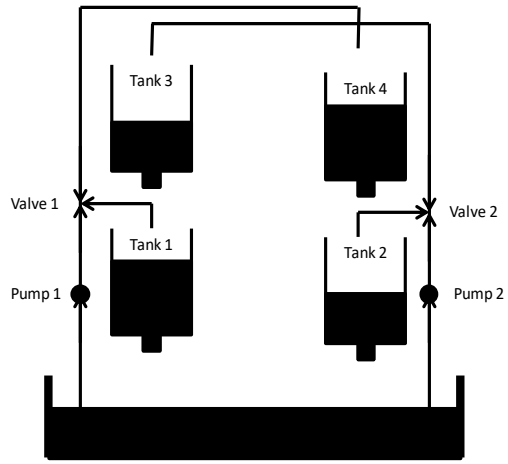

Figure 2. Schematic of the quadruple tank process [23]

The mathematical model of four tank systems is as follows [25], [26]:

$$\frac{dl_1}{dt} = -\frac{a_1}{A_1}\sqrt{2gl_1} + \frac{a_3}{A_1}\sqrt{2gl_3} + \frac{\gamma_1 k_1}{A_1}u_1 \quad (20)$$

$$\frac{dl_2}{dt} = -\frac{a_2}{A_2}\sqrt{2gl_2} + \frac{a_4}{A_2}\sqrt{2gl_4} + \frac{\gamma_2 k_2}{A_2}u_2 \quad (21)$$

$$\frac{dl_3}{dt} = -\frac{a_3}{A_3}\sqrt{2gl_3} + \frac{(1-\gamma_2)k_2}{A_3}u_2 \quad (22)$$

$$\frac{dl_4}{dt} = -\frac{a_4}{A_4}\sqrt{2gl_4} + \frac{(1-\gamma_1)k_1}{A_4}u_1 \quad (23)$$

Where;
A_i: Surface of cross section of the tank i;
a_i: Surface of cross section of the exit hole i;
l_i: Level of water in the tank i;
u_i: Voltage of the pump i;
γ_i: Constant of valve i;
k_i: Constant of pump i;
g: Acceleration due tothe gravity;
k_c: Pump gain.

The linearized state space model is [25], [26]:

$$\frac{dl}{dt} = \begin{bmatrix} -\frac{1}{T_1} & 0 & \frac{A_3}{A_1T_1} & 0 \\ 0 & -\frac{1}{T_2} & 0 & \frac{A_4}{A_2T_2} \\ 0 & 0 & -\frac{1}{T_3} & 0 \\ 0 & 0 & 0 & -\frac{1}{T_4} \end{bmatrix} l + \begin{bmatrix} \frac{\gamma_1 k_1}{A_1} & 0 \\ 0 & \frac{\gamma_2 k_2}{A_2} \\ 0 & \frac{(1-\gamma_2)k_2}{A_3} \\ \frac{(1-\gamma_1)k_1}{A_4} & 0 \end{bmatrix} u \quad (24)$$

$$y = \begin{bmatrix} k_c & 0 & 0 & 0 \\ 0 & k_c & 0 & 0 \end{bmatrix} l \quad (25)$$

The discrete four-tank plant model is as:

$$x_{k+1} = Ax_k + Bu_k$$
$$y_k = Cx_k \quad (26)$$

Where;

$$A = \begin{bmatrix} 0.9984 & 0 & 0.0026 & 0 \\ 0 & 0.9989 & 0 & 0.0018 \\ 0 & 0 & 0.9974 & 0 \\ 0 & 0 & 0 & 0.9982 \end{bmatrix};$$

$$B = \begin{bmatrix} 0.0048 & 0 \\ 0 & 0.0035 \\ 0 & 0.0077 \\ 0.0056 & 0 \end{bmatrix}; C = \begin{bmatrix} 1 & 0 & 0 & 0 \\ 0 & 1 & 0 & 0 \end{bmatrix}$$

6. Simulation Analysis

In this paper, the MPC method under imposed constraints is implemented in the state space model after linearization of the quadruple tank in the non-minimum phase region. A comparative study is performed with the quadratic programming function and 'if-else' technique.

The constant weight matrices Q and R are chosen in terms to obtain the better performances respectively,

$Q = \begin{bmatrix} 200 & 0 \\ 0 & 200 \end{bmatrix}$, and $R = \begin{bmatrix} 0.1 & 0 \\ 0 & 0.1 \end{bmatrix}$.

The initial levels in tanks 1 and 2 are 9.5 and 10.5 [cm].

The prediction horizon L of 16 is used.

The control action amplitude constraints $0 \leq u \leq 5$ is applied.

The reference is chosen as a square wave.

Simulation results are developed with Matlab® codes written to simulate a quadruple tank process.

6.1 Constrained MPC with 'quadprog' Function

The main advantages of MPC method are its capability to handle constraints [1]. Here the constraints are provided on both the input voltages to the pumps at the amplitude constraints $0 \leq u \leq 5$. The process outputs and control input signal, under constrained MPC method with 'quadprog' function, are shown in Figure 3.

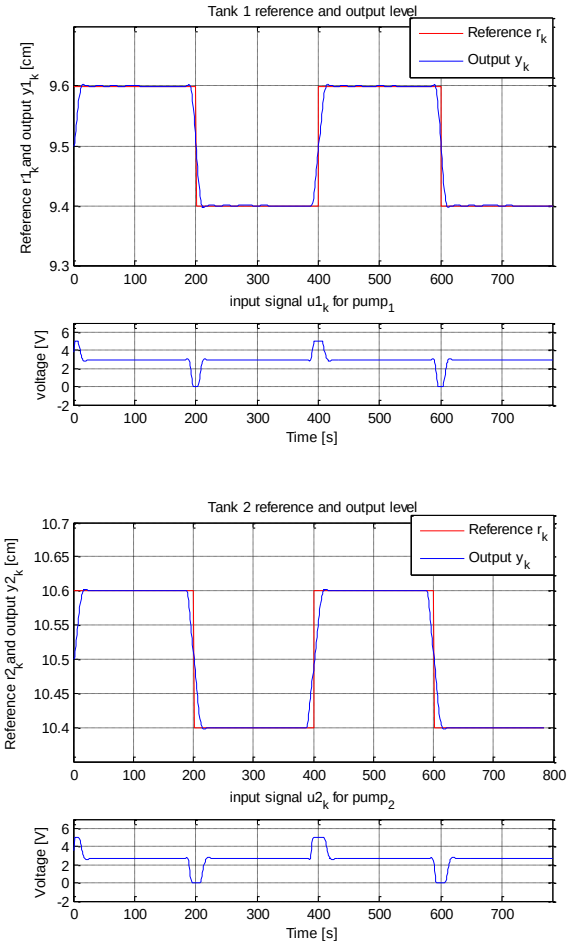

Figure 3. Quadruple tank process responses and control input signal using 'quadprog' function

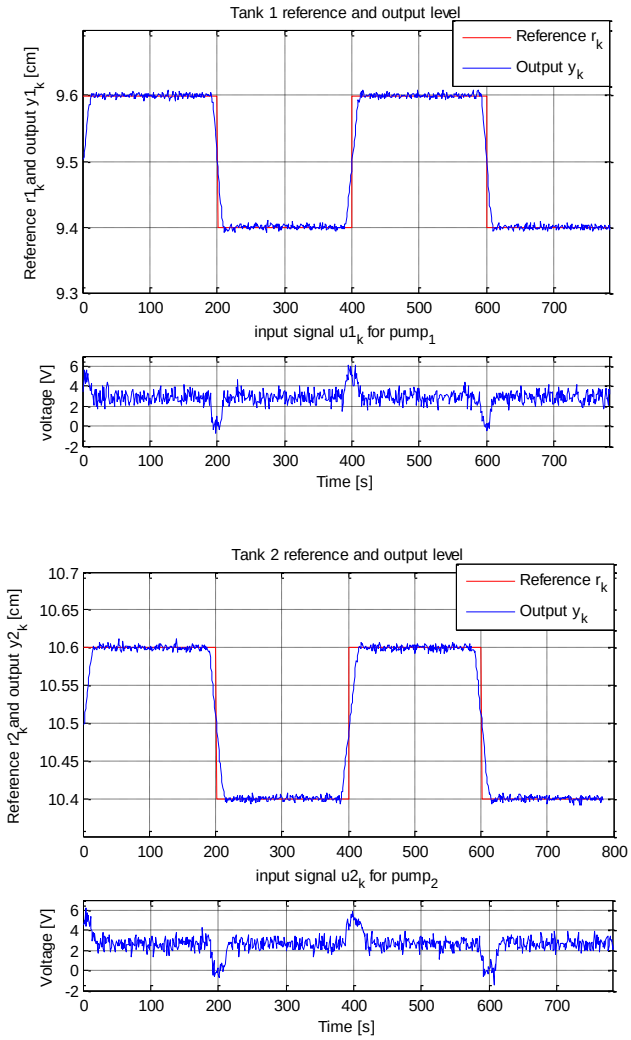

Figure 4. Quadruple tank process responses and control input signal using 'quadprog' function with a random disturbance

From the responses it is clearly shown that the output variables are able to track the set points given with no over/undershoots in both the tanks 1 and 2. When the load disturbance is applied as given in Figure 4, it can be seen that the proposed method allows guaranteeing the disturbance rejection and the tracking performance is achieved successfully. The running time of the simulation is 9.97 seconds due to complex calculation.

6.2 Constrained MPC with "if-else" Technique

The constraints are handled using "if-else" technique such as:

$u_{min} = 0$
$u_{max} = 5$

if $u < u_{min}$
$u = u_{min}$;
elseif $u > u_{max}$
$u = u_{max}$
end

The results are plotted and are given in Figure 5. From the responses it is clearly shown that the output variables are able to track the set points given with a small undershoots and overshoots in both responses of the system. When a random disturbance is applied to the system as seen in Figure 6, it can be observed that the disturbance is rejected, and the tracking performance is achieved successfully. The running time of the simulation is 2.13 seconds.

6.3 Comparison Results

In the presented Figures, it can be seen the comparative results between MPC under imposed constraints using the function 'quadprog' and the technique "if-else". The output levels for tanks 1 and 2, and the control input signal for pumps 1 and 2, under constrained MPC method with the function 'quadprog' and with the technique 'if-else' without and with the random disturbance, are shown, respectively, in Figures 3, 4, 5 and 6. Best performance is characterized by good set point tracking, robustness, lower or no over/undershoots. Based on this, it can be observed that the constrained MPC method with the function 'quadprog' produces the good response in terms of tracking and overshoot, and the effect of disturbance is well rejected. But the running time of simulation with the technique "if-else" is reduced compared to the case with the function 'quadprog'. As a result, the calculation time can be shortened and for the process with rapid dynamic, the 'if-else' technique is most interesting.

7. Conclusion

In this paper, a model predictive controller under constraints was designed using a linearized state-space model of the quadruple tank process in the non-minimum phase region. From the simulation results, it is clear that, the constrained MPC controller with 'quadprog' function has a good set point tracking and the effect of disturbance is well rejected. The running time of simulation is reduced with 'if-else' technique compared to 'quadprog' function. For the process with rapid dynamic, the 'if-else' technique is most interesting, this is particularly important in real times application.

Table 1. Comparison of Constrained MPC using 'quadprog' function and Constrained MPC using 'if-else' technique.

Parameters	Constrained MPC using 'quadprog' function	Constrained MPC using "if-else" technique
$\sum(y(k) - r(k))^2$ in tank 1	$2.6336e^{-004}$	$3.4953e^{-004}$
$\sum(u(k))^2$ in tank 1	8.6946	8.7327
$\sum(y(k) - r(k))^2$ in tank 2	$3.6109e^{-004}$	$5.3257e^{-004}$
$\sum(u(k))^2$ in tank 2	7.5232	7.6158
Execution time	9.97 seconds	2.13 seconds

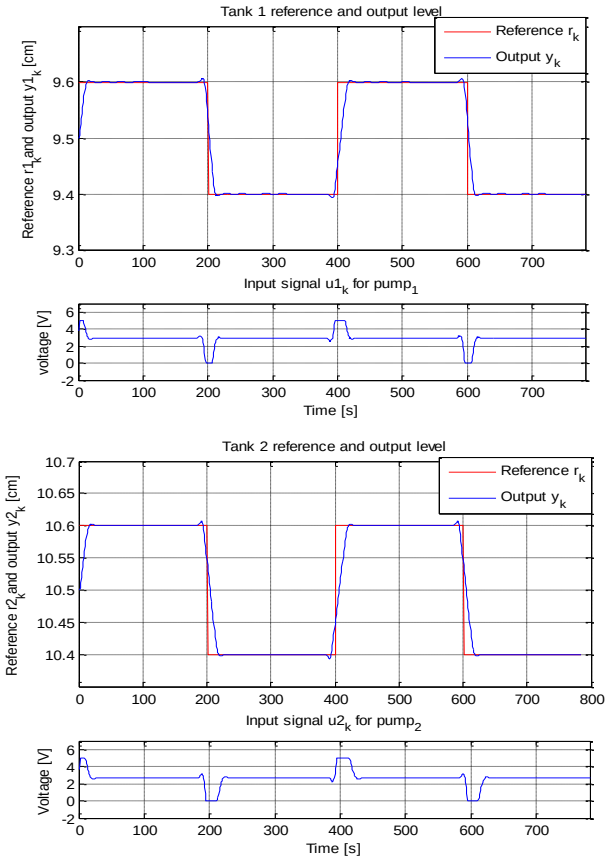

Figure 5. Quadruple tank process responses and control input signal using 'if-else' technique

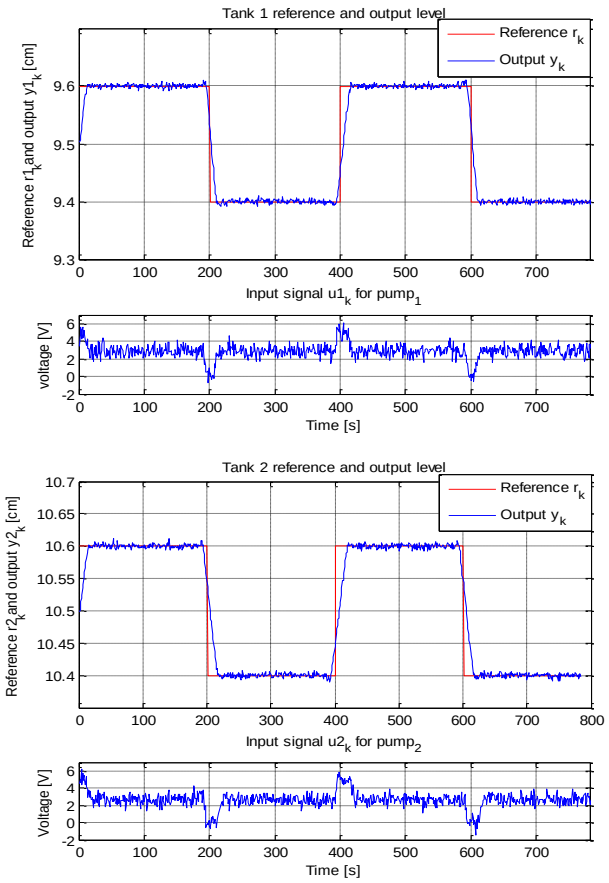

Figure 6. Quadruple tank process responses and control input signal using 'if-else' technique with a random disturbance

References

1. Morari, M. and J. H. Lee, *Model predictive control: Past, present, and future*. Comp. Chem. Eng., 1999. **23**: p. 667-682.
2. Kavery, Lal., S. Rakesh Kumar and R. Valarmathi, *Model predictive control for MIMO process*, ARPN Journal of Engineering and Applied Sciences, April 2018. **13**(7): pp. 2666-2670.
3. Gireesh, K. J. and S. Veena, *Model Predictive Controller design for performance study of coupled tank process*, ITSI Transactions on Electrical and Electronics Engineering (ITSI-TEEE), 2013. **1**(3): pp. 70-74.
4. A. Afram, A. and F. Janabi-Sharifi, *Theory and applications of HVAC control systems – A review of model predictive control (MPC)*, Building and Environment, 2014. **72**: pp. 343-355.
5. Rawlings, J. B., E. S. Meadows and K. R. Muske, *Nonlinear model predictive control: A tutorial and survey.* In IFAC ADCHEM'94, Kyoto, Japan, 1994. p.185-197.
6. Qin, S. J and T. A. Badgwell, *An overview of industrial model predictive technology*. In Chemical Process Control V, Tahoe City, CA, 1997. p. 232-256.
7. Richalet, J., *Industrial applications of model based predictive control*, Automatica, 1993. **29**: p. 1251-1274.
8. Abu-Ayyad, M. and R. Dubay, *Real-time comparison of a number of predictive controllers*, ISA Transactions, 2007. **46**: p. 411-418.
9. Holkar, K. S. and L. M. Waghmare, *Discrete Model Predictive Control for DC drive Using Orthonormal Basis function*, UKACC International Conference on control, Coventry, UK, 2010. p. 435-440.
10. Mohanty, S., *Artificial neural network based system identification and model predictive control of a flotation column*, Journal of Process Control, 2009. **19**: p. 991–999.
11. Camacho, E. F. and C. Bordons, *Model Predictive Control in the process industry*, 1995, Springer.
12. Camacho, E. F., *Constrained generalized predictive control*, IEEE Trans. Automat. Contr. , 1993. **38**: p. 327-332.
13. Rossiter, J. A. and B. Kouvaritakis, *Constrained stable generalized predictive control*, IEE Proc., Pt.D, 140, 1993. **4**: p. 243-254.
14. Kothare, M. V., V. Balakrishnan and M. Morari, *Robust constrained model predictive control using linear matrix inequalities*, Automatica, 1996. **32**(10): p.1361-1379.
15. Zidane, Z., *Unconstrained and Constrained Predictive Control for the Multivariable Process with Non-minimum Phase*, Journal of Modeling and Simulation of Materials, 2019. **2**(1): PP. 1-6.
16. Dale, D. A. M., E. Seborg, T. F. Edgar and F. J. Doyle, *Process Dynamics and Control*, 2011, 3 John Wiley & Sons.
17. Jalali, A. A. and V. Nadimi, *A Survey on Robust Model Predictive Control from 1999-2006*, International Conference on Computational Intelligence for Modeling Control and Automation, and International Conference on Intelligent Agents, Web Technologies and Internet Commerce, 2006, IEEE computer society.
18. Di Ruscio, D., *Model predictive control and identification: A linear state space model approach*, Proc. Of the 36th IEEE Conference on Decision and Control, December 10-12, 1997, San Diego, USA.

19. Di Ruscio, D., *Model predictive control and optimization*, Lecture notes for Master's course (SCE 4106), 2012, Telemark University College, Norway.
20. Di Ruscio, D, *Model predictive control and optimization*, 2001, Telemark University College.
21. Nunes, G. C, *Design and Analysis of Multivariable Predictive Control Applied to an oil-water-gas seperator: A Polynomial Approach*, 2001, University of Florida.
22. Mohsin, M., *Model Predictive control (MPC) with integral action;Reducing the control horizon and model free MPC*, Lecture notes for Master's thesis, 2013, Telemark University College, Norway.
23. Johansson, K. H, *the Quadruple-Tank Process: A Multivariable Laboratory Process with an Adjustable Zero*, IEEE Transactions on Control Systems Technology, 2000. **8**: p. 456-465.
24. Nagarajapandian, M., Kanthalakshmi S and Anitha T. *Design and Implementation of Controllers for Quadruple Tank System*, *Journal of Control & Instrumentation*, 2018. **9**(1): pp. 25–32.
25. IDivya, K. M. Nagarajapandian, and T. Anitha, *Design and Implementation of Controllers for Quadrupe Tank System***,** International Journal of Advanced Research in Education & Technology IJARE), April – June, 2017. **4**(2): pp. 158-165.
26. Kirubakarana, V., T. K. Radhakrishnana and N.Sivakumaranb, *Distributed multiparametric model predictive control design for a quadruple tank process*, Elsevier, January 2014. **47**: pp. 841-854.

Available online at www.dergipark.gov.tr

INTERNATIONAL ADVANCED RESEARCHES and ENGINEERING JOURNAL

Journal homepage: www.dergipark.gov.tr/iarej

e-ISSN: 2618-575X

International Open Access

Volume 03
Issue 03

December, 2019

Research Article

An experimental study on production of intelligent textile by using ionocromic materials

Aslıhan Koruyucu *

Namık Kemal University, Çorlu Faculty of Engineering, Department of Textile Engineering, Turkey

ARTICLE INFO

Article history:
Received 13 February 2019
Revised 21 August 2019
Accepted 28 September 2019

Keywords:
Halochromic dyes
pH-indicator
pH-sensor
Textile

ABSTRACT

The production of an intelligent textile material that changes color under the influence of pH was researched in this research article. For this purpose, halochromic dyes were used. In halochromic dyes, bleeding and fastness problems are encountered after dyeing. In order to solve these problems; the dye is fixed with cationic fixators in the textile fiber. In this study, a woven nylon fabric was dyed with Alizarin Red S halochromic dyestuff by conventional dyeing method which was followed by post-treated by tannic acid/potassium antimony tartarate at different ratios (1%, 2%, 3%). After dyeing and post-treating, CIELab, K/S, ΔE* values were measured by spectrophotometer and compared. In order to investigate the effect of halochromics on the post-treated, dyed and post-treated fabrics were immersed in 5 different solutions prepared by using HCl and NaOH between pH 2 and 10, and the samples were removed after 1 hour and the color change in the samples was compared. After the process, the speed of fixation of the dye molecule onto the fiber was increased.

1. Introduction

The textile material coloring is a well-known and broadly applicable process in which the focus is primarily on the textile material dyes development in fixed-color textile materials. [1,2]. Nowadays, interest in developing color-changing materials, such as pH sensitive textiles [8-15], has been increasing in the light of sensitive polymeric materials to stimulants [3-7].

These halochromic textiles may display a crop signal which can be effectively seen in a non-destructive manner.

Halochromic materials alter colors once pH alterations are consisted. The 'chromic' locution can be described as a material can reversibly alter color in the existence of a factor. In this instance, the factor is pH, and the pH index have these properties. At the final color, A reversible change in pH is occurred. Chromaticity is procured by the formation of a new chromophore [16]. Halochromic materials are suitable for usage in mediums in which pH changes are frequently made or pH changes are excessive. Halochromic materials assign the changes in the material acidity, such as metal corrosion detection.

Halochromic material can be applied as an indicator to determine the pH level of solution with unknown level of pH. The gained color is compared with the color sighted once the index is confused with known pH solutions. Then, the unknown solution pH can be assumed. The clear deficits of this method contain the dependence of the human eye on the color sensitivity and that unknown solutions which have already colored cannot be applied.

Conventional dyeing methods have been used in the textile industry for the purpose of coloring products for many years due to their economic and easy application.

Some of the studies in the literature on the development of textile surfaces that change color with pH, are generally the application of synthetic pH-indicator dyestuffs to conventional woven fabrics by conventional dyeing methods.

In these studies, the interaction of halochromic dyes and fiber structure and permanence of color change were investigated.

* Corresponding author. Tel.: +90 282 2502334; Fax: +90 282 250 9924.
E-mail address: adelituna@nku.edu.tr *(A. Koruyucu)*
ORCID: 0000-0002-8443-5188 *(A. Koruyucu)*
DOI: 10.35860/iarej.526440

Schueren and Clerck [17] examined that color changes between pH 2-11 of cotton, polyamide 6 and polyamide 6,6 woven fabrics for dyeing with 10 different synthetic halochromic dyes. Polyamide based fabrics showed good dyeing performance with all dyestuffs and some dyestuffs in cotton fabric. pH-indicator dyes while changing color in liquids immediately; it was observed that the color change time was prolonged when they were transferred to textile fabrics. At the end of the study, it was concluded that bright yellow and alizarin halochromic dyes are more effective and fiber type affects halochromism.

Staneva and Betcheva [18] studied on the color change of viscose rayon fabric by using a new pH sensitive dyestuff which they synthesized. Fast and reversible color change was observed in pH 5.2-11.4 from yellow to orange–red. The effect of molecular structure of synthesized new halochromic dyestuff on the change of color and fluorescent properties in the alkaline pH range was emphasized.

In this study, polyamide 6,6 woven fabric was dyed by using Alizarin Red S dye at 98 °C for 1 hour. For enhancing wet fastness, four different commercial fixators and tannic acid were used after the treatment. As a result of this study, water fastness test was applied, it was found that 3% Setafix S imparted the greatest water fastness improvement. The samples which were post-treated by tannic acid also showed good water fastness results. The washing fastness of the samples were recorded to good values, but the same results were not obtained on the original colored samples.

2. Experimental Study

2.1 Chemical Materials

All the chemical materials used for dyeing of polyamide 6,6 were of commercial grade. All solvents used were either of analytical grade or redistilled commercial grade. The following anionic fixators were used: Setafix S, Erional FRN, Polyfix PA and Hydrocol APR.

2.2 Dyeing Methods

Dyeing of polyamide 6,6 fabric was carried out using a procedure reported in the literature (Figure 3).

2.3 Procedure

Alizarin dye was provided by Sigma-Aldrich and it applied with hydrochloric acid (1mol/L), acetic acid (1M) and sodium hydroxide (50m %) for pH adjustment. pH level measure was earned by a pH meter.

10 mg/L solution's UV/vis spectra was measured on a spectrophotometer in the interval of 300-700 nm (together with a resolution of 1nm).

The measurement of the transmission in the solution and the reflection measurements of the fabrics were calculated according to absorptivity and values of Kubelka-Munk (K / S), respectively.

Each polyamide 6,6 fabric was immersed at a liquor ratio of 20:1 in a 0.7%, 1% and 1.5% on dye solution of mass fibre (omf%) that buffered at pH5.

The mix was then heated in the dyeing machine of the laboratory to 98 °C and dyeing was maintained at this temperature for 1 hour, accepting the dye molecules diffusion in the fabric [19].

The Alizarin Red S molecule chemical structure is presented in Figure 1.

The Alizarin Red S dye concentration was concluded at 520 nm. pH of the solutions was measured using a pH/ion meter and the absorption works were realized by UV - Visible spectrophotometer.

In solution, pH is an agent in the absorption treatment since it effects useful groups on surface of the absorbent and assigns the dye solubility in the aqueous solution. Figure 2 shows that the Alizarin Red S adsorption capacity was found to decrease with increasing pH in the 2-10 pH range. The adsorbent will be more positively charged sites through protonation of functional groups that increase with respect to higher pH levels, once the solution pH is about 2. According to the following reaction, under acidic conditions (pH≤2), $D\text{-}SO_3^-$ sulfonate groups with H^+ reduce the Alizarin Red S adsorption capacity [20].

$$D\text{-}SO_3^- + H^+ \rightarrow D\text{-}SO_3H \quad (1)$$

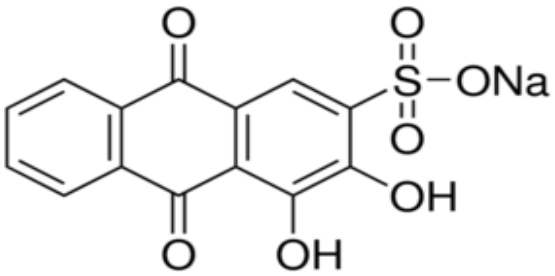

Figure 1. Alizarin Red S Chemical Structure

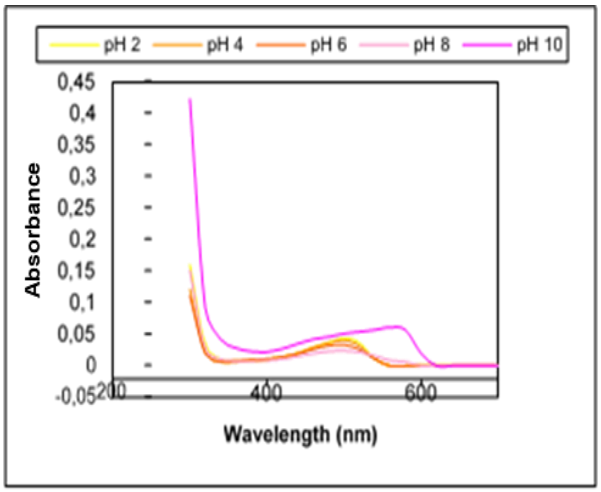

Figure 2. The pH effect on 0,7% Alizarin Red S dye removal (adsorbent 2 dose =1g, temperature= 303K).

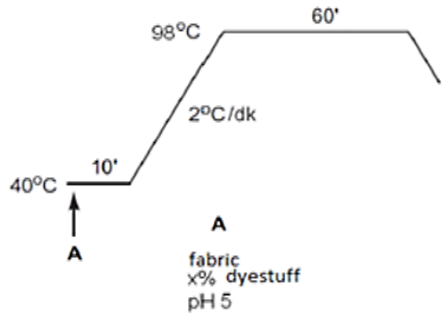

Figure 3. Dyeing of polyamide 6,6 with halochromic dyes

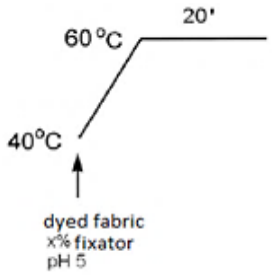

Figure 4. Post-treatment with fixator to dyed fabrics

Conventional dyeing is an inexpensive and simple method in bringing the halochromic properties to textile materials. Dyeing was carried out as shown in Figure 3 at a liquor ratio of 1:20 in the laboratory-type sample dyeing machine. The dyed fabrics were rinsed under running water for 10 minutes. Dyeing processes was performed on the fabrics at different dye concentrations.

After the dyeing process, clean bath was taken, and two different processes were applied as shown in Figure 4 at 60 °C for 20 minutes at 1:20 liquor ratio.

After dyeing with Alizarin Red S dye was completed, four fixators and tannic acid were added to improve the wet fastnesses of the dyed samples.

3. Results and Discussion

The hypsochromic and bathochromic shifts occur in the halochromic dyes.

Acetic acid, sodium hydroxide and hydrochloric acid were used for the production of hyposochromic and batochromic shifts of the Alizarin Red S dye used in this study.

3.1 UV-Visible Study

UV spectra of Alizarin Red S in aqueous solution (pH 7) exhibit one major absorption band in the region 300-700nm. One band is the result of n- π^* transition owing to the presence of the first group, which is not bonded by the intramolecular hydrogen bond.

A spectacular change occurred showing a red shift in the wavelength from 380 to 580 nm in aqueous medium even at the smallest value of sodium hydroxide was added into dye solution as shown in Figure 5.

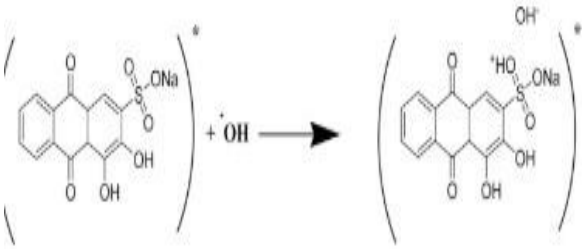

Figure 5. The addition mechanism of sodium hydroxide Alizarin Red S

3.2 The effect of post-treatment with anionic fixator and tannic acid on the color values

The effects of post-treating with anionic fixators and tannic acid on color coordinates of L* and b* were shown in Figures 6, 7, 8 and 9.

It can be observed in Figures 6 and 7 that the color became darker for samples dyed with Alizarin Red S after the application of anionic fixators. The darker in color is above the specified limits. The use of anionic fixators darkens the color. The color brightness increased as the fixator concentration increased. The largest color changes were obtained at a concentration of 3% Setafix S fixator. Color was shifted to yellow.

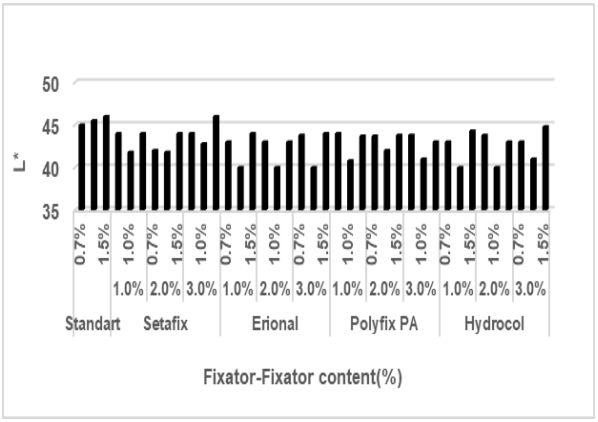

Figure 6. L* values of the standard Alizarin Red S dyed fabrics after post-treated with anionic fixators

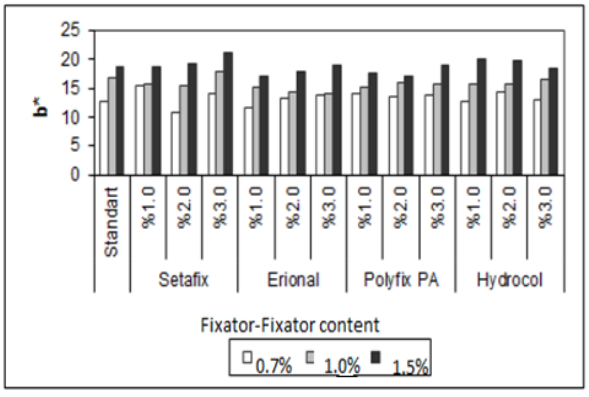

Figure 7. b* values of the standard Alizarin Red S dyed fabrics after post-treated with anionic fixators

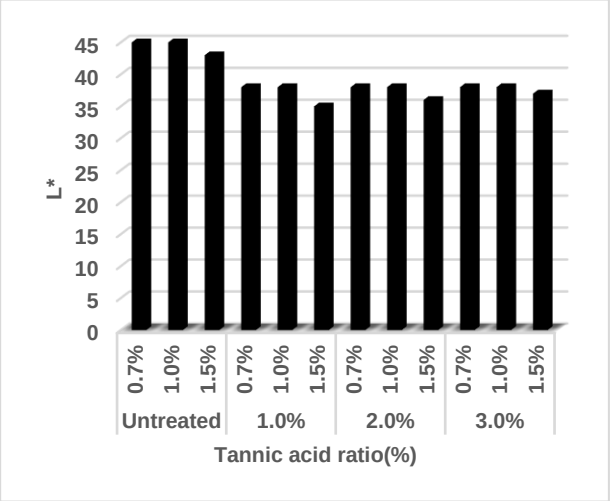

Figure 8. L* values of the standard Alizarin Red S dyed fabrics after post-treated with tannic acid

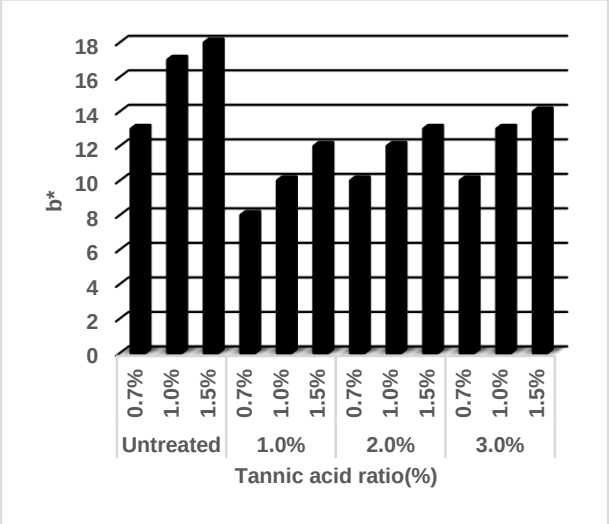

Figure 9. b*values of the standard Alizarin Red S dyed fabrics after post-treated with tannic acid

It can be seen in Figures 8 and 9 that the color became darker and reddish after dyeing with Alizarin Red S and post-treated with tannic acid.

3.3 The effect of post-treatment with anionic fixator and tannic acid on the color yield

The effects of post-treating with anionic fixators and tannic acid on the color yield were shown in Figures 10 and 11.

As given in Figure 10, it was determined that amount of fixator (%) has an effect on color yield for samples dyed with Alizarin Red S and post-treated with anionic fixator. Since the amount of fixator (%) increased, the color yield decreased. As the color intensity increased, the amount of fixator affected the color more. Maximum color yield for applied anionic fixators was obtained at 1.0% dyeing concentration.

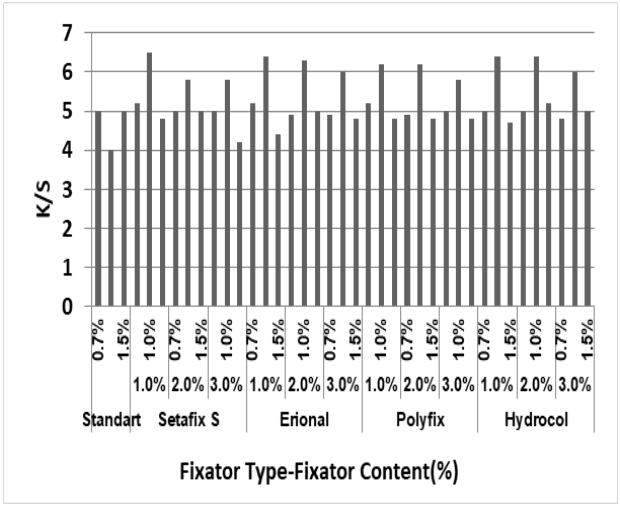

Figure 10. Effect of fixator type, amount and dyeing concentration on color yield in polyamide 6.6 fabric dyed with Alizarin Red S

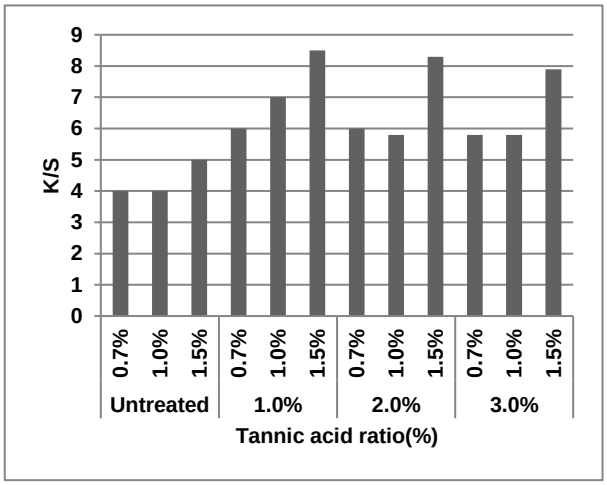

Figure 11. Effect of tannic acid ratio on color yield in polyamide 6.6 fabric dyed with Alizarin Red S

3.4 The effect of post-treating with fixator and tannic acid on rubbing, water and washing fastness

Wash fastness values of fabrics dyed with Alizarin Red S and treated with anionic fixators are given in Table 1. When wash fastness were examined, two replicates were made from each sample. The average of the results of these two repetitions were considered. Washing fastness values of fabrics dyed with Alizarin Red S and treated with tannic acid are given in Table 2.

The use of tannic acid in samples dyed with Alizarin Red S positively affected the color change values.

It can be seen in Table 3 that water fastness of fabrics dyed with Alizarin Red S and treated with anionic fixators increased.

3.5 Effects of post-treatment on color changes

Selected fabrics were immersed in nine different solutions prepared with HCl and NaOH between pH 2-13 and color change was observed after 1 hour (Figure 12).

Table 1. Wash fastness of fabrics dyed with Alizarin Red S and treated with anionic fixators

Dyestuff Ratio	Type of Fixator	Amount of Fixator	Microfiber Washing Fastness						Color Change
			wo	pac	pe	pa	co	cv	
	Reference		5	5	5	5	5	5	1/2
0.7%	Setafix S	1%	5	5	5	5	5	5	2
		2%	5	5	5	5	5	5	2
		3%	5	5	5	4/5	5	5	2/3
	Erional FRN	1%	5	5	5	4/5	5	5	1/2
		2%	5	5	5	4/5	5	5	2/3
		3%	5	5	5	5	5	5	2
	Polyfix PA	1%	5	5	5	5	5	5	2
		2%	5	5	5	5	5	5	1/2
		3%	5	5	5	5	5	5	2/3
	Hydrocol APR	1%	5	5	5	5	5	5	2/3
		2%	5	5	5	5	5	5	2
		3%	5	5	5	5	5	5	2/3
1%	Setafix S	1%	5	5	5	5	5	5	2/3
		2%	5	5	5	5	5	5	2/3
		3%	5	5	5	5	5	5	2/3
	Erional FRN	1%	5	5	5	5	5	5	2/3
		2%	5	5	5	5	5	5	2
		3%	5	5	5	5	5	5	2/3
	Polyfix PA	1%	5	5	5	5	5	5	2/3
		2%	5	5	5	5	5	5	2
		3%	5	5	5	5	5	5	2/3
	Hydrocol APR	1%	5	5	5	5	5	5	3
		2%	5	5	5	5	5	5	2
		3%	5	5	5	5	5	5	2/3
1.5%	Setafix S	1%	5	5	5	5	5	5	2/3
		2%	5	5	5	4/5	5	5	2/3
		3%	5	5	5	5	5	5	2
	Erional FRN	1%	5	5	5	4/5	5	5	2
		2%	5	5	5	5	5	5	2
		3%	5	5	5	5	5	5	2
	Polyfix PA	1%	5	5	5	5	5	5	2
		2%	5	5	5	5	5	5	2
		3%	5	5	5	5	5	5	2/3
	Hydrocol APR	1%	5	5	5	5	5	5	2
		2%	5	5	5	5	5	5	2
		3%	5	5	5	5	5	5	2/3

Table 2. Wash fastness of dyed with Alizarin Red S and post-treated with tannic acid

Dyestuff Ratio	Tannic acid ratio	Multifiber Wash Fastness						Color Change
		wo	pac	pes	pa	co	cv	
0.7%	untreatment	5	5	5	5	5	5	1/2
	1%	5	5	5	5	5	5	2
	2%	5	5	5	5	5	5	2/3
	3%	5	5	5	5	5	5	2/3
1.0%	untreatment	5	5	5	5	5	5	1/2
	1%	5	5	5	5	5	5	2/3
	2%	5	5	5	5	5	5	3
	3%	5	5	5	4/5	5	5	1/2
1.5%	untreatment	5	5	5	5	5	5	2
	1%	5	5	5	4/5	5	5	4
	2%	5	5	5	4/5	5	5	1/2
	3%	5	5	5	5	5	5	4

Table 3. Water and rubbing fastness of fabrics dyed with Alizarin Red S and post-treated with fixators

Dyestuff Ratio	Fixator Type	Fixator Contents	Water Fastness		Rubbing Fastness	
			PA	WO	Dry	Wet
0.7%	Reference		2/3	2	5	4/5
	Setafix S	1%	3/4	3/4	5	4/5
		2%	4	4	5	4/5
		3%	4/5	4/5	5	4/5
	Erional FRN	1%	3/4	2/3	5	4/5
		2%	4	3/4	5	4/5
		3%	4	3/4	5	4/5
	Polyfix PA	1%	3	2/3	5	4/5
		2%	4	3	5	4/5
		3%	4	3	5	4/5
	Hydrocol APR	1%	3	3	5	4/5
		2%	3	3/4	5	4/5
		3%	4	4	5	4/5
1%	Reference		2	2	5	4
	Setafix S	1%	3	3/4	5	4/5
		2%	4/5	4	5	4/5
		3%	4	4/5	5	4/5
	Erional FRN	1%	3	2/3	5	4
		2%	3	3/4	5	4/5
		3%	2/3	2/3	5	4/5
	Polyfix PA	1%	2/3	2/3	5	4/5
		2%	4	4	5	4/5
		3%	3/4	4	5	4/5
	Hydrocol APR	1%	2/3	2/3	5	4/5
		2%	4	3/4	5	4/5
		3%	4	4	5	4/5
1.5%	Reference		½	½	5	4
	Setafix S	1%	3/4	3	5	4/5
		2%	4	3/4	5	4/5
		3%	4	4	5	4/5
	Erional FRN	1%	3	2/3	5	4/5
		2%	3/4	3	5	4/5
		3%	3/4	3/4	5	4/5
	Polyfix PA	1%	3	2/3	5	4/5
		2%	4	3	5	4/5
		3%	4	3	5	4/5
	Hydrocol APR	1%	3	2/3	5	4/5
		2%	3/4	3	5	4/5
		3%	4	3/4	5	4/5

3.6. Surface Treatment

The functionality of the color alteration of halochromic dyes in polyamide 6,6 is often realized by surface treatment, such as dyeing.

Polyamide 6,6 fabric dyed with the pH - sensitive dye Alizarin Red S altered color from yellow to red in the range of 3,7-5,2 pH. Thus, compared with the solution, only a slight broadening was found. However, the acidic wavelength displayed a bathochromic shift of maximum 15nm with showing the influence of the dye and fibre coactions [21]. Figure 13 shows the results.

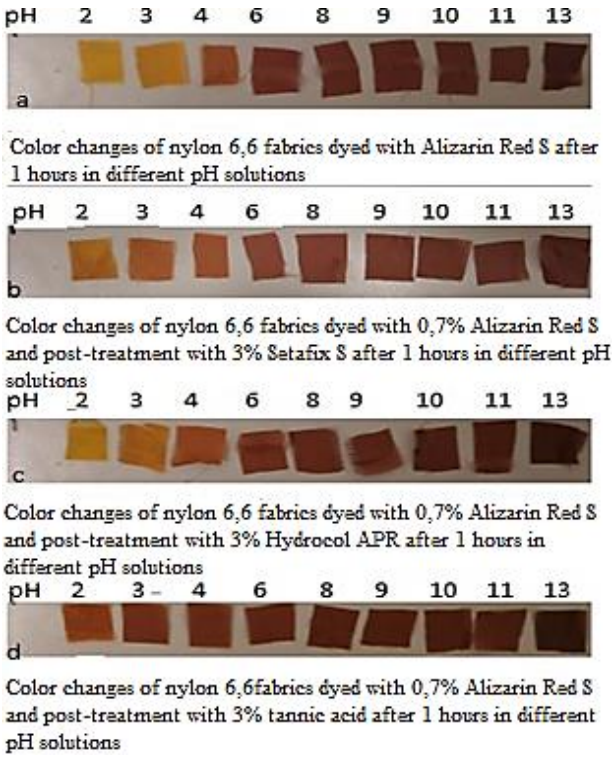

Figure 12. Color changes of nylon 6,6 fabrics dyed with Alizarin Red S and post-treated with two different fixators and tannic acid after 1 hour in different pH solutions.

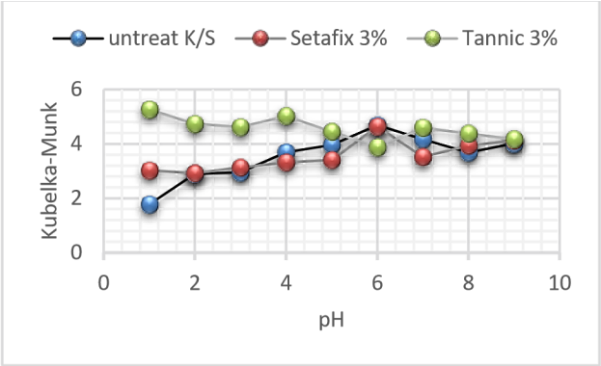

Figure 13. Normalized Kubelka-Munk values of Alizarin Red S in polyamide 6,6 as a function of pH at the absorbance maxima 440 and 520 nm

Polyamide 6,6 fabric dyed with the pH-sensitive dye Alizarin Red S altered color from yellow to red in the range of 3,7-5.2 pH. Thus, compared with the solution, only a slight broadening was found. However, the acidic wavelength displayed a bathochromic shift of maximum 15 nm with showing the influence of the dye and fibre coactions [21]. Figure 13 shows the results.

4. Conclusions

While it was obtained fine results in the water fastnesses, there was no significant effect on the rubbing fastness of the post-treatment with fixators. The best results were obtained with Setafix S fixator. Water fastness of fabrics dyed at low dye concentration and post-treated with tannic acid was well. It has been found that the use of tannic acid had no significant effect on improving of the rub fastness. It has been determined that wash fastness of fabrics dyed with Alizarin Red S and post-treated with tannic acid had not a significant effect. It has been determined that the use of tannic acid reduced color change. The use of a fixator is more appropriate because the color change must be fast and clear.

Acknowledgement

This study was supported by Namık Kemal University, Department of Textile Engineering, Turkey under Research Project (Project no: NKUBAP.00.17.YL.13.04).

References

1. Zollinger, H., *Color chemistry: syntheses, properties, and applications of organic dyes and pigments.* 2003, Switzerland: VHCA and Wiley-VCH, Inc.
2. Kim, S.H., editor. 2006, *Functional dyes*. Elsevier.
3. Bamfield, P. and Hutchings M.G., *Chromic phenomena: technological applications of colour chemistry.* 2010, UK: Royal Society of Chemistry.
4. Kirschning, A., Monenschein, H. and Wittenberg, R., *Functionalized polymers—emerging versatile tools for solution-phase chemistry and automated parallel synthesis.* Angewandte Chemie International Edition, 2001. **40**(4): p. 650-679.
5. Vancoillie G., Pelz S., Holder E., Hoogenboom R., *Direct nitroxide mediated (co) polymerization of 4-vinylphenylboronic acid as route towards sugar sensors.* Polymer Chemistry, 2012. **3**(7): p. 1726-1729.
6. Pietsch, C., Schubert, U.S., and Hoogenboom, R., *Aqueous polymeric sensors based on temperature-induced polymer phase transitions and solvatochromic dyes.* Chemical Communications, 2011. **47**(31): p. 8750-8765.
7. Fournier, D. and Du Prez, F., *"Click" chemistry as a promising tool for side-chain functionalization of polyurethanes.* Macromolecules, 2008. **41**(13): p. 4622-4630.
8. Roy, D., Cambre, J.N. and Sumerlin, B.S., *Future perspectives and recent advances in stimuli-responsive materials.* Progress in Polymer Science, 2010. **35**(1-2), p. 278-301.
9. De Meyer, T., Hemelsoet, K., Van der Schueren, L., Pauwels, E., De Clerck, K., Van Speybroeck, V., *Investigating the halochromic properties of azo dyes in an aqueous environment by using a combined experimental and theoretical approach.* Chemistry–A European Journal, 2012. **18**(26): p. 8120-8129.
10. Makedonski, P., Brandes, M., Grahn, W., Kowalsky, W., Wichern, J., Wiese, S., & Johannes, H.H., *Synthesis of new kinds of reactive azo dyes and their application for fibre-optical pH-measurements.* Dyes and Pigments, 2004. **61**(2): p. 109-119.
11. Trupp, S., Alberti, M., Carofiglio, T., Lubian, E., Lehmann, H., Heuermann, R., Yacoub-George, E., Bock, K., and Mohr, G.J., *Development of pH-sensitive indicator dyes for the preparation of micro-patterned optical sensor layers.* Sensors and Actuators B: Chemical, 2010. **150**(1), p. 206-210.
12. Kuwabara, T., Nakajima, H., Nanasawa, M. and Ueno, A., *Color change indicators for molecules using methyl red-modified cyclodextrins.* Analytical Chemistry, 1999.

71(14): p. 2844-2849.

13. Van der Schueren, L. and De Clerck, K., *The use of pH-indicator dyes for pH-sensitive textile materials.* Textile research journal, 2010. **80**(7): p. 590-603.
14. De Meyer, T., Hemelsoet, K., Van der Schueren, L., Pauwels, E., De Clerck, K. and Van Speybroeck, V., *Investigating the halochromic properties of azo dyes in an aqueous environment by using a combined experimental and theoretical approach.* Chemistry–A European Journal, 2012. **18**(26): p. 8120-8129.
15. De Meyer, T., Hemelsoet, K., Van Speybroeck, V. and De Clerck, K., Substituent effects on absorption spectra of pH indicators: An experimental and computational study of sulfonphthaleine dyes. Dyes and Pigments, 2014. **102**: p. 241-250.
16. Bouas-Laurent, H. and Dürr, H., *Organic photochromism (IUPAC technical report).* Pure and Applied Chemistry, 2001. **73**(4): p. 639-665.
17. Schueren, L.V. and Clerck, K.D., *The Use of pH-indicator Dyes for pH-sensitive Textile Materials.* Textile Research Journal, 2010. **80**(7): p. 590-603.
18. Staneva, D. and Betcheva, R., *Synthesis and Functional Properties of New Optical pH Sensor Based on Benzo [de]anthracen-7-one Immobilized on the Viscose*. Dyes and Pigments, 2007. **74**(1): p. 148-153.
19. De Meyer, T., Steyaert, I., Hemelsoet, K., Hoogenboom, R., Van Speybroeck, V. and De Clerck, K., *Halochromic properties of sulfonphthaleine dyes in a textile environment: The influence of substituents.* Dyes and Pigments, 2016. **124**: p. 249-257.
20. Gautam, R.K., Gautam, P.K., Chattopadhyaya, M.C. and Pandey, J.D., *Adsorption of Alizarin Red S onto biosorbent of Lantana camara: kinetic, equilibrium modeling and thermodynamic studies.* Proceedings of the National Academy of Sciences, India Section A: Physical Sciences, 2014. **84**(4): p. 495-504.
21. Van der Schueren, L. and De Clerck, K., *Coloration and application of pH-sensitive dyes on textile materials*. Coloration Technology, 2012. **128**(2): p. 82-90.

Available online at www.dergipark.gov.tr

INTERNATIONAL ADVANCED RESEARCHES
and
ENGINEERING JOURNAL

Journal homepage: www.dergipark.gov.tr/iarej

e-ISSN: 2618-575X

International Open Access

Volume 03
Issue 03

December, 2019

Research Article

Investigation on the corrosion resistances of bronze-waste tire-concrete composites

Tuba Bahtli [a,*] ***and Nesibe Sevde Ozbay*** [b]

[a]*Engineering and Architecture Faculty, Department of Metallurgical and Materials Engineering, Necmettin Erbakan University, Konya 42140, Turkey*
[b]*Institute of Science and Technology, Department of Mechanical Engineering, Department of Metallurgical and Materials Engineering, Necmettin Erbakan University, Konya 42140, Turkey*

ARTICLE INFO

Article history:
Received 08 October 2019
Revised 18 October 2019
Accepted 06 November 2019

Keywords:
Bronze sawdust
Composite
Concrete
Corrosion
Waste tire

ABSTRACT

In this study, finely ground CuAl10Ni bronze sawdust and waste tire additives were incorporated into C30 concrete at different amounts and then their corrosion resistances were investigated. SEM/EDX analyses were performed. It was observed that after acids attacks, as the waiting time in the acid solutions increased, electrical surface resistance values increased due to further corrosion. Also, more losses in the weight were observed in the pure concrete than the concretes including bronze sawdust and waste tire grains, then those refractories showed higher corrosion resistances than that of pure concrete.

1. Introduction

Corrosion is an important parameter for the service life of reinforced concrete structures limited by corrosion deterioration [1]. There have been many academic researches on concrete corrosion. In the study of Congqi Fang et al., it was observed that flat steel bar reinforced concrete, which was kept in 5% NaCl solution for 3 days after curing, was more corroded than the concrete having deformed steel bar. Corrosion degree increased with increasing corrosion time, and also the concretes coated with polyethylene material were less corroded [2]. Similarly, concretes with coated steel reinforcement were less corroded. In addition, it was stated that the degree of corrosion had a significant effect on the bond that decreased with increasing corrosion degree according to Cabrera's study [3]. Guerrero et al. produced the geopolymeric concrete product coated with metakaolin and fly ash for 3, 7 and 28 days. As a result of this study, metakaolin coated concrete had a higher compressive strength and gel polymeric coating exhibited better adhesion than that of hybrid polymer coating. It was concluded that geopolymer material (as a protective coating) showed a much better chlorine permeability resistance than that of uncoated concrete material [4].

Corrosion of reinforcement is the predominant factor causing deterioration of concrete construction, especially located in the marine environment. Chloride ions and carbon dioxide penetrations are the most important causes of corrosion initiation of reinforcing steel. After initiation of the corrosion process, the corrosion products are usually deposited in the concrete around the steel. Then expansive stresses formation occurs cracking the concrete cover [5, 6].

In the study of Thomas et al., the chloride penetrations of concretes in which crumb rubber was replaced up to 7.5% of fine aggregates were lesser than or equal with the value of their control concrete. Also, more losses in the weight and compressive strength were observed in their control concrete than the rubberized concrete after acid attack [7].

In the present study of Oikonomou et al., physical and mechanical properties of cement mortars modified with worn tires from automobiles have been investigated. The reduction in chloride ion penetration in cement mortars and in concrete reduces the potential for corrosion of embedded reinforcement [8].

The aim of this study is to investigate for the use of bronze sawdust and waste tire additives in order to improve corrosion resistances of C30 concrete materials.

* Corresponding author. Tel.: +90-332-325-2024.
E-mail addresses: taksoy@erbakan.edu.tr *(T. Bahtli)*, nesibesevde@hotmail.com *(N.S. Ozbay)*
ORCID: 0000-0001-5682-6280 *(T. Bahtli)*, 0000-0002-0071-8464 *(N.S. Ozbay)*
DOI: 10.35860/iarej.630895

2. Materials and Methods

New concrete materials with different compositions were produced by using bronze waste and fine rubber waste: i) 2.5 wt.% bronze waste and 2.5 wt.% waste tire (2.5%B+2.5%T); and ii) 5 wt.% bronze and 5 wt.% waste tire were added to C30 concrete (5%B+5%T). Ready-mixed dry mortar of C30 concrete was used. After the produced samples were removed from the mold, were kept in water for 28 days for curing.

Corrosion tests were performed according to ASTM C-1152. Three different acid solutions with pH 1.5-2 were prepared by using HCl, H_2SO_4 and HNO_3 acids. Samples from each composition were stored in three different acid solutions for 7 and 28 days. After 7 days, the samples were removed and their electrical resistances were measured. Then the samples were dried and weighed. Same procedures were applied for the samples which were held for 28 days. After corrosion test had completed, microstructure investigations were performed by scanning electron microscopy (SEM) at 1000x magnification with backscattered electron images.

3. Results and Discussion

3.1 Corrosion Test Results

According to corrosion tests results with 3 different acids, for all concrete samples either with or without additives, it has been found that 3 acid types had approximately the same effect weight loss in concretes.

Dissolution and weight losses occurred in pure concrete samples after corrosion tests. In the concrete samples where bronze and tire were used together, it was found that the weight losses were not significant for the corrosion tests performed within 3 acids, also close to the pre-corrosion values and even increased slightly. It was considered that these concrete materials had higher corrosion resistances compared to pure concrete (Table 1).

Similar results of our study were achieved in the study of Blessen Skariah Thomas et al. After acid attack, more losses in the weight were observed in their control mix concrete than the rubberized concrete [7].

As a result of corrosion tests performed with 3 different acids, it was seen that the electrical surface resistance values of all concrete samples increased (Table 2). Ceramics are non-conductive materials and show electrical surface resistance. Metal reinforcements are materials which are electrically conductive but begin to show resistance after corrosion. Then, structural defects caused by corrosion effect in pure concrete (ceramic matrix) and rusting of metallic reinforcement (bronze) in the doped concrete materials caused the increase of electrical surface resistances. Similar to our results, Yung et al. found that the electrical resistance increased as more waste tire rubber powder was added [9].

The increase in resistance means that the metal reinforcement is corroded. According to the resistance results, similar to the weight losses, 3 strong acids have approximately the same corrosion effect. As the waiting time in the acid solutions increased, electrical surface resistance values increased due to further corrosion.

which contained porosity, microcracks and also deep cracks.

According to the elemental analysis, the distributions of Cu, Al, Ni elements were in the same regions and it was seen that the grains were bronze.

According to the microstructure and elemental analysis of the concrete sample containing 2.5% bronze and 2.5% waste tire, which were tested for corrosion in HCl solution for 28 days (Figure 2), the oxygen distribution was in the region where the bronze grains were found. Then, it was thought that bronze grains were oxidized, new phase formation occurred. Waste tire grains could also absorb some acid solutions. These situations were thought to be effective in weight gain (Table 1).

Table 1. Dry weights of samples that were stored in acid solutions with pH 2 for 7 and 28 days

Acid Solution Type	Material	Dry weights before corrosion test (g)	Dry weights after corrosion test for 7 days (g)	Weight change after corrosion test for 7 days (%)	Dry weights after corrosion test for 28 days (g)	Weight change after corrosion test for 28 days (%)
HCl solution	Pure	302.63	291.56	-3.65793	291.83	-3.56871
	2.5%B+2.5%T	298.42	299.64	0.509349	299.97	0.284833
	5%B+5%T	287.97	288.73	0.263916	289.16	0.239608
H_2SO_4 solution	Pure	304.01	292.95	-3.63804	293.75	-3.37489
	2.5%B+2.5%T	292.32	293.65	0.454981	293.98	0.465244
	5%B+5%T	283.20	283.65	0.158898	283.99	0.173023
HNO_3 solution	Pure	301.24	291.06	-3.37937	292.82	-2.79511
	2.5%B+2.5%T	293.17	294.81	0.24218	294.86	0.235358
	5%B+5%T	277.80	278.70	-0.036	278.87	0.025198

Table 2. Electrical surface resistances of samples kept in pure water and acid solutions

Sample	After soaking in pure water (kΩcm)	After corrosion test for 7 days (kΩcm)			After corrosion test for 28 days (kΩcm)		
		HCl	H_2SO_4	HNO_3	HCl	H_2SO_4	HNO_3
Pure	51.5	140	135.5	126	346	265	160
2.5%B+2.5%T	128	160	174	183	172	196	190
5%B+5%T	175	214	212	201	230	228	215

Similarly, since the Cl ions were in the regions where both the concrete matrix and the Cu element were present, it was thought that the concrete matrix and the bronze reinforcement were affected by the HCl acid solution and that the corrosion type known as bronze cancer occurred (Figure 3).

3.2 SEM Analysis of Concretes Before and After Corrosion Tests

Before corrosion test, according to SEM images of 2.5%B+2.5%T concrete (Figure 1), it was observed that there was no strong bonding between the concrete matrix, bronze and waste tire interfaces in the concrete structure

According to study of Dermaj et al., similar to our results given as above, bronzes are subjected to corrosion, which results in the formation of an oxide or salt layer (Cl in our study) on its surface. The corrosion products formed on bronze surface acquire the barrier property preventing acomplete destruction of the object [10].

When EDX analysis (Table 3) were examined, it was seen that before corrosion test, besides the Ca, Si, Al elements, which are mainly in the cement phase, Cu, Al, Ni elements forming the bronze material increased and the percentage of C increased with increasing the amount of waste tire.

After corrosion tests, the decrease in Ca and Si amounts indicated the dissolution of the concrete matrix. According to results of corrosion test in HCl solution, the amount of Cu decreased slightly from the pre-corrosion value suggested that the oxidation could be passive oxidation (protective oxide layer on the surface). The fact that the resistance values did not increase too much confirmed this situation.

According to the EDX analysis of corrosion test, where H_2SO_4 solution was used, as the amount of Cu did not decrease, passive oxidation could be the same as in HCl solution.

Also, it was seen that the amount of C and O increased. It was thought that tire reinforcements were not affected by acid unlike the concrete matrix.

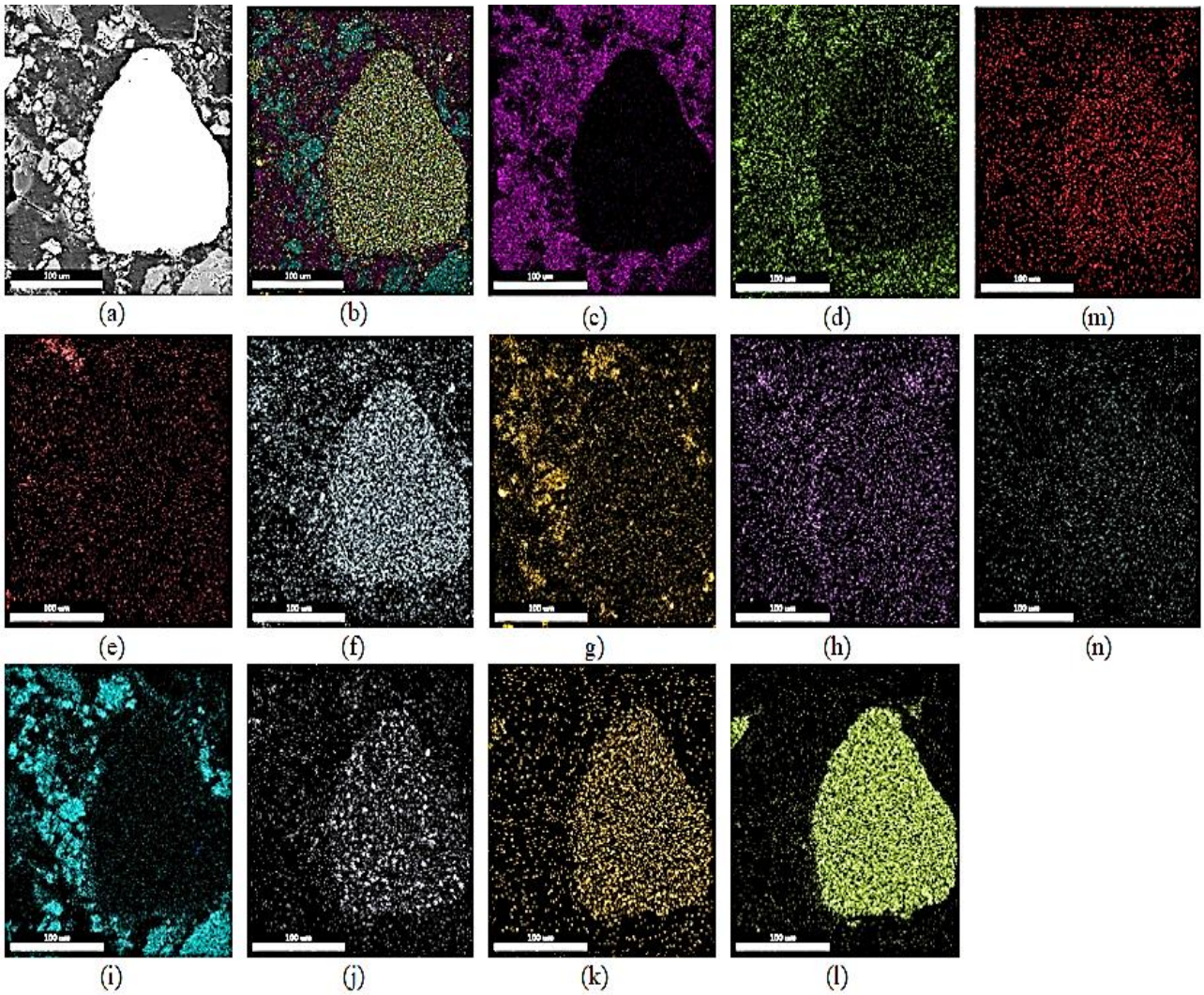

Figure 1. Before corrosion test in HCl solution, a) Microstructure, b) Colored microstructure of 2.5%B+2.5%T concrete and distribution of elements: c) C, d) O, e) Na, f) Mg, g) Al, h) Si, i) S, j) K, k) Ca, l) Fe, m) Ni, n) Cu (1000X-SEM backscattered electron image).

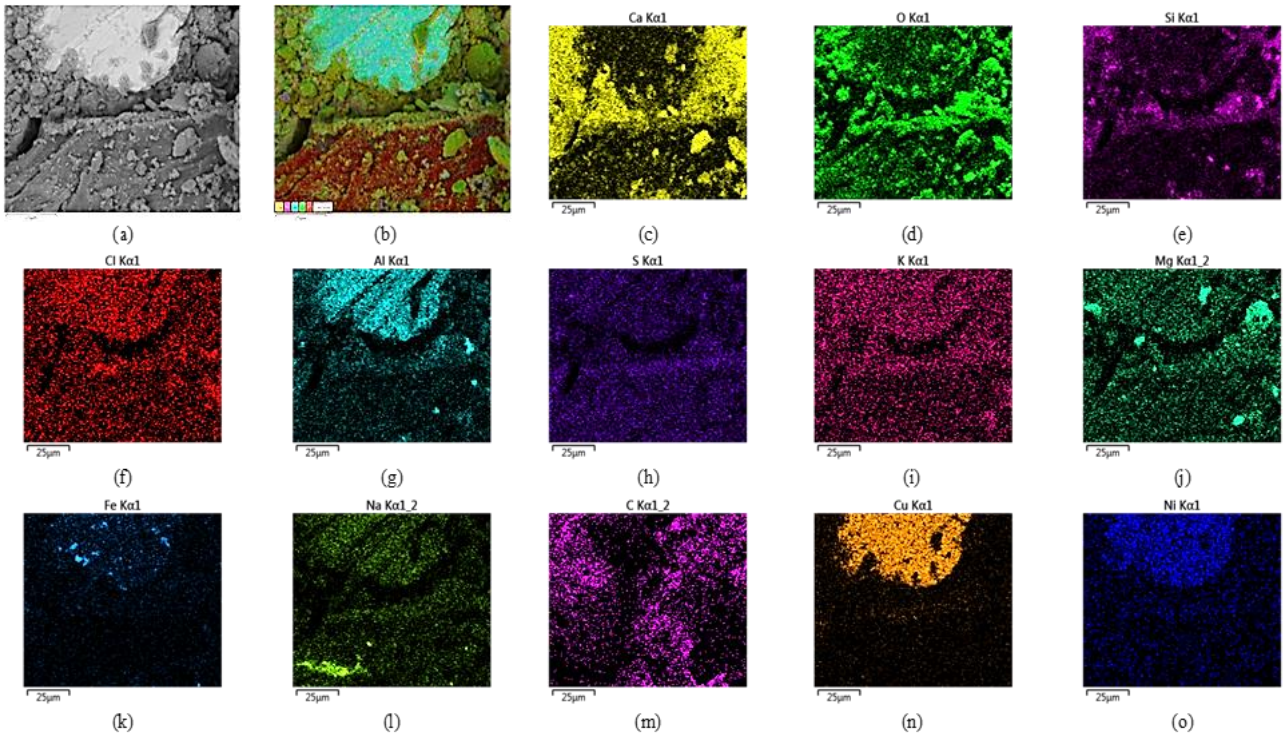

Figure 2. After corrosion test in HCl solution, a) Microstructure, b) Colored microstructure of 2.5%B+2.5%T concrete and distribution of elements: c) Ca, d) O, e) Si, f) Cl, g) Al, h) S, i) K, j) Mg, k) Fe, l) Na, m) C, n) Cu, o) Ni (1000X-SEM back scattered electron image).

Table 3. EDX analysis after corrosion tests of bronze and tire doped concrete samples

Elements (%)	2.5%B+2.5%T		
	Before corrosion test	After corrosion test in HCl solution	After corrosion test in H_2SO_4 solution
C	**7**	**54.32**	**33.75**
O	**8**	**27.51**	**28.18**
Na	1	0.42	0.18
Mg	2	0.58	0.60
Al	6	**1.34**	**1.80**
Si	**12**	**1.12**	**3.55**
S	4	0.00	0.00
K	2	0.18	0.30
Ca	**46**	**6.64**	**17.00**
Fe	3	0.59	2.18
Ni	1	**0.45**	**1.11**
Cu	**8**	**6.78**	**11.34**
Cl	0	0.07	0

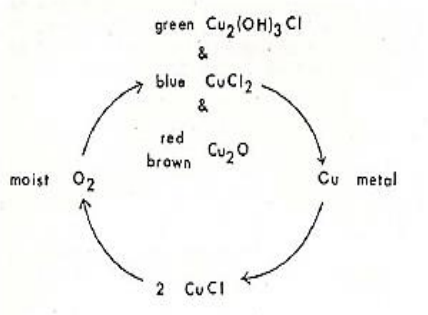

Figure 3. Schematic depiction of the cyclic nature of bronze cancer.

In the process of bronze cancer (Figure 3), free chlorine ions in the environment reacts with ionizing copper ions such as below:

$$2Cu^{+} + 2Cl^{-} \rightarrow Cu_2Cl_2 \text{ or}$$
$$Cu^{+} + Cl^{-} \rightarrow CuCl \text{ (Nantokit)} \quad (1)$$
$$2Cu_2Cl_2 + ½O_2 \rightarrow Cu_2O + 2CuCl_2$$

Under humid and oxygenated environment:

$$2Cu_2Cl_2 + 4H_2O + O_2 \rightarrow CuCl_2.3Cu(OH)_2 + 2HCl \quad (2)$$
$$3Cu_2Cl_2 + 3/2O_2 + 3H_2O \rightarrow 2CuCl_2 + CuCl_2.3Cu(OH)_2$$

A portion of the copper chloride reacts with the additional copper in the alloy to form more copper chloride:

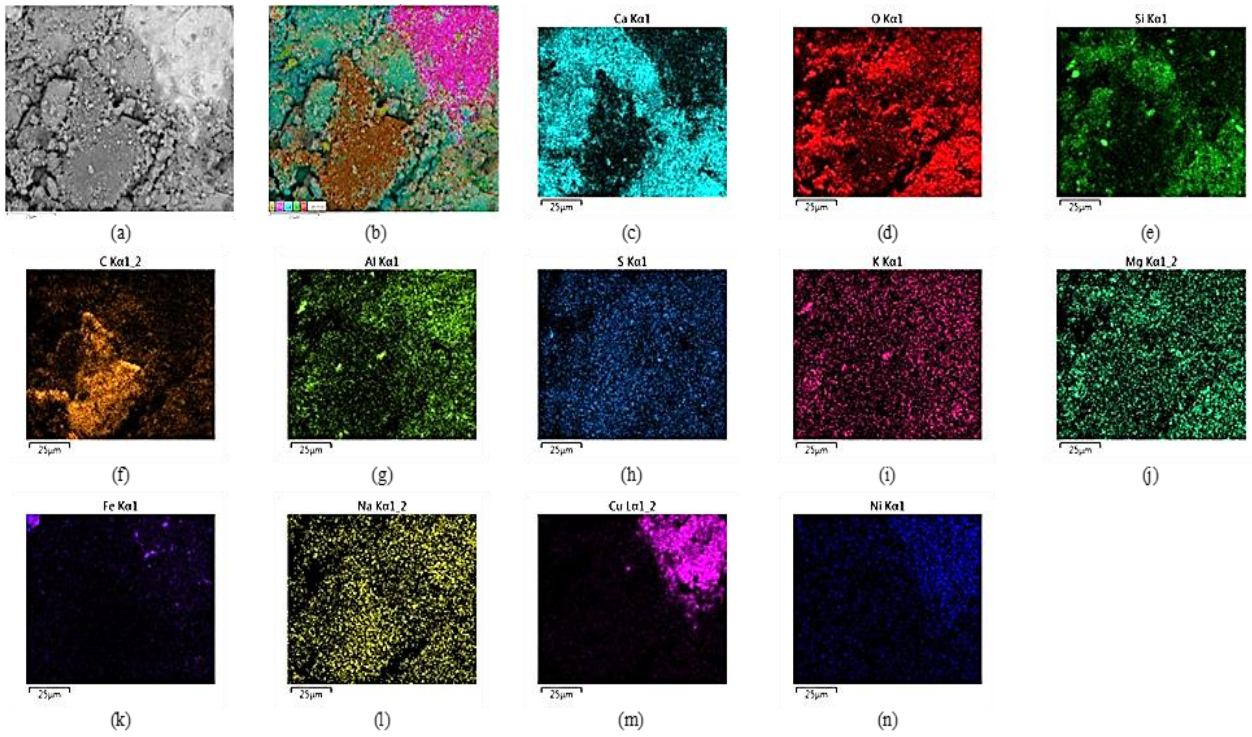

Figure 4. After corrosion test in H_2SO_4 solution, a) Microstructure, b) Colored microstructure of 2.5%B+2.5%T concrete and distribution of elements: c) Ca, d) O, e) Si, f) C, g) Al, h) S, i) K, j) Mg, k) Fe, l) Na, m) Cu, n) Ni (1000X-SEM back scattered electron image).

$$CuCl_2 + Cu \rightarrow Cu_2Cl_2 \quad (3)$$

The reaction sequence of the bronze disease process occurs repeatedly until all the copper and copper compounds in the alloy turn into waste [11].

When the SEM results of the concrete containing 2.5% bronze and 2.5% waste tire were tested for corrosion in H_2SO_4 solution (Figure 4), it was thought that bronze was oxidized due to the coincidence of the distribution regions of oxygen and Cu. However, the amount of Cu did not decrease, then passive oxidation could be on the surface of bronze grains.

4. Conclusions

After the corrosion tests carried out in different acid solutions of the concrete sample containing 2.5% bronze and 2.5% waste tire, it was seen that the amount of Ca and Si decreased considerably, and the amount of O increased. Also, Cu did not decrease much more than the pre-corrosion value. Electrical surface resistance values did not increase too much. Then it was thought that while the concrete matrix was affected by acid solutions, the rubber components were not affected. The corrosion called bronze cancer occurred on bronze grain surfaces at low levels. Those results showed that there was a lower level of corrosion in the concrete sample containing 2.5% bronze and 2.5% waste tire compared to pure concrete.

Acknowledgment

This work was supported by the Necmettin Erbakan University Scientific Research Projects under the project no: 171351001, Konya.

Nomenclature

B : Bronze

T : Waste tire

References

1. Liu, T., Weyers, W., *Modeling the Dynamic Corrosion Process in Chloride Contaminated Concrete Structures*. Cement and Concrete Research, 1998. **28**(3): p. 365-379.
2. Fang, C., Lundgrenb, K., Chena, L., Zhua, C., *Corrosion Influence on Bond in Reinforced Concrete*. Cement and Concrete Research, 2004. **34**: p. 2159–2167.
3. Cabrera, J. G., *Deterioration of Concrete Due to Reinforcement Steel Corrosion*. Cement & Concrete Composites, 1996. **18**: p. 47-59.
4. Guerrero, A. M. A., Robayo-Salazar, R. A., Mejía de Gutiérrez, R., *A Novel Geopolymer Application: Coatings to Protect Reinforced Concrete Against Corrosion*. Applied Clay Science, 2017. **135**: p. 437–446.
5. Elsener, B., Büchler, M., Stalder, F., Böhni H., *Migrating Corrosion Inhibitor Blend for Reinforced Concrete: Part 1—Prevention of Corrosion*. Corrosion,1999. **55**(12): p. 1155-1169.
6. Song, H.W., Saraswathy, V., *Corrosion Monitoring of Reinforced Concrete Structures – A Review*. International Journal of Electrochemical Science, 2007. **2**: p. 1- 28.
7. Thomas, B. S., Gupta, R. C., Panicker, V. J., *Recycling of waste tire rubber as aggregate in concrete:durability-related performance*. Journal of Cleaner Production, 2016. **112**(1): p. 504-513.
8. Oikonomou, N., Mavridou, S., *Improvement of chloride ion penetration resistance in cement mortars modifiedwith rubber from worn automobile tires*. Cement & Concrete Composites, 2009. **31**: p. 403–407.
9. Yung, W. H., Yung, L. C., Hua L. H., *A study of the*

durability properties of waste tire rubber appliedto self-compacting concrete. Construction and Building Materials, 2013. **41**: p. 665-672.

10. Dermaj, A., Hajjaji, N., Joiret, S. ,. Rahmouni, K., Srhiri, A., Takenouti, H., Vivier, V., *Electrochemical and spectroscopic evidences of corrosioninhibition of bronze by a triazole derivative.* Electrochimica Acta, 2007. **52**: p. 4654–4662.
11. Goffer, Z., *Archaeological Chemistry*, 2007, A John Wiley & Sons, Inc Publication, , p. 193-197.

Available online at www.dergipark.gov.tr

INTERNATIONAL ADVANCED RESEARCHES and ENGINEERING JOURNAL

Journal homepage: www.dergipark.gov.tr/iarej

e-ISSN: 2618-575X

International Open Access

Volume 03
Issue 03

December, 2019

Research Article

TEM characterization and synthesis of nanoparticle B_4C by high-energy milling

Hakan Gokmese [a,*], ***Bulent Bostan*** [b], ***Taha Alper Yilmaz*** [c] ***and Ufuk Tasci*** [d]

[a]*Necmettin Erbakan University, Faculty of Seydisehir Ahmet Cengiz Engineering, Konya, 42370, Turkey*
[b]*Gazi University, Faculty of Technology, Ankara, 06500, Turkey*
[c]*University of Atatürk, Faculty of Engineering, Metallurgical and Materials Engineering, Erzurum, 25240, Turkey*
[d]*University of Gazi, Technical Sciences Vocational School, Ankara, 06374, Turkey*

ARTICLE INFO

Article history:
Received 08 October 2019
Revised 24 October 2019
Accepted 05 November 2019

Keywords:
TEM
Diffraction pattern
B_4C
Nanoparticle
Synthesis

ABSTRACT

In this study, nanoparticle B_4C synthesis was carried out by high-energy milling. For this purpose, B_2O_3-C-Mg triple systems were used in the reaction stoichiometric ratios as starting materials in the experimental studies. The reduction process of B_2O_3 was performed using speks type milling device. The transformation of the ceramic phase of the nanoparticle B_4C by XRD analysis was examined. In terms of microstructural characterization of its powder shape and morphology, TEM (imaging and selected area diffraction pattern) investigations were conducted. The product synthesized by the leaching process was cleaned from MgO/B_4C impurities and the production of the nanoparticle B_4C was performed. After leaching processes, it was determined that some of the synthesized powders were below 50 nm, while others varied between the ranges of 50-350 nm. In TEM examinations of B_4C particles carried out after leaching process, it was seen that there were twin formations observed as planar error. Depending on the d values calculated by solving the TEM diffraction patterns, the planes represented by nano-sized B_4C particles were determined.

1. Introduction

It is said that the mechanochemical synthesis will be one of the most important methods in the future for the production of composite materials and it is becoming the focus of attention by the day [1]. Mechanochemical synthesis is a solid-state powder-material synthesis method involving chemical reactions at room temperature or lower temperatures following the mixture of reaction start powders [2].

The chemical reaction in question can be either during the mechanical alloying process or by the heat treatment of mechanically alloyed powders. In this process, metal powders are subjected to milling with a combination of metal powders and reactive elements to synthesize thermally stable compositions (metal oxides, nitrides, and carbides) in the presence of reactive solids or gases. These stable compositions are usually formed as a result of the in-situ reaction [1]. The increase in reaction kinetics during the high-energy milling process occurs through microstructural thinning, repeated cold deformation, and diffraction of particles [2].

When solid particles are micronized, their surface area increases in inverse proportion to the particle size. When the 1cm-sized particle is micronized to a scale of 1µm and 10nm, its specific surface area increases between 10,000 and 1,000,000. The increase in the specific surface area directly affects the dissolution and reaction rates of particles [3]. Most materials produced by mechanochemical synthesis can be produced with its shape having crystallized size on a scale of 1-10 nm. Nanoparticles can be used potentially due to their superior mechanical and physical properties, which allow for many structural applications. Due to the effect of nanoparticles available in the structure of nanostructured materials, their properties such as high hardness, fracture toughness and ductility at low temperatures make them advantageous compared to the equivalent materials in the microstructure. In terms of the development of the nanoparticle surface modifications after the milling process, the potential applications are going on [4].

In recent years, the widespread use of phase composites, which are especially intertwined with mechanochemical technique, together with nano-sized microstructures attracts

* Corresponding author. Tel.: +90-332-582-6000.
E-mail addresses: hakan1440@gmail.com *(H. Gokmese)*, bbostan@konya.edu.tr *(B. Bostan)*, tahaalperyilmaz@atauni.edu.tr *(T.A. Yilmaz)*, ufuktasci@gazi.edu.tr *(U. Tasci)*
ORCID: 0000-0002-5125-9720 *(H. Gokmese)*, 0000-0002-6114-875X *(B.Bostan)*, 0000-0002-4316-6890 *(T.A. Yilmaz)*, 0000-0002-8577-443X *(U.Tasci)*
DOI: 10.35860/iarej.630999

attention [2]. When Alumina's (Al_2O_3) thermal stability and mechanical properties at high temperatures are combined with Magnesium oxide's (MGO) high melting point (2800°C), compressive strength, hardness, and thermodynamic stability and boron carbide's (B_4C) high melting point, excellent rigidity, low specific gravity (2.52 g/cm^3), high elastic modulus, and chemical stability, the properties of the resulting material can be significantly improved [5-10].

Thus, in this study, the synthesizability of nanoparticle B_4C ceramic phase with the mechanochemical method by using B_2O_3-B_4C-C triple system was examined at room temperature. In addition, the powder shape and morphology of synthesized nanoparticle B_4C, the solution of diffraction patterns and determination of planes were identified by TEM.

2. Experiment

The initial components used for the production of nano-B_4C particles by mechanochemical synthesis, which constitute the first phase of experimental studies, were used in the studies in the form of B_2O_3, C and Mg initial powder components, respectively. In the studies, B_2O_3 powder (315μm) obtained from the Eti Mine Enterprise was used as a source of boron. The chemical properties of B_2O_3 powder are stated in Table 1. Carbon powder was used as the carbide-maker starting component and it was obtained from Aldrich Company. The properties of the used carbon powder are shown in Table 2. In order for the B_4C ceramic structure to be synthesized, Mg metal powders obtained from Aldrich Company and used as reactants were used in the studies for the purpose of the reduction of B_2O_3. The properties of Mg powders are also given in Table 3.

Table 1. Chemical properties of the boron oxide powder.

Content	Unit	Value
B_2O_3	%	98.00 min.
SO_4	ppm	500 max.
Cl	ppm	10 max.
Fe	ppm	15 max.

Table 2. Properties of carbon

Vapor pressure	Purity	Shape	Ignition temperature
< 0.1 mmHg (20°C)	99.95%	Powder, ball	842 °F
Specific resistance	Particle size	mp	Density
1375 μΩ-cm (20°C)	2-12 μm	3550 °C (lit.)	2.267 g/cm^3

Table 3. Properties of magnesium

Purity	Shape	Ignition temperature	Specific resistance
≥ 98 %	Powder	950 °F	4.46 μΩ-cm 20°C
Particle size	bp	mp	Density
75 - 200 μm	1090 °C (lit.)	648 °C (lit.)	1.74 g/cm^3

Table 4. Experiment parameters

Experiment	Starting Materials			Total Powder (g)	Reactions	
	B_2O_3	Mg	C			
1	1.074	0.833	0.092	2	$2B_2O_3 + 6Mg + C$ ==> $6MgO + B_4C$	
Milling Parameters (Speks)						Sample Code
Pot Volume (ml)	Ball Diameter (mm)	Ball Weight (g)	Ball Number (Pieces)	Powder / Ball Ratio	Rotation speed (rpm)	Time hours	
50	15.10.5	40	10	1/20	1200	4	S-Mg-3

For the production of nano boron carbide by mechanochemical synthesis, activation processes of B_2O_3, C and Mg powder material starting components were provided in the speks type-milling device. The experiment parameters used for this purpose are given in Table 4.

After the synthesis studies, leaching process (15% HCl) was applied to the powder material mixture in order to remove the impurities such as Fe and MgO which originated from the synthesis environment and the initial components used in the synthesis. Thus, it was aimed to transfer impurities into the prepared solution and to obtain the nano B_4C particles, which were intended to be produced, alone. Size analysis measurements of the synthesized nanoparticle powder mixtures by using speks type milling device were performed. For this purpose, size-analysis-measurements of powder before and after leaching were carried out with the device, which operated with Laser Doppler Electrophoresis technique and made particle measurement with Malvern-Nano-ZS model zeta potential. XRD analysis was performed for determination of the possible compounds in synthesized powder mixtures before and after leaching. XRD studies were conducted with Philips brand X-ray diffractometer device and by using 40kV voltage, 40mA current, and Cu-Kα radiation in the range of $10° < 2\theta < 70°$. Especially after leaching processes, JEOL JEM-1400 Transmission Electron Microscope (TEM) was used for nano-sized microstructural imaging. The images obtained in these studies were recorded with different enlargements having 100kV value and in the range of 500-100/1 in the digital environment. The formula given in the following equation was used for the indexing of the diffraction patterns of synthesized nano-dimensional B_4C particles.

$$d_{(hkl)} = (\lambda \times CL) / R \quad (1)$$

d = Distance between planes (Â), λ = Electron wavelength (Â), CL = Camera length (mm), R = Vectorial distance of the specified spot to the zero axis (mm).

d values were calculated using the equation given above which is also known as camera constant equation (d1, d2, d3 etc.). The d values given for various phases and compounds were examined and indexing of the patterns were performed in terms of the values belonging to the B_4C ceramic phase.

3. Results and Discussions

In speks studies, in terms of magnesiothermic reduction, 4 hours of synthesis was performed with B_2O_3, C and Mg starting components under the study parameters in Table 4 by using reactant Mg metal. XRD analysis of the obtained powder mixture is shown in Figure 1. It is observed that peak values occurring at the end of XRD analysis after 4 hours of synthesis define the initial metallic magnesium, Fe and MgO. Setoudeh et al. showed MGO/ZrB_2 synthesis with the mechanochemical method in ZrO_2, B_2O_3 and Mg ternary system by XRD analysis at the end of 2 hours. They explained that after 15 hours, the transformation began, and nanoparticle ceramic phases could be formed [11]. In the literature reviews conducted on mechanochemical synthesis, the attention is drawn to the type and amount of pollution present during synthesis. It is stated that the powder pollution may be due to the issues such as initial powder impurities, atmosphere, and milling equipment [12]. It can also be stated that this is due to the milling pot and the balls used in synthesizing studies, as well as powder pollution and by-products formed in the process.

It is seen that in XRD analysis after leaching proses, the obtained peak values define the B_4C ceramic phase (Figure 2). Deng et al. explained that in the MGO/B4C powder mixture, which they synthesized mechanochemically, MgO could be removed with a solution of 18% HCl and nanoparticle B_4C could be produced alone [13]. In another study, using XRD analysis, Sharifi and his colleagues showed that the B_4C nanoparticle, which was mechanochemically synthesized alone after leaching, showed similarity to the B_4C in commercial purity produced by the carbothermal method [14]. Thus, the synthesized nanoparticle B_4C ceramic material was also brought out after leaching processes. In addition, MGO and other chemicals with impurities such as Fe were moved to the prepared acid solution, and production of nanoparticle B_4C alone was performed.

The shape and morphological characterization of nanoparticle particles produced using mechanochemical synthesis method and attitudes they had in terms of diffraction pattern studies were revealed after the TEM examinations. After the preparation stages, the examinations were performed by taking the TEM sample on the formvar/carbon grid. In this context, to determine the microstructural behavior of the powder mixture during the TEM examinations, microstructural images from the grid slices on the grid at low magnifications (500) to the high magnifications (300,000) are given in Figure 3. When the microstructure images before the leaching process in Figure 3 are examined, we can say that the microstructure images (a, b) at the low magnification in the grid slice are appropriately dispersed in terms of the powder mixture that was mixed during the sample preparation. However, as it can be understood from microstructure images (e, f) at the high magnifications, intense agglomeration was detected in the powder particles.

From the general distribution of the powder mixture, which was mixed after the preparation phase of the TEM sample, their distribution emerging at high magnifications is shown in Figure 4 by microstructure images. When the general distributions of the powders before leaching and after they were mixed were compared, as shown in Figure 4, it was determined that the general distributions of the mixed powders were more suitable and smaller sizes. The most important element in occurring of this situation is the removal of impurities from the structure by leaching process and the ability to display the nanoparticle B_4C particles alone.

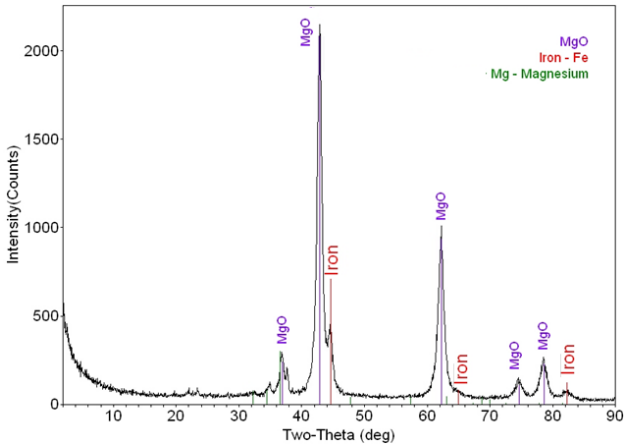

Figure 1. XRD analysis of the powder mixture synthesized for 4 hours (before leaching).

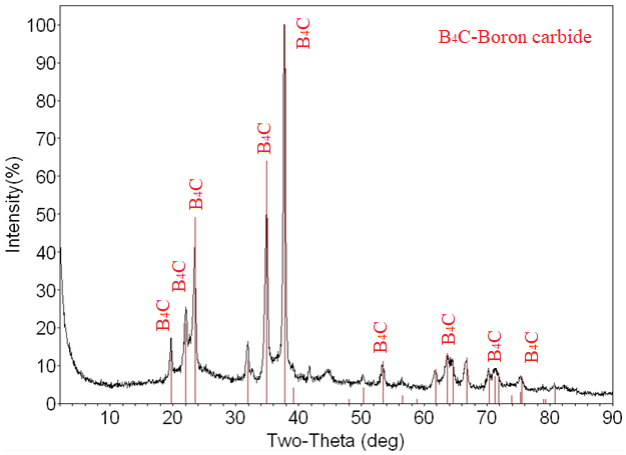

Figure 2. XRD analysis of the powder mixture synthesized for 4 hours (after leaching).

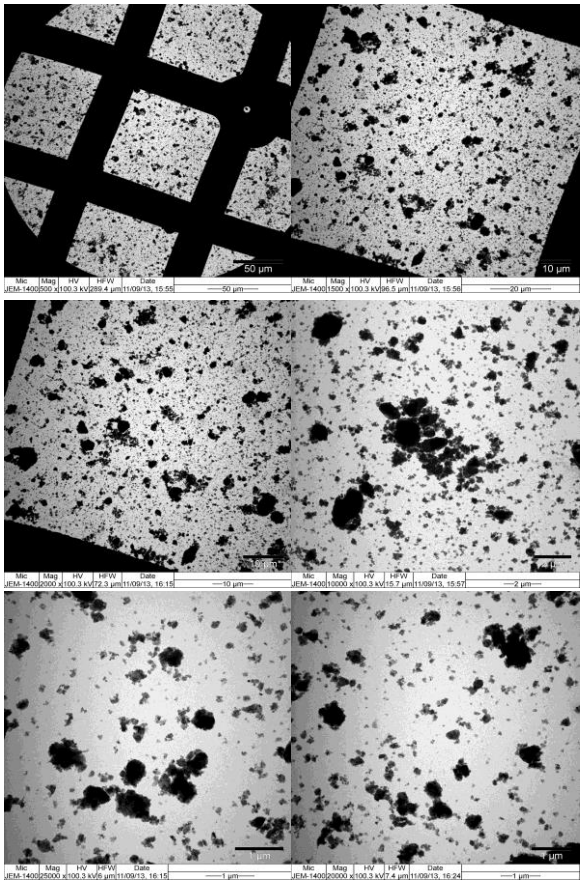

Figure 3. TEM image of powder mixture synthesized for 4 hours (before leaching).

When the microstructure images in Figure 4 are examined, it will be possible to say that the free particles are mostly contained within the structure, rather than the microstructures of B_4C particles prior to leaching operations. When the evaluation is done in terms of the powder shape and morphological aspects, we can say that the powder particles in the equiaxed geometric form are in smaller sizes and that those in polyhedron geometric forms are in larger sizes. It was determined that the agglomerate formation behaviors exhibited by powder particles prior to leaching were also minimized by the leaching process. In the study conducted by Alizadeh and colleagues, the synthesized B_4C particles showed similarity with the TEM image in the equiaxed structure of the nano-sized B_4C particles used as the starting material in composite production [15].

When the microstructure images in Figure 5 were examined, it was possible to see the twin formations exhibited by the B_4C particles after the leaching process in the powder mixture synthesized for 4 hours. In terms of evaluation of the twin formation and TEM examinations; Anselmi and colleagues investigated the effects of synthesis temperature on B_4C structural errors by using spark plasma synthesis method. In their experimental and modeling studies, they focused on the existence of twins [16]. In their other studies, Anselmi and colleagues conducted TEM-oriented simulation studies to analyze the effect of Twin formations, resulting from planar errors, on the X-ray diffraction pattern of B_4C [17].

Li et al. conducted a study on the metal-matrix composite structure of the nano-structured Al 5083/B_4C and deformation twinning in B_4C particles. With TEM studies, they supported the twin formations. They noted that the twin formations in B_4C particles were caused by high shear force and regional high intensity stress forces [18]. The TEM images of the synthesized powder mixture after leaching process also show similarities in terms of twin formation.

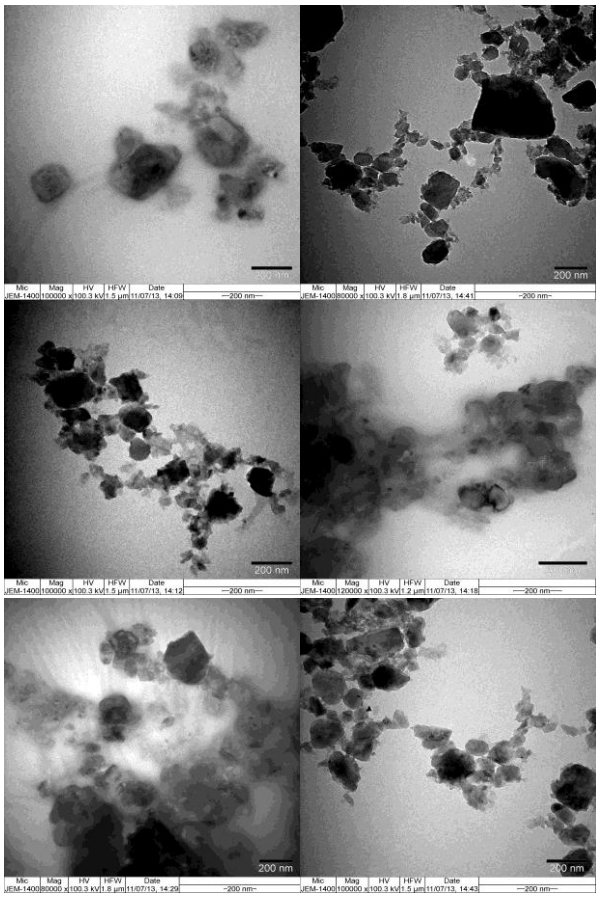

Figure 4. TEM image of the powder mixture synthesized for 4 hours (after leaching).

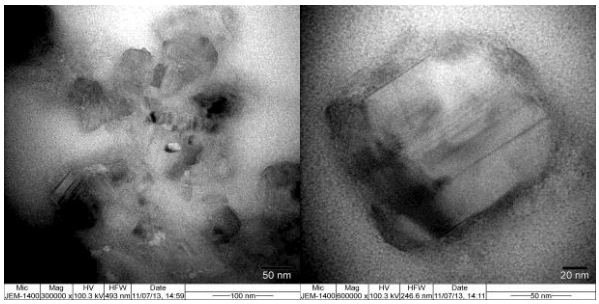

Figure 5. TEM-twin formation of powder mixture synthesized for 4 hours (after leaching).

The size analysis results conducted before and after leaching processes for the powder mixture, which was synthesized at the end of 4 hours when Mg reactant was used, are shown in Figure 6. For the powder-mixture synthesized for 4 hours, the nanoparticle size measurement result conducted before leaching process was determined as Z-average (d.nm) = 405.7 nm. For the powder-mixture synthesized for 4 hours, the sizes of the B_4C particles after the leaching process were measured as Z-average (d.nm) =185.8.

The microstructure images given in Figure 7 show that agglomeration occurred in powders prior to leaching processes. The large values in size analysis measurements are thought to be due to the influence of ceramic phases, which are usually agglomerates. In Figure 7-a, it was determined that powder particles 50 nm and below are present in the TEM image of the powder mixture synthesized for 4 hours before the leaching process. On the other side, in Figure 7-B, it is seen that free particles mostly take part by the effect of the leaching process.

Preparation of TEM sample is very important in TEM examinations. Although it was rare, the negative effects of this condition were encountered during TEM examinations. When the TEM microstructures in Figure 8-a and 8-b were examined, it was observed that the powder mixture could not be distributed well and as a result of this situation, it caused tearing on the grid in the regions where it was densely located. Therefore, TEM sample preparation stages were reviewed and the problems based on deformation that could be in the grid and samples used during the examination were eliminated.

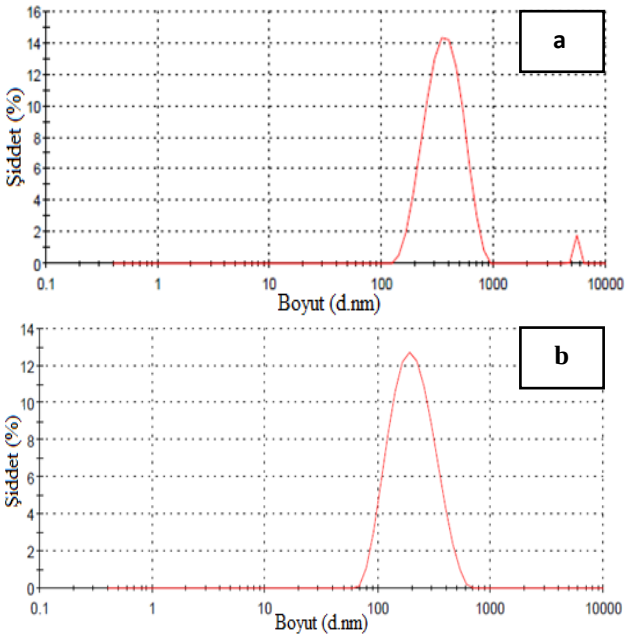

Figure 6. Nanoparticle size analysis of 4-hour synthesized powder mixture; a) Before leaching b) After leaching

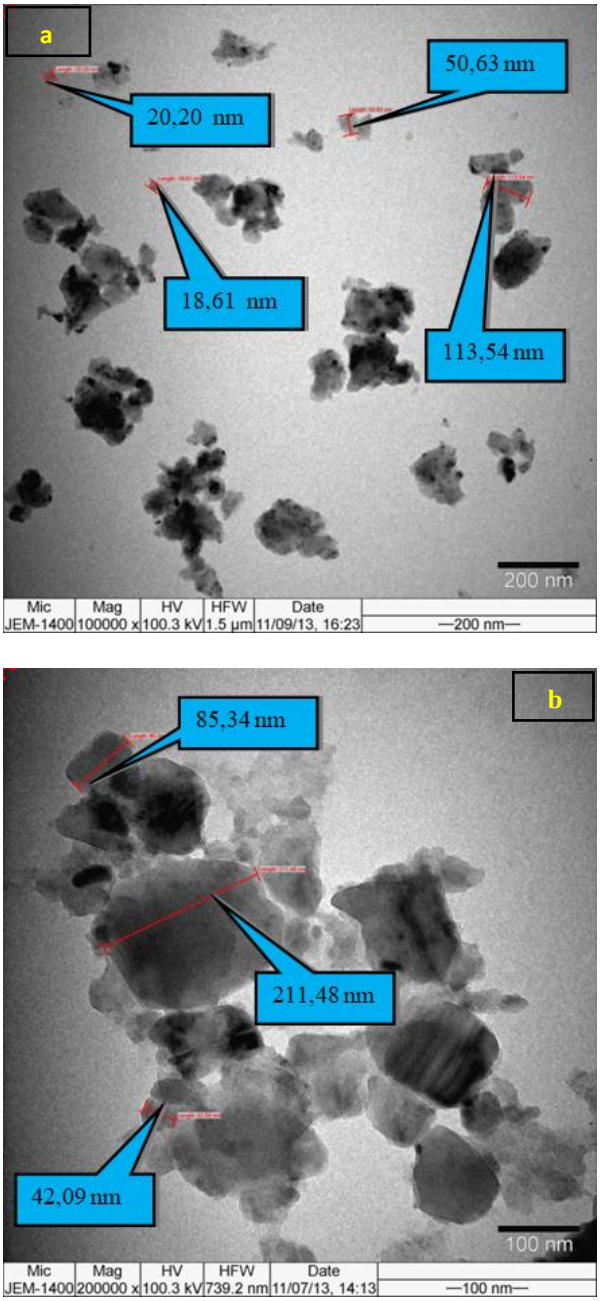

Figure 7. TEM size analysis of powder mixture synthesized for 4 hours: a) before leaching, b) after leaching

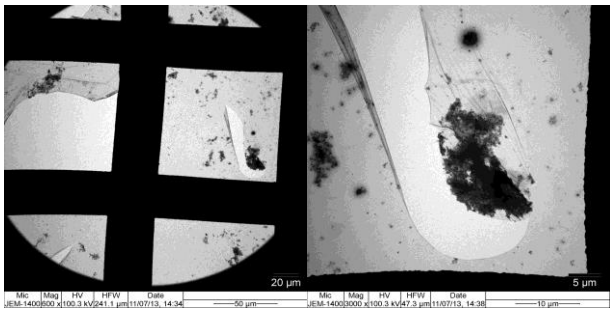

Figure 8. TEM image of the powder mixture synthesized for 4 hours (after leaching).

High-resolution TEM imaging and the examination of the selected-field diffraction pattern were performed only on the powder mixture obtained in nanoparticle size alone after 4-hour synthesis with Mg reactant after the leaching processes (Figure 9). In this context, the high-resolution imaging and selected-field diffraction pattern examination of the nano-sized B_4C particles that were available in the structure after leaching were performed. On its microstructure obtained in TEM image mode over a specific region of the powder mixture synthesized for 4 hours, various B_4C particles in equiaxed, irregular and polyhedral geometric forms are seen. Figure 9 shows the selected area diffraction pattern taken from the same region. When the selected field diffraction pattern was examined, the reflections in the form of spot and ring, which the special orientation of the powder mixture caused, were determined.

In the selected-field diffraction pattern examinations, the agglomerate behavior of the nanoparticle-sized B_4C particles and the fact that they were in coarse particle structures prevented the exact formation of the ring-electron diffraction patterns, one of the TEM indexing techniques, and caused the emerging of discrete ring patterns [14, 19]. At the same time, pattern formations of the amorphous ceramic phase structures that emerged as a result of the mechanochemical synthesis were also found to exist in the structure, mostly in the form of spots and even slightly discrete rings (Figure 9-b).

Jain et al. performed the TEM examinations in their studies conducted on electrolytic production of boron from B_4C particles which they identified as metallic scrap. They demonstrated the discrete and ring-shaped diffraction patterns of boron by examining the selected-field diffraction pattern. They stated that the material was in polycrystalline structure and there were numerous diffraction patterns, and they defined the β-rhombohedral boron structure by diffraction calculations [20]. Li et al. studied the broad twinning attitude in Al-%4Mg-B_4C nanocomposite. With the selected-field diffraction pattern examinations, they mentioned about the formation of discrete ring and spot patterns resulting from the emerging large twin structures [21].

Therefore, as opposed to calculation method via ring proportioning, in the selected-field diffraction pattern examinations, the spot-diffraction-pattern solution method was used in the indexing of B_4C particles. By using the equation given in experimental studies, indexing of B_4C particles was completed. When the selected field diffraction pattern in Figure 9-b was examined, the center spot, on which the reflection occurred, was assumed as a zero (zone) axis and the vector lengths of the reflection spots were calculated according to the center spot.

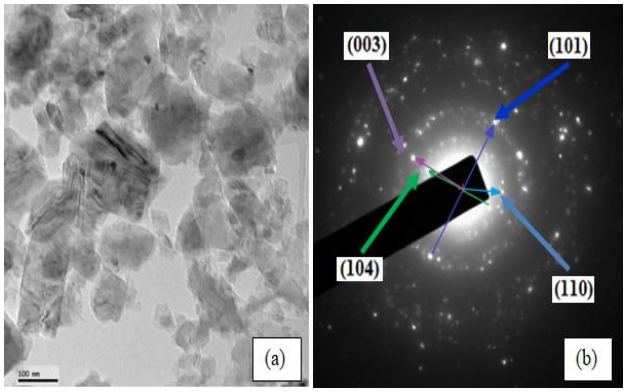

Figure 9. TEM image of powders synthesized for 4 hours (after leaching); a) Bright field image, b) selected-field diffraction pattern.

As a result of the calculations, the coordinates of the spot patterns that made reflection were shown on the images. In line with the vector lengths and camera constant calculations, d values were calculated from diffraction patterns and they were determined as 2,56 – 2,80 – 4,03 – 4,49 Â, respectively. Compared to the diffraction patterns of the B_4C particles, the calculated d values of the reflection spots were found to overlap (Figure 9-b).

4. Conclusions

In this study, related to the synthesis of nanoparticle ceramic B_4C phase after leaching and the production of B_4C particles, which is a high-tech product, at room temperature (as opposed to the chemical methods or high temperatures) by using B_2O_3-Mg-C triple initial powder components via the mechanochemical method, the following conclusions were reached.

- After leaching at the end of 4 hours of synthesis, in XRD analysis, the peaks that define the ceramic phase of nanoparticle B_4C was determined.
- When the TEM microstructure image was examined, it was observed that polyhedron, stick polyhedron and equiaxed B_4C particles were available in the structure.
- As a result of TEM examinations, the presence of twin formations exhibited by B_4C particles was determined.
- When the TEM selected-field diffraction pattern was examined, it was determined that there were many reflections in the form of spot and discrete ring caused by the special orientation of the powder mixture.
- The efficiency of the leaching process made clear the importance of single-phase nano B4C particle synthesis on the reaction activity of the Mg metal.

References

1. Sivasankaran, S., Sivaprasad, K., Narayanasamy, R., Satyanarayana, P.V., *X-ray peak broadening analysis of AA 6061$_{100-x}$–x wt.% Al_2O_3 nanocomposite prepared by mechanical alloying*, Materials Characterization, 2011. **62**: 661-672.
2. Khaghani-Dehaghani M.A., Ebrahimi-Kahrizsangi R., Setoudeh N., Nasiri-Tabrizi B., *Mechanochemical synthesis of Al_2O_3–TiB_2 nanocomposite powder from Al–TiO_2–H_3BO_3 mixture*, Int. Journal of Refractory Metals and Hard Materials, , 2011. **29**: 244–249.
3. Yokoyama, T., *Basic Properties and Measuring Methods of Nanoparticles*, Fundamentals of Nanoparticles, 2013. Chapter 1, 5-10.
4. Castro, C. L. and Mitchell, B. S. *Nanoparticles from Mechanical Attrition*, Functionalization and Surface Treatment of Nanoparticles, 2002. Chapter 1, 1-15.
5. Rahimian, M., Ehsania, N., Parvin, N., Baharvandi, H. R., *The effect of particle size, sintering temperature and sintering time on the properties of Al–Al_2O_3 composites, made by powder metallurgy*, Journal of Materials Processing Technology, 2009. **209**: 5387–5393.
6. Rahimian, M., Parvin, N., Ehsani., N., *The effect of production parameters on microstructure and wear resistance of powder metallurgy Al–Al_2O_3 composite*, Materials and Design, 2011. **32**: 1031–1038.
7. Arslan, G., Kalemtaş, A., Tunçer, E., Yeşilay, S., *Emdirme Sonrası Isıl İşlemlerin B_4C-Al Kompozitlerin Mikro Yapı ve Özelliklerine Etkileri*, Anadolu Üniversitesi Bilim ve Teknoloji Dergisi, 2009. **10**(1): 267-276.
8. Cafri, M., Dilman, H., Dariel, M. P., Frage, N., *Boron carbide/magnesium composites: Processing, microstructure and Properties*, Journal of the European Ceramic Society, 2012. **32**: 3477–3483.
9. Abdizadeh, H., Ebrahimifard, R., Baghchesara, M. A., *Investigation of microstructure and mechanical properties of nano MgO reinforced Al composites manufactured by stir casting and powder metallurgy methods: A comparative study*, Composites: Part B, 2014. **56**: 217–221.
10. Karabulut, H., Çıtak, R., Çinici, H., "*Mekanik Alaşımlama Süresinin Al + % 10 Al_2O_3 Kompozitlerde Eğme Dayanımına Etkisi*", Gazi Üniv. Müh. Mim. Fak. Der., 2013. **28**(3): 635-643.
11. Setoudeh, N., and Welham, N. J., *Formation of zirconium diboride (ZrB_2) by room temperature mechanochemical reaction between ZrO_2, B_2O_3 and Mg*, Journal of Alloys and Compounds, 2006. **420**: 225–228.
12. Suryanarayana, C., *Mechanical alloying and milling*, Progress in Materials Science, 2001, 46, 1-184.
13. Deng, F., Xie, H. Y., Wang L., *Synthesis of submicron B_4C by mechanochemical method*, Materials Letters, 2006. **60**: 1771–1773.
14. Sharifi, E. M., Karimzadeh, F., Enayati, M. H., *Mechanochemical assisted synthesis of B_4C nanoparticles*, Advanced Powder Technology, 2011. **22**: 354–358.
15. Alizadeh, A., Taheri-Nassaj, E., *Mechanical properties and wear behavior of Al–2 wt.% Cu alloy composites reinforced by B_4C nanoparticles and fabricated by mechanical milling and hot extrusion*, Materials Characterization, 2012. **67**: 119-128.
16. Anselmi-Tamburini, U., Munir, Z. A., *Influence of Synthesis Temperature on the Defect Structure of Boron Carbide: Experimental and Modeling Studies*, J. Am. Ceram. Soc**.**, 2005. **88**(6): 1382–1387.
17. Anselmi-Tamburini, U., Ohyanagi, M., and Munir, Z. A., *Modeling Studies of the Effect of Twins on the X-ray Diffraction Patterns of Boron Carbide*, Chem. Mater., 2004. **16**: 4347-4351.
18. Li, Y., Zhao, Y. H., Liu, W., Zhang, Z. H., Vogt, R. G., Lavernia, E. J., Schoenung, J. M., *Deformation twinning in boron carbide particles within nanostructured Al 5083/B_4C metal matrix composites*, Philosophical Magazine, 2010. **90**(6): 783-792.
19. Zheng, R., Hao, X., Yuan, Y., Wang, Z., Ameyama, K., Ma, C., *Effect of high volume fraction of B_4C particles on the microstructure and mechanical properties of aluminum alloy based composites*, Journal of Alloys and Compounds, 2013. **576**: 291–298.
20. Jain, A., Anthonysamy, S., Ghosh, C., Ravindran, T. R., Divakar, R., Mohandas, E., "*Electroextraction of boron from boron carbide scrap*, Materials Characterization, 2013. **84**: 134-141.
21. Li, Y., Lin, Y. J., Xiong, Y. H., Schoenunga, J. M., and Lavernia, E. J., *Extended twinning phenomena in Al–4% Mg alloys/B_4C Nanocomposite*, Scripta Materialia, 2011. **64**: 133–136.